



Diss. 2007 - 01
January

Spectroscopic investigation of the charge dynamics
of heavy ions penetrating solid and gaseous targets

S. Korostiy

(Dissertation Technische Universität Darmstadt)

Gesellschaft für Schwerionenforschung mbH
Planckstraße 1 · D-64291 Darmstadt · Germany
Postfach 11 05 52 · D-64220 Darmstadt · Germany

Spectroscopic investigation of the charge dynamics of heavy ions penetrating solid and gaseous targets

Vom Fachbereich Physik
der TECHNISCHEN UNIVERSITÄT DARMSTADT

zur Erlangung des Grades
eines DOKTORS DER NATURWISSENSCHAFTEN
(DR. RER. NAT.)

genehmigte Dissertation von
Ing.-Phys. **Svitlana Korostiy**
aus Gadyach (Ukraine)

Darmstadt 2006

D 17

Referent: Prof. Dr. Dr. h.c./RUS D.H.H. Hoffmann
Korreferent: Prof. Dr. M. Roth
Tag der Einreichung: 18.07.2006
Tag der Prüfung: 13.11.2006

Zusammenfassung

Die vorliegende Doktorarbeit präsentiert Untersuchungen zum Abbremsprozess von schnellen Schwerionen in Materie. Im Rahmen dieser Arbeit wurde der Einfluss der Targetdichte auf den Abbremsprozess untersucht. Die Experimente wurden mit $^{48}\text{Ca}^{6+}$ – $^{48}\text{Ca}^{10+}$ und $^{26}\text{Mg}^{5+}$ bei Strahlenergien von 11,4 MeV/u sowie 5,9 MeV/u in Wechselwirkung mit festen und gasförmigen Targets ausgeführt. Eine neuartige Diagnosemethode – Röntgenspektroskopie der K-Schalen Strahlung des Projektils – wurde verwendet, um den Ladungszustand des Projektils in Abhängigkeit seiner Geschwindigkeit während das Eindringens in das Medium zu bestimmen. Zum ersten Mal wurde eine orts aufgelöste Messung der Projektilstrahlung in einem Festkörper realisiert. Durch den Einsatz von porösen Materialien wie Silica aerogels konnte die Abbremslänge der Ionen um den Faktor 20–100 im Vergleich zu gewöhnlichen Quarz gestreckt werden. Der bei der K-Schalen Spektroskopie beobachtete Dopplereffekt wird genutzt, um die Ionengeschwindigkeit in Abhängigkeit zur Eindringtiefe in das Targetmaterial zu berechnen. Es wird eine vergleichende Analyse der K_{α} Spektren von Schwerionen in festen (Silica aerogel) und gasförmigen (Argon und Neon) Targets bei gleichen Energien durchgeführt. Es wird gezeigt, dass der dominierende Einfluss von Stößen in dichter Materie zu einer Erhöhung des effektiven Ionisationsquerschnittes bei hoher Geschwindigkeit sowie zu einer Unterdrückung des Elektroneneinfangs in angeregte Projektilzustände bei niedrigen Geschwindigkeiten führt. Daraus resultierend wird eine Erhöhung des Ladungszustands der Ionen in fester Materie beobachtet. Diese Effekte werden mittels eines numerischen Modells zur Besetzungskinetik des Projektils erklärt und sind in guter Übereinstimmung mit den Messungen.

Abstract

This thesis presents the study of the slowing down process of fast heavy ions inside matter. In the framework of this research, the influence of the target density on the stopping process is investigated. Experiments on the interaction of $^{48}\text{Ca}^{6+}$ - $^{48}\text{Ca}^{10+}$ and $^{26}\text{Mg}^{5+}$ ion beams with initial energies of 11.4 MeV/u and 5.9 MeV/u with solid and gaseous targets have been carried out. A novel diagnostic method, X-ray spectroscopy of K-shell projectile radiation, is used to determine the ion charge state in relation to its velocity during the penetration of fast heavy ions inside the stopping material. A spatially resolved analysis of the projectile and target radiation in solids is achieved for the first time. The application of low-density silica aerogels as stopping media provided a stretching of the ion stopping length by 20 - 100 times in comparison with solid quartz. The Doppler Effect observed on the projectile K-shell spectra is used to calculate the ion velocity in dependence on the ion penetration depth in the target material. A comparative analysis of K_α spectra of fast heavy ions is performed in solid (silica aerogels) and gaseous targets (Ar and Ne gases) at the same ion energy. It is shown that the dominant role of collisions in dense matter leads to an increase of the effective ionization cross section at high ion velocity and suppression of the electron capture to the projectile ion excited states at low ion velocity. As a result, an increase of the ion charge state in dense matter is observed. The experimentally detected effects are interpreted with numerical calculations of the projectile population kinetics, which are in good agreement with measurements.

Contents

Zusammenfassung	iii
Abstract	v
1 Introduction	1
2 Interaction of heavy ions with matter	5
2.1 Historical review	5
2.2 Stopping process in cold matter	7
2.2.1 Bohr's model	7
2.2.2 Bethe's approach	8
2.2.3 Corrections to Bethe's theory	9
2.3 Elementary processes in ion-atom collisions	11
2.3.1 Projectile ionization	12
2.3.2 Bound electron capture	13
2.3.3 Radiative decay	14
2.3.4 CAPTURE and LOSS codes	16
2.4 Projectile charge state	19
2.4.1 Average charge	20
2.4.2 Effective charge	21
2.5 Target density effect	23
2.5.1 Experimental evidence of the density effect	23
2.5.2 Theoretical explanation	24
3 Experimental setup and method	27
3.1 UNILAC facilities	27
3.2 K-shell projectile radiation as diagnostic method	29
3.3 Experimental scheme	31
3.4 Target material	32
3.4.1 Silica aerogel	32
3.4.2 Gaseous target	33

3.5	Diagnostics of the projectile radiation	35
3.5.1	Spectrometer design and method of the observation	35
3.5.2	Analysis of the ion velocity dynamics	39
3.5.3	Visible diagnostics of the gaseous target	41
4	Experiments and data analysis	43
4.1	Experimental results with solid targets	43
4.1.1	Silica aerogel as a solid target	43
4.1.2	K-shell target radiation	46
4.1.3	Velocity dynamics	48
4.1.4	Projectile charge states	51
4.1.5	Analysis of the projectile charge state dynamics	59
4.2	Experimental results with gaseous targets	61
4.2.1	Projectile radiation	62
4.2.2	Diagnostics of the gas density	65
4.3	Experimental evidence of the gas-solid effect	67
5	Numerical model of the ion population kinetics	71
6	Conclusions and outlook	77
	Acknowledgments	87
	Curriculum Vitae	89
	Erklärung	91

Chapter 1

Introduction

Over the years, the study of the interaction of fast heavy ions with matter has evolved into a large research field due to new powerful experimental methods and facilities around the world. The interaction of fast heavy ions with matter is a unique method to investigate the processes in complex atomic systems, which play a very important role in the development of modern physics [Geissel et al., 2002].

The actual research in this field of science is motivated by the application of ion beams for well tailored energy deposition in matter. A large amount of energy can be deposited to well defined areas of the target at a well defined dose rate because of the extreme stopping power of heavy ions. The investigation of physical processes, which take place during the slowing down of fast heavy ions in matter, is of a great importance. Among the various applications of energy deposition in matter by heavy ion beams, some of them should be mentioned explicitly: matter heating, inertial fusion and tumor therapy.

A big progress has been achieved in the field of heavy ion-target interactions with the advent of the new accelerator facilities. Intense heavy ion beams open new possibilities to generate high energy density states or warm dense matter [Hoffmann et al., 2002]. A new generation of experiments has been started with heavy ions of a large energy region from MeV/u to GeV/u and very high intensities. At these conditions it is possible to use heavy ions for matter heating [Tahir et al., 2006]. In warm dense matter experiments macroscopic dense volumes can be created due to high energy densities induced by heavy ion beams in solid targets. Variations of the target material properties during the interaction process (phase transitions) change the relation between the ion charge and its energy. The knowledge of the behavior of matter under extreme conditions is of significant importance for fundamental physics.

In the inertial confinement fusion [Labaune et al., 2000] the kinetic energy of the ion beam is converted into soft X-ray radiation inside a converter target (hohlraum). This radiation heats fusion pellet, located in the center of the

hohlraum, and the stopping material is transformed in a fully ionized plasma. In order to determine the energy deposition in plasma, a detailed information about the charge dependent stopping power is necessary.

The fast ignition concept offers excellent opportunities to combine intense heavy ion and laser beams. In the near future heavy ion accelerators and high power lasers at the Gesellschaft für Schwerionenforschung (GSI, Darmstadt) will allow to study high energy density physics [Hoffmann et al., 2005]. Moreover, interaction processes of ion beams with matter require detailed investigations of material properties of the irradiated targets.

A big success in the study of heavy-ion penetration through matter has been achieved in tumor treatment [Kraft, 2000]. In contrast to X-rays heavy ions have a well defined penetration depth in matter. This opens the possibility to use heavy ions for tumor treatment. Heavy ions have the favorable dose profile to eliminate deep tumors due to the sharp Bragg peak at the end of the stopping range. The high ionization at the end of the range leads to a higher biological efficiency in cells. The key instrument for biomedical investigations and applications is the detailed knowledge about the penetration of heavy ions in matter.

The topic of heavy ion-target interactions is of fundamental importance for a wide range of applications. The study of heavy-ion interactions with different kind of targets requires a reliable knowledge about the slowing down process, first of all, inside cold matter. From the pioneering discovery of Bohr [Bohr, 1913] the energy loss of charged particles is proportional to the square of the projectile charge, which is a function of the projectile velocity. This is correct for protons, but for heavy ions the charge during the slowing down in matter varies with the projectile velocity. There are still many open questions about the relation of the ion charge and projectile velocity during the stopping process in matter. In ion-atom collisions the charge of ions passing through matter is changed due to electron capture and loss processes, which occur with a high probability. Up to now no accurate quantitative theoretical descriptions concerning the formation of charge states of fast heavy ions in collisions with target atoms inside matter exist. In previous researches the energy loss and the charge state distribution of projectile ions having left the target were traditionally analyzed.

This thesis presents a significant progress in the understanding of the slowing down process of heavy ion beams in matter. A novel diagnostic method to investigate the stopping process **inside** matter, X-ray spectroscopy of K-shell projectile radiation, has been introduced. This method allows determining the ion charge state as a function of the projectile velocity during the penetration of heavy ions inside the target material. The spectroscopic method is a unique tool for a spatially and spectral resolved analysis inside solids. Using a specific target material, porous silica aerogel, it is possible to increase the stopping length and better resolve the projectile dynamics. In the framework of this thesis, the experimental

evidence of the influence of the target density, the so called density effect, on the stopping process is demonstrated.

The presented experiments have been carried out at the Gesellschaft für Schwerionenforschung (GSI) in Darmstadt at the Universal Linear Accelerator (UNILAC). The measurements were performed at the Z6 experimental area of the plasma physics group.

An overview of the experimental results and theoretical approaches of the researches on the interaction of heavy ions with matter is presented in chapter 2. The stopping-power theory has been considered from the point of view of the classical and quantum-mechanical treatments. The 'effective charge' problem was discussed with the influence of collisional processes in ion-atom interactions and target parameters such as density and atomic number. Atomic collisions of fast heavy ions with target atoms at solid density are described taking into account the target density effect.

The experimental part of the work is described in chapter 3. The diagnostic method of the stopping process and target materials are presented.

In chapter 4 the results of the performed experiments are reviewed. Chapter 5 presents a numerical model of the projectile population kinetics that allow a quantitative analysis of the ion charge evolution of the stopping process.

In conclusion, the main results of the work are resumed in chapter 6 and some suggestions for further energy loss investigations are proposed.

Chapter 2

Interaction of heavy ions with matter

The presented chapter is an overview of the research on the interaction of fast heavy ions with matter. A general survey of the most important theoretical and experimental investigations of this field of science is summarized.

A significant part of the chapter is given to the attention to atomic processes between projectile ions and target atoms during their interaction. These processes are responsible for the slowing down of heavy ions in matter. Theoretical aspects of the cold electronic stopping are treated using the Bohr-Bethe-Bloch approach. According to this formula in order to estimate the energy loss of ions it is necessary to calculate their ion charge states during the slowing down process. The experimental results and theoretical activities concerning the formation of charge states of heavy ions in collisions with target matter have been discussed. The variation of the ion charge with target density gave permit to several conclusions as the mechanism of the collisional processes. The target density effect is explained with the influence of electron loss and capture processes. The researches concerning the formation of charge states during the stopping process and the influence of the target density effect are relevant for the presented thesis.

2.1 Historical review

The penetration of charged particles through matter is one of the principal ways to investigate nature. The charge particles lose their energy during the passage through the medium in collisions with target atoms. The theory of the slowing down process is complicated because of a difficult description of the ion and target charge states during the stopping process.

The greatest scientists of the last century have worked on the subject of

charged-particle penetration in matter. In 1900 Marie Curie found that energetic particles having left radioactive materials could penetrate thin foils. Than further experiments on the interaction of α -particles with different gases gave rise to the discovery of the energy deposition maximum, the so called Bragg peak. The first theoretical treatment about scattering of electrical charged particles was published by J.Thomson in his book on electricity [Thomson, 1906]. This work did not demonstrate directly the calculations of the energy loss, but the author was interested in the problem of charged particle stopping. In 1911 Rutherford published his famous discovery about the atomic structure [Rutherford, 1911]. He started to investigate the penetration of α -rays in matter.

Niels Bohr continued the validity of Rutherford's investigations. His work in 1913 was the first sufficient theory on the energy loss of ions passing through matter [Bohr, 1913]. Bohr's classical approach for the electronic stopping power was unexcelled and served as a basis for the quantum mechanically description of the stopping problem. The discovery of the nuclear fission gave the possibility for a detailed investigation of the penetration of high speed particles through matter [Bohr et al., 1940, Bohr, 1941, Bohr, 1948]. Bohr and Lindhard understood the difficulty to describe collisions between interacting particles. They connected the energy loss of fission ions along stopping path with the capture and loss of electrons by such particles [Bohr and Lindhard, 1954]. Bohr also recognized that the study of the stopping process is limited by knowledge of the ion charge state inside matter, which is estimated by the balance between electron capture and loss processes.

In the 1920s with the discovery of quantum mechanics, Bohr's classical stopping model showed inconsistencies to describe the atomic phenomena because the energy transfer occurs in discrete quantities. Hans Bethe used Bohr's approximation and recreated the classical result in the quantum-mechanical treatment [Bethe, 1930]. His calculations are valid for relativistic energies [Bethe, 1932].

Later Felix Bloch investigated the classical and quantum-mechanical approaches and found conditions in which these theories could be used. Bloch made corrections to Bethe's model and got the formula, which is valid for Bethe's result as well as for Bohr's [Bloch, 1933].

The Bohr-Bethe-Bloch formula is an unique instrument to estimate the energy loss process of projectiles. However, this theory was modified due to further development of physics. Some features of projectile ions and target atoms such as energy region of incident particles, type of ions, target density and many other can significantly change the ion energy loss in matter. Therefore, several corrections to the basic stopping formula were applied.

In spite of the fact that the stopping process in matter has its roots already in works of Bohr, Bethe and Bloch, the growing field of applications sets new problems for physicists in our century. New powerful facilities allow to investigate the

stopping not only in cold, but as well in ionized matter [Hoffmann et al., 1990].

The presented work describes the spectroscopic approach to investigate the interaction of heavy ion beam with cold targets using associated K-shell radiation of projectile ions and target atoms.

2.2 Stopping process in cold matter

The development of the cold stopping theory belongs to the beginning of XX century. The cold stopping means the energy transfer from projectile ions to the bound target electrons of the medium. Niels Bohr divided this process into two ways: nuclear and electronic. The energy loss to positive cores of target atoms is called the nuclear stopping. The electronic slowing-down process is due to collisions between electrons in the medium and projectiles. The **stopping power** S of the projectile ions in matter is defined as the differential energy loss for that particles within the material divided by the corresponding differential path length:

$$S(E) = -\frac{dE}{dx}, \quad (2.1)$$

The minus sign indicates that the energy is lost by particles. The distance at which charged particles lose completely their energy in the medium is called the **range** of the particles. It depends on the initial energy and type of the incident particles as well as the penetrated material. The energy deposition is described by the so called **Bragg curve**. The energy loss increases with the penetration depth until the sharp maximum, which is called the **Bragg peak**, where ions are stopped.

The powerful experimental methods of the latest generation are able to investigate the slowing-down process in different types of material such as partially and fully ionized plasma. In this case the energy loss of projectiles to free target electrons takes place. The presented section is addressed to theoretical approaches concerning the cold electronic stopping process.

2.2.1 Bohr's model

The baseline for all theoretical approaches of the stopping process in matter was Bohr's work [Bohr, 1913]. He characterized ion-atom collisions by impact parameter on the basis of classical mechanics. Bohr treated the collisional process as binary process, at which the projectile ion interacts with an target electron assumed to be free at the moment. The distance from the electron to the initial travel of the projectile ion, which is far from the electron, was defined as the impact pa-

parameter b . As a result of calculations, Bohr obtained the classical formula for the energy loss:

$$-\frac{dE}{dx} = \frac{4\pi N Z^2 e^4 Z_T}{m_e v^2} \ln \frac{b_{max}}{b_{min}}, \quad (2.2)$$

where Ze is the electric charge of a projectile particle, v is the projectile velocity, N is a number of target electrons per unit volume, Z_T is the atomic number of the target atom, m_e is the electron rest mass. The logarithm expression is called **Coulomb or stopping logarithm**, which appears by integrating $-(dE/dx)$ over b from a minimum to a maximum value. In the case $b_{min} = 0$ and $b_{max} = \infty$ it leads to an infinite rate of energy loss. Therefore, the integrating limits should be apply. Bohr's theory works for projectile velocity much smaller than the speed of light, $1 < v/v_0 < Z^{2/3}$, where Z is the atomic number of the projectile ion, v_0 is the velocity of the electron in the ground state of the hydrogen atom, $v_0 = 2.188 \times 10^8$ cm/s [Bohr, 1948].

2.2.2 Bethe's approach

Bohr's stopping model was unique for many years. However, Bohr understood the limits of its application. The model didn't take into account the discrete energy of target electrons. Not any energy transfer to target atoms is possible. Some years later Bohr pointed out that the binding effects are very important during the slowing-down process. Distant collisions are treated as free-electron scattering by the projectile ion. However, interactions at small distances were considered as electromagnetic excitations of harmonic oscillators and could not be described by means of classical mechanics. Hans Bethe treated the energy loss process by means of the quantum mechanics using the first Born approximation [Bethe, 1930]. He used the momentum transfer rather than impact parameter to characterize collisions. Under this condition the energy loss process is written as

$$-\frac{dE}{dx} = \frac{4\pi N Z^2 e^4}{m_e v^2} B_{Bethe}. \quad (2.3)$$

The term B_{Bethe} is called the **stopping number** and corresponds:

$$B_{Bethe} = Z_T \ln \frac{2m_e v^2}{I}, \quad (2.4)$$

where Z_T is the nuclei charge of the target material, I is a mean excitation potential per electron and is expressed as

$$I = \frac{1}{Z_T} \sum_n f_n \hbar \omega. \quad (2.5)$$

$\sum_n f_n \hbar \omega$ is equal to a number of electrons on the n shell of target atoms with the oscillator strength of discrete transitions f_n with the energy $\hbar \omega$.

2.2.3 Corrections to Bethe's theory

The energy loss problem went on with the investigations of Felix Bloch. He considered classical Bohr's and quantum-mechanical Bethe's concepts taking into account the regions of application [Bloch, 1933]. It is expressed with the dimensionless parameter, which allows quantum perturbation theory when small, but permits a classical treatment when large compared to unity:

$$\eta = \frac{Ze^2}{\hbar v}. \quad (2.6)$$

Bloch considered distant collisions according to the Bohr binary model, at which the target electrons could be treated as if they would be free. In this case Bohr's formula is valid at the limits $\eta \gg 1$. Bethe's approach is able at $\eta \ll 1$, at which close collisions were analyzed quantum mechanically because of the important role of the binding effects. This in fact is the result that Bloch obtained and introduced the nonrelativistic correction term

$$B_{Bloch} = \psi(1) - \operatorname{Re} \psi\left(1 + i \frac{Ze^2}{\hbar v}\right), \quad (2.7)$$

where ψ is the logarithmic derivative of gamma function Γ .

As a result, the expression for the energy loss is written as

$$-\frac{dE}{dx} = \frac{4\pi N Z^2 e^4}{m_e v^2} (B_{Bethe} + B_{Bloch}). \quad (2.8)$$

The Bohr-Bethe-Bloch concept is still the starting point to calculate the energy loss of heavy ions passing through matter. There are many effects that have significant influence on the energy loss of projectile ions, and some corrections to the basic stopping formula should be taken into account.

Bethe's formula was derived using the Born approximation. It is valid if the velocity of the incident particles is much larger than the velocity of the projectile orbital electrons. In other case the stopping formula should be modified by calculating the contribution of the binding effects, the so called **shell correction**. It is expressed as

$$B_{shell} = -\frac{C_i}{Z_T}, \quad (2.9)$$

where C_i is the function of various parameters for atomic shell i , Z_T is the atomic number of the target atom. Shell correction is especially important for the inner electrons of heavier elements and low energy region.

Another important correction was the 'Barkas effect' in the 50's after the discovery of the fact that the stopping of π^+ particles is significantly different than for π^- particles because of different screening [Barkas et al., 1956, Barkas et al., 1963]. This correction plays important role at low ion velocities and can be neglected at high energy region.

The ability of the electrical field of the incident particles to polarize atoms is responsible for the so called 'polarization effect'. The basic Bohr-Bethe-Bloch formalism described gases at low density. In this case particles can be assumed as independent. That can not be valid for solids and liquids. Enrico Fermi emphasized that the dependence of energy loss in addition to Bethe-Bloch parameters supplements with material dielectronic properties [Fermi, 1939].

The study of energy loss of partially stripped ions has been in progress with the development of new generation of high energy accelerators. Analytical formulas for the electronic stopping power of swift lithiumlike and berylliumlike ions have been presented on the basis of first-order perturbation theory by T.Kaneko [Kaneko, 1994]. He assumed that the charge state of the projectile remains frozen during its passage and all correction terms were neglected.

Heavy ions become available over a large range of kinetic energies and there are a lot of applications in modern physics. As a result, relativistic theory of stopping for heavy ions was developed. Ahlen reviewed the theory of the electromagnetic interactions between charge particles moving with relativistic velocities and matter [Ahlen, 1980]. Lindhard and Sørensen have studied the stopping power for light and heavy ions, whose velocity is comparable to the speed of light [Lindhard and Sørensen, 1996].

The stopping of nonrelativistic heavy ions has been analyzed as function of the projectile charge by P.Sigmund [Sigmund, 1997]. The excitation and ionization of target electrons were described according to Bohr's classical theory. The influence of the projectile electrons was taking into account mainly via screening of the Coulomb interaction.

Some years later, G.Schiwietz proposed a simple method to calculate the impact-parameter dependence of the electronic energy loss of bare ions for all impact parameters [Schiwietz and Grande, 1999]. He computed the energy loss of heavy ions using the impact-parameter scaling and Bloch's stopping power treatment. G.Maynard has described the energy loss of partially ionized heavy ions in the energy range of MeV/u using the convergent kinetic Lindhard theory [Maynard et al., 2001].

Nowadays, different new theoretical approaches for the stopping of fast heavy ions in matter are in progress. However, there are still many open questions,

for example, a lacking knowledge about the charge of ions, which varies with the projectile velocity during the slowing down in matter. In order to estimate this charge-changing phenomena the role of elementary processes in ion-atom collisions should be ascertained.

2.3 Elementary processes in ion-atom collisions

During the interaction of fast heavy ions with matter the exchange electronic configuration of the target atoms and projectile ions takes place. Atomic processes concerning the projectile ions are describes in this section.

A comprehensive description of the theoretical aspects concerning the interaction of fast heavy ions with matter is complicated because of plenty of projectile charge states formed during the stopping process. The formation of ion charge states is a result of atomic processes, which occur with a high probability in ion-atom collisions. They are divided into collisional

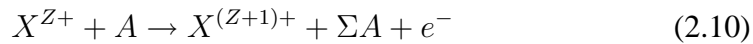
- **projectile ionization**
- **bound electron capture**
- **collisional excitation and deexcitation**

and non-collisional processes

- **radiative decay**
- **Auger decay**

A probability of a certain collisional process is characterized by a **cross section** σ , which is defined as a ratio of a number of given events per unit time per a target particle to a flux of the incident particles per square unit. In atomic scale one unit of a cross section is $\pi a_0 \simeq 0.88 \times 10^{-16} \text{ cm}^2$, where a_0 is the Bohr radius.

The ion interacting with a target atom can increase the charge as a result of loss of a proper electron:



or decrease the charge as a result of capture of a target electron:



where X^{Z+} is the projectile ion, Z is the ion atomic number, A is the target atom, ΣA are possible states of the target after the collision. These processes lead to the charge change of heavy ions during the slowing down in matter.

The total charge changing-cross section is defined by sum of ionization and electron capture cross sections:

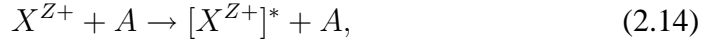
$$\sigma_{tot} = \sigma_{ion} + \sigma_{ec}, \quad (2.12)$$

where the dependence of these cross sections on the atomic parameters of projectile ions and target atoms is treated as [Shevelko, 1999]

$$\sigma_{ion} \sim \frac{Z_T^2}{Z_P^2 v^2}, \quad \sigma_{ec} \sim \frac{Z_T^5 Z_P^5}{v^{11}}, \quad (2.13)$$

where Z_P and Z_T are, respectively, the projectile and target atomic numbers, v is the velocity of the incident ions. These expressions are valid at high energies, $v/Z_P > 2.188 \times 10^8$ cm/c. The decrease of the electron capture cross section with the energy increase is significantly faster in comparison with the ionization cross section. However, the capture process has stronger dependence on the projectile and target charges. Therefore, the contribution of each process depends on the energy range, the atomic number of projectile ions and target.

In addition to the charge changing processes the excitation of projectile ions takes place in ion-atom collisions. This process induced by ion impact with a target atom and, as a consequence of the interaction, the transition of an bound electron from the ground to the excited state of the ion occurs:



where the asterisk denotes the excited state. The return to the ground state is accompanied by collisional deexcitation or radiative decay.

In the following subsections a general survey of collisional processes as well as radiative decay is considered. The Auger decay is explained in the next chapter in the course of the diagnostic method.

2.3.1 Projectile ionization

The earliest extensive theory about the ionization process of fast heavy ions in collisions with target atoms was presented by N.Bohr [Bohr, 1948]. He pointed out that the projectile ion losses its electrons which have orbital velocities smaller or equal than the velocity of the ion. Bohr and Lindhard [Bohr and Lindhard, 1954] defined the ionization process as the energy transfer to electrons of the ion sufficiently light for electron escape and estimated as

$$\sigma_{ion} = \pi a_0^2 q^2 Z^{1/3} \left(\frac{v_0}{v^*} \right)^3, \quad (2.15)$$

where a_0 and v_0 are the radius and velocity of the electron in the ground state of the hydrogen atom, Z is the atomic number of the projectile ion, q is the ion charge state, v^* is the orbital velocity of the most loosely bound electron in the ground state of the ion.

The application of Bohr's theory was limited by heavy-ion velocities, which are in the range of $v_0 < v < Zv_0$. As later experiments have shown, Bohr's work and some theoretical approaches on its basis need modifications [Betz, 1972].

M.Gryzinski described the collisional ionization cross section using a detailed classical theory of two-particle collisions in the laboratory system of coordinates [Gryzinski, 1965a, Gryzinski, 1965b, Gryzinski, 1965c]. He assumed that the initial direction of the second particle (target atom) coincides with the z axis of the laboratory system. As a result of the interaction with the first particle (projectile ion), the velocity of the second particle changes in magnitude and direction. The total ionization cross section was treated as

$$\sigma_{ion} = \sum_n N_n \pi \left(\frac{Z_T e^2}{U_n} \right)^2 G(V), \quad (2.16)$$

where N_n and U_n are, respectively, the population number and binding energy of electrons in the n -th shell of the projectile, Z_T is the target atomic number, e is the electronic charge. The summation is performed over all projectile shells. In this equation $G(V)$ is a function of the scaled velocity V equal to v/v_n , where v is the projectile velocity, v_n is the velocity of orbital electrons of projectile. The function is given by J.McGuire as [McGuire and Richard, 1973]

$$G(V) = a^{3/2} \frac{1}{V^2} \left\{ a + \frac{2}{3} \left(1 + \frac{1}{b} \right) \ln(2.7 + V) \right\} \left(1 - \frac{1}{b} \right) \left(1 - \left(\frac{1}{b} \right)^{1+V^2} \right), \quad (2.17)$$

where

$$a = \frac{V^2}{1 + V^2}, \quad b = 4V^2 \left(1 + \frac{1}{V} \right). \quad (2.18)$$

This function is maximal for $v = v_n$ and close to the disappearance if the deviation between velocities is large.

2.3.2 Bound electron capture

The first and the most simple method to calculate the bound electron capture cross section in ion-atom collisions is well-known Oppenheimer-Brinkman-Kramers approximation written for hydrogenlike states [Oppenheimer, 1928, Brinkman and Kramers, 1930]:

$$\sigma_{ec}(n_i \rightarrow n_f) = \frac{8.53 \times 10^{-16} Z^2 E_i^{5/2} E_f^{3/2} E_K^4}{[E_K^2 + 2E_K(E_i + E_f) + (E_i - E_f)^2]^5}, \quad (2.19)$$

where Z and E_K are, respectively, the atomic number and kinetic energy of the projectile ion, E_i and E_f denote the electron binding energy in initial and final states characterized by quantum numbers n_i and n_f , correspondingly. This equation is based on the first Bohr approximation, which ignores target-ion interaction after the capture process has taken place. Therefore, too large values of capture cross section are observed and a reduction factor should be applied. This problem was taken into account by Chan and Eichler, who estimated the range of the reduction factor from 0.1 to 0.4 [Eichter and Chan, 1979, Eichter et al., 1981].

The bound electron capture in collisions between multielectron particles was attempted to describe by Bohr and Lindhard [Bohr and Lindhard, 1954]. The electron capture cross section was treated as

$$\sigma_{ec} = \pi a_0^2 Z_T^{1/3} q^2 \left(\frac{v_0}{v} \right)^3, \quad (2.20)$$

where a_0 and v_0 are the radius and velocity of the electron in the ground state of the hydrogen atom, Z_T is the atomic number of the target atom, q is the charge state of the projectile ion, v is the projectile velocity.

An universal empirical scaling rule for the single-electron capture cross section by fast highly charged projectiles in gaseous targets has been found by A.Schlachter et. al [Schlachter et al., 1983]:

$$\sigma_{ec} = 1.1 \times 10^{-8} \frac{q^{3.9} Z_T^{4.2}}{E^{4.8}}, \quad (2.21)$$

where q is the projectile charge state, E is the energy of projectile ions and Z_T is the atomic number of the target. The experimental cross sections for a large variety of projectiles and targets were fitted using reduced coordinates:

$$\tilde{\sigma} = \sigma \frac{Z_T^a}{q^b}, \quad \tilde{E} = \frac{E}{Z_T^c q^d}. \quad (2.22)$$

A nonlinear least squares fitting routine was used to adjust a, b, c, d parameters. Schlachter's formula is valid for the projectile energy range from 0.3 to 8.5 MeV/u and arbitrary projectile-target combinations.

2.3.3 Radiative decay

The population of the excited levels is governed by competition of collisional and non-collisional processes. A radiative transition is a spontaneous emission of photon, which does not depend on the collisional characteristics. The probability of a radiative decay corresponds to the maximal value of photons per second, which an ion can radiate. Since the probability of a transition is given per unit of time it has a dimension of s^{-1} .

In quantum electrodynamics the probability dA per unit of time of a one transition from an initial excited state $|a\rangle$ to a final state $|b\rangle$ is given by [Ahiezer and Berestetski, 1981]:

$$dA = \frac{e^2\omega}{2\pi\hbar c} |\langle b | \vec{\alpha} \vec{\epsilon}^* e^{-i\mathbf{k}\mathbf{r}} | a \rangle|^2 d\Omega, \quad (2.23)$$

where c is the speed of light, $\omega = (E_a - E_b)/\hbar$ is the frequency of the emitted photon, $\vec{\epsilon}$ is its polarization vector, $\vec{\alpha}$ is the Dirac matrix, \mathbf{k} is the photon momentum and $d\Omega$ denotes space angle for the radiation.

The probability of the radiative decay defines very important atomic characteristics such as intensity of spectral lines and lifetime of the excited states. The intensity I_{10} of the spectral line for the transition 1-0 from the upper 1 to the lower 0 state is given by

$$I_{10} = N_1 A_{10} \hbar \omega, \quad (2.24)$$

where A_{10} is the radiative probability for the transition 1-0, N_1 is the number of ions in the upper level 1 per unit volume, ω is the transition frequency, $\omega = (E_1 - E_0)/\hbar$, \hbar is the Planck constant divided by 2π .

The radiative lifetime τ_κ of an excited state κ is defined as

$$\tau_\kappa = \left(\sum_{i < \kappa} A_{i\kappa} \right)^{-1} [s], \quad (2.25)$$

where $A_{i\kappa}$ is a radiative transition probability from the upper level κ to all lower levels i .

The radiative process drastically depends on the ion charge Z_P and the principle quantum number n of the projectile:

$$A \sim \frac{Z_P^4}{n^5}. \quad (2.26)$$

In order to calculate the radiative decay rates in hydrogen-like systems the classical Kramers formulas are used [Vainshtein et al., 1973]. The radiative transition probability for any atoms and ions is estimated in the form [Lebedev and Beigman, 1998]:

$$A(n_1 - n_0) = 1.61 \times 10^{10} \frac{z^4}{n_1^3 n_0} \frac{1}{\Delta n (n_1 + n_0)} \left(1 - \frac{0.236}{\Delta n} \right), \quad (2.27)$$

where z is the spectroscopic symbol of the ion, n_1 and n_0 are, respectively, the principle quantum numbers of the upper 1 and lower 0 levels, $\Delta n = n_1 - n_0$.

2.3.4 CAPTURE and LOSS codes

In the last years the study of the interaction of fast heavy ions with matter plays a critical role in such applications as the production of long-lived ion beams in accelerators [Melchert, 1999], the generation of high-density-energy matter [Hoffmann et al., 2005], heavy-ion inertial fusion [Labaune et al., 2000] and heavy-ion therapy [Kraft, 2000]. The ion charge states and charge changing-cross sections of heavy ions are important source of information about atomic collisions in complex atomic systems. The theoretical predictions of projectile ionization and electron capture cross sections in the energy range of the 1-100 MeV/u have been performed by V.Shevelko using the LOSS and CAPTURE computer code accounting to the atomic structure of the target [Shevelko, 2001, Shevelko et al., 2001]. These numerical programs were used to estimate the charge changing-cross sections for the experimental conditions of the presented work.

In the **CAPTURE** code effective cross sections of one-electron charge exchange is calculated using the method of multichannel normalization in the impact parameter representation. This method uses the relationship between the quasi-classical $a(\rho, v)$ and the quantum-mechanical $f(\mathbf{q}, v)$ charge exchange amplitudes [Shevelko, 1980].

The charge exchange between state 0 of the atomic target and state 1 of the resulting ion is written as

$$X^Z + A(n_0) \rightarrow X^{(Z-1)+}(n_1) + A^+, \quad (2.28)$$

where X^Z and $A(n_0)$ are, respectively, the projectile ion charge and the target atom before the interaction process, $X^{(Z-1)+}(n_1)$ and A^+ the projectile ion charge and the target atom after the interaction process, n is the principal quantum number.

In the impact parameter representation, the exchange cross section is estimated as

$$\sigma(v) = 2\pi \int_0^\infty W(\rho, v) \rho d\rho, \quad (2.29)$$

where $W(\rho, v) = |a(\rho, v)|^2$ is the exchange probability, ρ is the impact parameter, v is the relative velocity of colliding particles.

The impact parameter capture amplitude $a(\rho, v)$ is related to the wave $f(\mathbf{q}, v)$ treatments for electron capture and considered in Brinkman-Kramers (BK) approximation:

$$a(\rho, v) = \frac{1}{v(2\pi)^2} \int_P f(\mathbf{q}, v) e^{ik\rho} d^2\mathbf{q}. \quad (2.30)$$

The integration over vector \mathbf{q} in the equation is made on the plane P , described by equation $\mathbf{q}\mathbf{v} - w - v^2/2 = 0$.

The BK approximation is the most simple and universal method to calculate the capture cross sections in the region of the relative velocities $v \gg \sqrt{w}$, where w is the resonance defect of the reaction in atomic units, i.e. the difference between the binding energies of a captured electron in the initial (0) and final (1) states. In the BK approximation the $f(\mathbf{q}, v)$ value is a multiplication of Fourier components of the atomic wavefunctions of the initial and final states with interaction potential [May, 1964, Shevelko, 1978].

At low relative energy, $v \leq \sqrt{w}$, the probability of the capture may exceed unity which has no physical meaning. The reason is that the relationship (2.30) has been obtained in the first order of the perturbation theory [Shevelko and Vainshtein, 1993]. The more accurate computing procedures, such as the method of strong coupling between atomic states or the method of charge exchange probability normalization in the impact parameter representation is applied to remove this defect.

The method of multichannel normalization of the exchange probability for the 0-1 transition is written as

$$W_{01}^N(\rho, v) = \frac{W_{01}(\rho, v)}{1 + \sum_j W_{0j}(\rho, v)}, \quad (2.31)$$

where the summation in the denominator is over all possible final exchange channels j for the resulting ion $X^{(Z-1)+}$, including the exchange into the state 1 under study.

The physical meaning of formula (2.31) is following: if the probability W_{01} is small, the normalized probability is also small, $W_{01}^N \approx W_{01}$. Even if the probability W_{01} is large ($W_{01} \gg 1$), the normalized value remains small, $W_{01}^N \leq 1$.

The total cross sections of charge exchange for multielectron systems are difficult to calculate. It can be accomplished with the multichannel normalization method and using hydrogen-like wave functions for captured electrons. The use of hydrogen-like functions simplifies the calculation of the exchange total cross sections, i.e. those averaged over the quantum numbers m and l . The second reason is that the electron capture in the highly excited (H-like) states of a resulting ion makes a great contribution to the total cross section of the charge exchange. At high collision energy, exchange cross sections have larger dependence on the capture of inner shell electrons of the target, which are located near the unscreened nucleus and are also hydrogen-like.

The advantage of the presented method is that the total cross sections of the charge exchange between heavy multielectron atoms and ions can be calculated with regard for the capture of inner shell electrons of the target and the capture into excited states.

The **LOSS** code calculates one-electron ionization cross sections and ion-beam lifetimes for heavy low-charged ions colliding with neutral atoms in the momentum transfer representation with account of the atomic structure of the target. The calculations are performed in the Born approximation when the relative velocity v of colliding particles is quite high: $v > 1a.u. \simeq 2.2 \times 10^8$ cm/s.

The Born projectile-ionization cross section with account of the target atomic structure has the form:

$$\sigma(v) = \frac{8\pi}{v^2} \sum_P \sum_\lambda \int_0^\infty d\epsilon \times \int_{q_{min}}^\infty \frac{dq}{q^3} |F_P(q, \epsilon, \lambda)|^2 |Z_T(q)|^2, \quad (2.32)$$

$$|Z_T(q)|^2 = [Z - \sum_{j=1}^N F_{jj}(q)]^2 + [N - \sum_{j=1}^N |F_{jj}(q)|^2], \quad (2.33)$$

$$F_{jj} = \langle j | \exp(i\mathbf{q}\mathbf{r}) | j \rangle, \quad q_{min} = (I_P + \epsilon)/v, \quad (2.34)$$

where q is the momentum transfer, ϵ and λ are the energy and orbital momentum of the ejected electron. Indices P and T indicate the projectile and the target states, respectively. The function $F_P(q, \epsilon, \lambda)$ is the projectile form factor for a bound-free transitions, $Z_T(q)$ is the effective charge of the target which depends on the momentum transfer q , Z and N are the nuclear charge and the total number of electrons in the target, I_P is the binding energy of the ejected electron.

The relation (2.33) consists of two terms. The first term (screening) includes the electron-electron interactions in the elastic channel when the target electrons screen the nuclear charge of the target. The second term (antiscreeing) describes the mechanism when the target electrons act as an electron cloud in which every electron can ionize the projectile by changing its own state.

The sum $\sum_j \langle j | \exp(i\mathbf{q}\mathbf{r}) | j \rangle$ is the atomic form factor expressed in terms of the Fourier transform of the electron density $\rho(r)$:

$$\sum_j \langle j | \exp(i\mathbf{q}\mathbf{r}) | j \rangle = \int_0^\infty \rho(r) \frac{\sin(qr)}{qr} dr, \quad (2.35)$$

$$\rho(r) = \sum_\gamma N_\gamma P_\gamma^2(r), \quad (2.36)$$

$$\int_0^\infty P_\gamma^2(r) dr = 1, \quad (2.37)$$

where $P_\gamma(r)$ are the radial wave functions of the target electrons; the sum over γ runs over all electron shells of the target with N_γ being the number of equivalent electrons in the shell γ . The expressions for Fourier transforms of an arbitrary atom are suggested to obtain in a close analytical form using the Slater nodeless wave functions [Slater, 1960].

In order to calculate the radial wave functions $P(r)$ of projectile electrons the Schrödinger equation with the central-symmetrical potential $U_c(r)$ of the atomic core and a given energy ε is solved:

$$\left(\frac{d^2}{dr^2} - \frac{l(l+1)}{r^2} - \frac{2}{\omega}U_c(r/\omega) + \varepsilon\right) = \hat{V}_{ex}P(r/\omega), \quad (2.38)$$

where ε is Ry units ($1 \text{ Ry} \simeq 13.6 \text{ eV}$), ω is the eigen-value of the present equation. The right-hand side of the equation corresponds to the exchange interaction operator \hat{V}_{ex} [Shevelko and Vainshtein, 1993]. The effective field of the core electrons $U_c(r)$ is calculated with the same Slater functions, as the effective charge of the target $Z_T(q)$.

The computer code LOSS allows also to calculate the excitation cross sections of the projectiles, including excitation with autoionization, with account for the effective charge of the target $Z_T(q)$.

Collisional processes such as projectile ionization and bound electron capture, which occur with a high probability in ion-atom interactions are key parameters to investigate the stopping process of energetic ions in matter.

2.4 Projectile charge state

As follows from the Bohr-Bethe-Bloch stopping formula, in order to calculate the energy loss of heavy ions passing through matter it is necessary to estimate the ion charge as function of the ion velocity. The stopping theory was valid for the slowing down process of light particles such as protons and α -particles. Since the discovery of nuclear fission the stopping of energetic heavy particles was the subject of active investigations. During the penetration of fast heavy ions through matter several atomic processes as electron loss and capture, excitation, collisional and radiative decay take place. It leads to fluctuations of the ion charge. An important quantity is the **average charge** Z_{av} , which is defined by

$$Z_{av} = \sum_q qF(q), \quad (2.39)$$

where $F(q)$ denotes the fraction of the ions, which carries the charge q . Traditionally the average charge is measured for ions emerging from the stopping material. An excellent review of experimental results and theoretical approaches

concerning the formation of the average charge state of heavy ions passing solids and gases up to 1972 was given by Betz [Betz, 1972].

However, it was not clear which ion charge should be applied in the energy loss formula: the initial ion charge Z_P , the average ion charge Z_{av} or some **effective charge** Z_{eff} as a good approximation to the initial, formed under the influence of the target and ion beam properties. The charge at all considered velocities during the stopping process is the conception of the effective charge. This is called the 'effective charge' problem: the traditional energy loss formula can be used when a degree of ionization for projectiles in medium could be estimated.

2.4.1 Average charge

The pioneering theoretical estimation of the average charge belong to Bohr [Bohr et al., 1940, Bohr, 1941]. His idea was that fast heavy ions passing through matter lose electrons, which have an orbital velocity smaller than the projectile velocity. Bohr criterion was based on the statistical Thomas-Fermi model. Irrespective of Bohr, Lamb determined the average charge from the ionization potential of projectiles [Lamb, 1940]. He assumed that heavy fragments are stripped until the ionization potential of the next stage of ionization is greater than the kinetic energy of target electrons. This approach worked well for some heavy ions.

The first semiempirical estimation for the average equilibrium charge taking into account Bohr criterion was given by Dmitriev and Nikolaev [Dmitriev and Nikolaev, 1964]:

$$Z_{av} = Z_P \frac{\lg(v/AZ_P^\delta)}{\lg(BZ_P^\mu)}, \quad (2.40)$$

where Z_P and v are, respectively, the atomic number and velocity of the projectile ions. A , B , δ , μ are parameters evaluated from experiments with ions $Z \leq 10$ and different for solid and gaseous targets. The formula is applicable for $0.3Z_P \leq Z_{av} \leq 0.9Z_P$. In the case of $Z_{av}/Z_P \leq 0.3$ they gave another definition:

$$Z_{av} = CvZ_P^{1/2}, \quad (2.41)$$

where the parameter C is calculated from experiments with nitrogen and argon targets.

By summing of experimental data on the passing of sulphur, arsenic, iodine and uranium ions through different foil and gaseous strippers at energy range of 5-80 MeV Betz calculated the average charge formula as [Betz et al., 1966]

$$Z_{av} = Z_P(1 - K(0.71Z_P^a)^{\beta/\alpha}), \quad (2.42)$$

where the parameters K and a are evaluated from experiments, α is fine structure constant, $\alpha = 1/137$, $\beta = v/c$.

Some years later due to the development of powerful accelerators, there was the possibility to carry out experiments with heavy ions at energies above 100 MeV. Nikolaev and Dmitriev made use of experimental results and developed an universal expression for all types of ions in solid stripper [Nikolaev and Dmitriev, 1968]:

$$Z_{av} = Z_P(1 + v_r^{(-1/k)})^{(-k)}, \quad (2.43)$$

$$v_r = \frac{v}{3.6 \cdot 10^8 Z_P^{0.45}}, \quad k = 0.6. \quad (2.44)$$

The presented formula was in close agreement with experimental results.

Modifications of formulas described above were performed by Shima in 1982 [Shima et al., 1982]. He received empirical expression for the average equilibrium charge-state of heavy ions behind various foils:

$$Z_{av} = Z_P[1 - \exp(-1.25v_r + 0.32v_r^2 - 0.11v_r^3)][1 - 0.0019m\sqrt{v_r} + 0.00001m^2v_r], \quad (2.45)$$

$$m = Z_T - 6, \quad (2.46)$$

where Z_T is the atomic number of the target atoms. The presented formula is applicable in the energy range of $E < 6$ MeV/u, for projectiles and targets with atomic numbers $Z_P \geq 8$ and $4 \leq Z_T \leq 79$, correspondingly. For the first time the empirical expression was calculated for carbon foils because of plenty of the experimental information, but later corrected for all types of foils.

Attempts to calculate the average charge of projectile ions were created on the basis of experimental results and, therefore, formulas have a scope of applications.

2.4.2 Effective charge

In the forties Bohr pointed out that the energy loss of fission ions along their path in matter is estimated by the ion charge, which fluctuates due to electron loss and capture processes in the medium. He estimated the ion charge, which varies along the stopping path in matter as [Bohr et al., 1940, Bohr, 1948]

$$Z^* = Z_P^{1/2} \frac{v}{v_0}, \quad (2.47)$$

v is the projectile velocity, v_0 is the velocity of the electron in the ground state of the hydrogen atom.

The effective charge as an empirical parameter first appeared in the paper of Martin and Northcliffe [Martin and Northcliffe, 1962]. They measured the energy loss of several heavy ions in various gases as function of gas thickness and calculated the effective charge of the ions from the ratio of experimental stopping powers for measured ions and for the reference ion (helium) at the same velocity in the same gas. It was pointed out that the effective charge has a strong dependence on the velocity and charge of ions, the atomic number and density of the medium. Northcliffe recommended to discuss about stopping power in relative terms [Northcliffe, 1963, Northcliffe and Schilling, 1970]. In this case the calculation of the relative stopping powers for different ions requires that ions should move with the same velocity in the same medium such as proton. He proposed to introduce the effective charge parameter

$$\gamma^2 = \frac{S(Z_P, Z_T, v)}{Z_P^2 S(1, Z_T, v)}, \quad (2.48)$$

where $S(Z_P, Z_T, v)$ is the stopping cross section for projectile ions with Z_P passing through the medium with Z_T at velocity v , $S(1, Z_T, v)$ is the stopping cross section of proton in the same matter with the same velocity. The physical interpretation of Z_{eff} was not clear defined. Northcliffe supposed that Z_{eff} is equal to the root-mean-square (rms) charge, i.e. the statistical measure of Z_P of a varying quantity.

Pierce and Blann estimated the effective charge parameter of heavy ions for solids and gases empirically [Pierce and Blann, 1968]:

$$\gamma = 1 - \exp(-0.95v_r), \quad (2.49)$$

$$v_r = \frac{v}{v_0 Z_P^{2/3}}, \quad (2.50)$$

where v_r is reduced velocity parameter, $v_0 Z_P^{2/3}$ is Thomas-Fermi electron velocity. They did not find the difference in effective charge for these media, but there is a significant difference in rms charges. It was calculated using average charges of solid and gaseous media. Measurements showed higher value passing solids than gases. As a result, the effective charge in gases is in good agreement with rms charge. However, in solids there is no the same relationship, the rms charge may give values in some times higher, than the effective charge.

The experimental work of Anthony and Lanford showed that a general expression for the heavy ion effective charge for different target materials is possible [Anthony and Lanford, 1982]:

$$Z_{eff} = Z_P \left[1 - A_1(Z_T) \exp \left(\frac{-A_2(Z_T)v}{Z_P^{2/3} v_0} \right) \right], \quad (2.51)$$

where $A_1(Z_T)$ and $A_2(Z_T)$ are empirical functions of the target atomic numbers. It appears from this the strong dependence of the effective charge on the target material.

P. Sigmund asserted that the effective charge can not be referent to hydrogen or helium and, therefore, the relative stopping power does not have a theoretical basis [Sigmund and Schinner, 2001].

2.5 Target density effect

As evident from the presented study of the stopping process, the variation of the projectile charge is estimated by the probability of electron capture and loss processes. In ion-atom collisions more than one collision occurs and collisions with excited states are possible as well. Therefore, the final ion charge depends on collisional frequency, which is directly dependent on the density of the target medium. This is the so called density effect .

2.5.1 Experimental evidence of the density effect

The first theoretical approaches concerning the energy loss and the charge state distribution of heavy ions passing through matter were valid only for diluted gases because of easier description of collisional processes in gases. It was argued by Lamb in his calculations of the average ion charge of uranium fission fragments [Lamb, 1940]. The first quantitative data about evidence of the density effect were received by Lassen. His experimental work with uranium fission fragments clearly showed that the average charge of projectiles emerging from thin metal foils is higher than the average charge of ions emerging from gases [Lassen, 1951a]. He also found that the charge of ions emerging from the gas is function of the gas pressure [Lassen, 1951b]. If the pressure is higher, collisions become more frequent and the ionization is dominant. Some years later Lassen's discovery was explained by Bohr and Lindhard (BL model) [Bohr and Lindhard, 1954]. They related the gas-solid difference to the influence of excited states in solid target. Collisions of ions with target atoms lead to the projectile excitation, but in gases such excitation will be dissipated due to spontaneous radiative transitions to the ground state. In dense materials, however, the probability of the ion excitation is high due to the solid density and the radiative relaxation of excited states does not occur before next collision. The electron loss is the dominant process and the average ion charge is shifted to higher values inside solids. BL theory was

confirmed by experiments on the interaction on heavy ions with different density targets [Nikolaev et al., 1963, Franzke et al., 1967, Ryding et al., 1969].

More recently, Betz and Grodzins made changes to the theory of the density effect in solids. As follows from their model, the increase of the charge occurs directly behind the solid target due to multiple Auger emission [Betz and Grodzins, 1970]. However, the experimental work of Baragiola *et. al* on the Auger decay of 48 - 722 keV argon ions emerging from carbon foils did not show the influence of the Auger process on the difference between the average charge in gaseous and solid targets [Baragiola et al., 1976].

A detailed study of the observation of a gas-solid difference in the stopping powers was carried out at the Darmstadt accelerator facility UNILAC using krypton, xenon, lead and uranium projectiles in the energy range of 1-10 MeV/u [Geissel et al., 1982]. It was observed for the first time in experiments with 3.6 and 7.9 MeV/u uranium projectiles that the stopping power in gases is lower by up to 20% than in solids.

The systematic study of the stopping power of heavy ions in gases during 1984-1985 showed results, which are not in good agreement with BL theory. The Bimbot's group in Orsay investigated the gas-solid effect for five projectiles (neon, argon, copper, krypton and silver) of 2-13 MeV/u energy in twelve gaseous stopping media [Bimbot et al., 1989]. It was observed no gas-solid difference for neon ions in comparison to the heavier projectiles. It should be denoted that the lack of knowledge about the gas-solid difference in stopping powers still exists.

2.5.2 Theoretical explanation

The changing of the projectile bound electron structure due to collisional processes underlies of the target density effect. The influence of the density effect depends on the projectile energy, target density and atomic features of the colliding particles, i.e. excitation, ionization, electron capture cross sections and radiative decay rates of the projectiles. The dependence of collisional cross sections and radiative decay on the atomic number of projectile ions and target atoms was previously described in this chapter.

In physics of atomic collisions a term **rate coefficient** of the process is applied. The rate coefficient of the collisional process is introduced as

$$R_{coll} = N_T v \sigma_{ion}, \quad (2.52)$$

where N_T is the target density in at/cm^3 , v is the projectile velocity and σ_{ion} is the ionization cross section. The quantity R_{coll} characterizes the number of interactions per unit time and has dimension of s^{-1} . The non-collisional process

is characterized by radiative decay A (see subsection 'Radiative decay' of this chapter).

In a high-density target collisions occur with a high probability. The bound electrons of the incident ions can be directly ionized, but they also can be excited. The time between collisions is not enough to allow relaxation of excited states to the ground state before next collision occurs. Therefore, through successive collisions with target atoms the ions from these excited states can be also ionized. It leads to the higher population of excited states and increase of the effective ionization rate

$$\sigma_{ion}^{eff} = P_{n_0}\sigma_{ion}(n_0) + P_n^*\sigma_{ion}(n) + P_{n+1}^*\sigma_{ion}(n+1) + \dots, \quad (2.53)$$

where n_0 and n , $n+1$ are, respectively, the ground and excited states of incident ions, σ_{ion} is the ionization cross section of projectiles, P are populations of the ground and excited (with asterisk) states. The ionization cross sections of highly excited n -states are quite large and increase as $\sigma_{ion}(n) \sim n^2$ [Sobelman et al., 1995]. Some increase of the excited state populations with higher density leads to the increase of the projectile ion charge in dense matter. There is the highest possible quantum number n_{cut} above which the excited ions with $n > n_{cut}$ are ionized due to successive collisions with the target particles. The ions in the states with $n \leq n_{cut}$ decay to the lower states via radiative channels. As a result, the total capture cross section can be determine as the sum of the partial capture cross sections σ_n from the ground state n_0 up to a limited number of the excited states n_{cut} [Shevelko et al., 2005]:

$$\sigma_{ec}^{tot} = \sum_{n=n_0}^{n_{cut}} \sigma_{ec}(n). \quad (2.54)$$

The cut-off principle quantum number n_{cut} can be estimated from the balance between a competition of radiative decay and ionization rate:

$$A(n_{cut}) = N_T v \sigma_{ion}(n_{cut}). \quad (2.55)$$

In a low-density target the excited projectiles can be created in any n state via electron capture [Shevelko et al., 2005]:

$$\sigma_{ec}^{tot} = \sum_{n=n_0}^{\infty} \sigma_{ec}(n). \quad (2.56)$$

There is no influence of the density effect on the ionization cross section. The relaxation of excited states to the ground state occurs via radiative decay. Therefore, the effective ionization rate is defined mostly by the ground state:

$$\sigma_{ion}^{eff} = P_{n_0} \sigma_{ion}(n_0). \quad (2.57)$$

One can make some estimates the ratio of collisional and radiative rates by the branching factor

$$\beta = \frac{R_{coll}}{A}. \quad (2.58)$$

It is interpreted in the following way: by increase of the target density, the rate of collisional processes is governed by depopulation of the ion excited states, $\beta \gg 1$. If the radiative decay becomes dominant in the depopulation of excited states, then $\beta \ll 1$. If $\beta \sim 1$ ($R_{coll} \sim A$) the dependence on the target density is complicated.

The corresponding ionization and radiative rate coefficients are written as

$$R_{coll} = \frac{N_a n^2}{Z_P^2 v}, \quad (2.59)$$

$$A = \frac{Z_P^4}{n^5}, \quad (2.60)$$

where Z_P is the atomic number of projectile ions, n is the principle quantum number. As it should be

$$\beta = \frac{N_a n^7}{Z_P^6 v}. \quad (2.61)$$

As follows from this treatment the influence of the target density effect depends on the atomic parameters of the projectile ions and target atoms as well as collisional and radiative decay rates of particles. The same target density can provide 'solid' conditions for projectile ions with low atomic number and low energy, and 'gas' conditions for high Z_P and high energy.

Chapter 3

Experimental setup and method

The experimental part of the work is discussed in this chapter. In previous investigations, the stopping process in matter was traditionally analyzed for ions emerging from the target. The ion energy loss was determined using e.g. the time-of-flight method and the ion charge state distribution was analyzed e.g. by means of a magnetic spectrometer. A novel diagnostic method of the stopping process, the method of X-ray spectroscopy of K-shell radiation, is presented in this work. It allows to estimate the ion charge states at all velocities during the stopping process **inside matter**. The main experimental goal of the presented work was: 1) to investigate the charge state as function of velocity during the slowing-down process of heavy ions inside solids and gaseous targets; 2) to show the evidence of the influence of the target density on the stopping process. The following experiments were carried out at the Universal Linear Accelerator (UNILAC) of the Gesellschaft für Schwerionenforschung (GSI, Darmstadt). The measurements were performed at the Z6 experimental area (figure 3.1).

3.1 UNILAC facilities

The high frequency accelerator UNILAC offers outstanding possibilities for experiments with heavy ion beams to investigate the properties of matter (figure 3.1).

The accelerator provides pulsed ion beams for experiments at the energy range of 1.4-15 MeV/u. It is able to accelerate all elements from proton up to uranium. Three different injectors are in use for the UNILAC, equipped with different ion sources [Spädtke, 2003]. The ion beam is generated at one of the three preinjector terminals. The standard injector with PENNING ion source and the high current injector (with CHORDIS or MEVVA ion source) supply the next section of UNILAC with the injection energy of 2.2 keV/u. The PENNING ion source is operated in a pulsed mode, typically 50 Hz with pulse length from 2 to 6 ms.

CHORDIS or MEVVA ion sources are regularly operated in a pulse mode up to 50 Hz and pulse length from 0.5 to 5 ms.

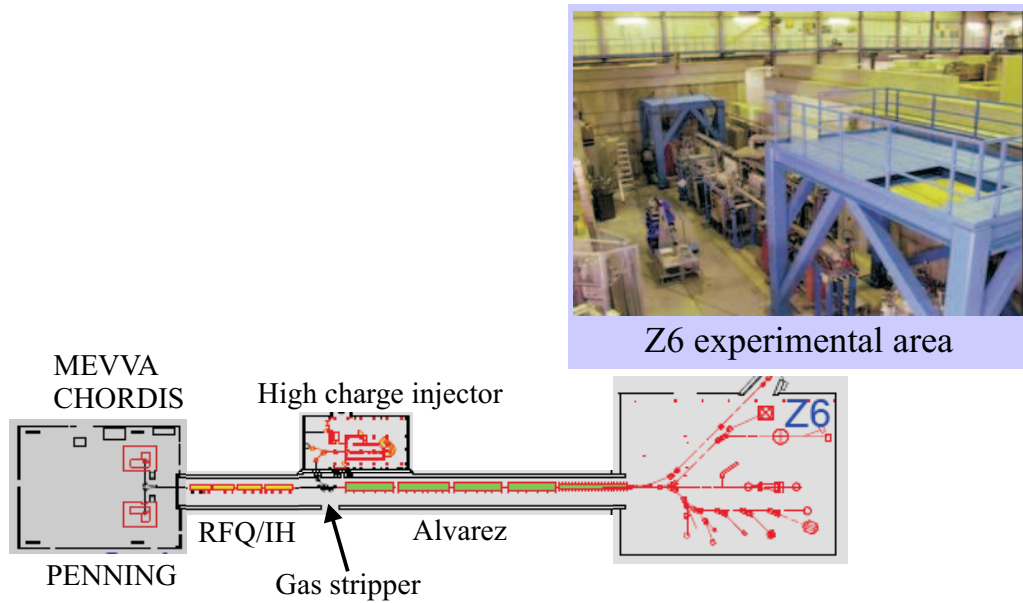


Figure 3.1: Schematic view of the Universal Linear Accelerator at the Gesellschaft für Schwerionenforschung and the Z6 experimental area.

The ion beam from the injector is extracted to the section, where it is accelerated from 2.2 keV/u up to 1.4 MeV/u. This stage of the accelerator consists of the RFQ (Radiofrequency Quadrupole) and two cavities of IH-DTL (Drift Tube Linac). The RFQ works with a frequency of 36 MHz. Then ions pass through a gaseous target, where they undergo strong collisions and are stripped to different higher charge states. One of the charges is selected for further acceleration in the next Alvarez section.

In parallel to the RFQ/IH section an additional injector, the "high-charge injector", is operated. It uses a special ion source known as electron cyclotron resonance source (ECR), which enables to produce highly charged ions in a wide mass range, but with lower intensity. The ECR operates with a frequency of 108 MHz. The highly charged ions from the ECR ion source are preaccelerated in a very compact IH-accelerator. After that they can be injected directly into the Alvarez section. The high-charge injector was used to generate the ion beam for presented experiments.

The ions are accelerated further in the Alvarez structure, which operates with a frequency of 108 MHz. It is possible to reach the energy up to 11.4 MeV/u for all ions, a value corresponding to 16 % of the speed of light.

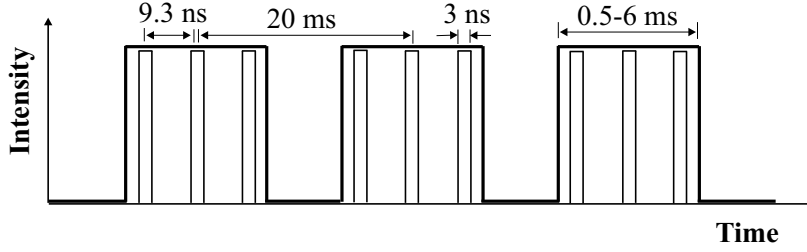


Figure 3.2: Time structure of the UNILAC ion beam divided in macro pulse from the network frequency of 50 Hz and micro pulse with a frequency of 108 MHz.

The time structure of the radiofrequent accelerated ion beam is divided in a macro- and a microstructure (figure 3.2). The macrostructure arises from the network frequency of 50 Hz with a pulse length up to 6 ms with an interval of 20 ms.

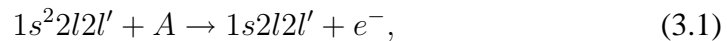
The ion beam from the accelerator are distributed to the UNILAC experimental area and used for low energy experiments. One of them is the Z6 experimental area.

3.2 K-shell projectile radiation as diagnostic method

In experiments on the interaction of fast heavy ions with matter K-shell radiative transitions of ions were used to determine the projectile charge state and velocity during the ion stopping process.

The spectroscopic method is based on the measurement of the characteristic emission of projectile ions excited in collisions with target atoms. This radiation proceeds predominantly via resonant radiative transitions into the ion ground state. Their photon energies for elements with a nuclear charge of 6 - 30 cover wide VUV and X-ray regions depending on the amount of bound electrons of the projectile (ion charge state).

In close collisions of fast heavy ions with matter the ionization of the K-shell electron has a high probability. Let's consider the K-shell photon production in the case of Be-like ion $1s^2 2l 2l'$ for KLL state (figure 3.3). If the interaction between the projectiles and target atoms is sufficiently strong to ionize the projectile K-electron, that a vacancy in the K shell is created (figure 3.3a):



where A is the target atom. $1s 2l 2l'$ is the unstable double excited level (au-

to ionization state), which can decay via the radiative decay (figure 3.3b) or via the Auger decay (figure 3.3c).

In the first case an electron from the higher L shell makes a transition into the K shell to fill the gap. A quantum of electromagnetic radiation is emitted in the form of a photon (K_α -line):

$$1s2l2l' \rightarrow 1s^22l + h\nu. \quad (3.2)$$

If the transition takes place from the M shell into the K shell, the so called K_β -line is appeared.

Also, the emitted energy can be transferred to an bound electron of the L shell with a non-radiative transition. This electron will be ejected into continuum if this energy is enough to ionize it. The electron is called the Auger electron:

$$1s2l2l' \rightarrow 1s^2 + e^-. \quad (3.3)$$

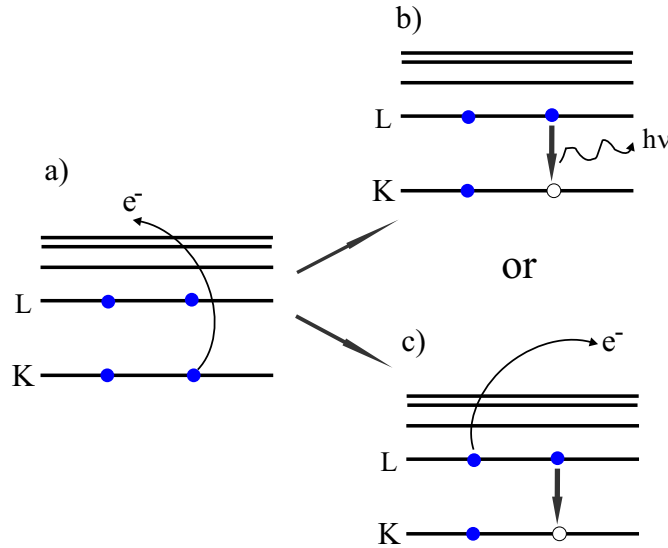


Figure 3.3: Schematic view of the K-shell projectile radiation. The creation of KLL double excited states in Be-like ion due to the ionization of the projectile K-electron in collisions with target atoms (a). The double excited level can decay via the radiative decay with the emission of the K_α -photon (b) or via the Auger decay with the ejection of an electron into continuum (c).

The energy of K-shell radiative transitions does not change significantly with the ion charge due to shielding effect produced by bound projectile electrons. K-shell ionization cross sections depend on the projectile ion energy and slightly on the projectile charge state. It is possible to observe all projectile charge states by

the same X-ray detector. Figure 3.4 shows the charge and energy dependence of K-shell ionization cross sections of calcium and magnesium ions interacting with SiO_2 molecules. The cross sections were calculated by the LOSS code described in the previous chapter [Shevelko et al., 2001].

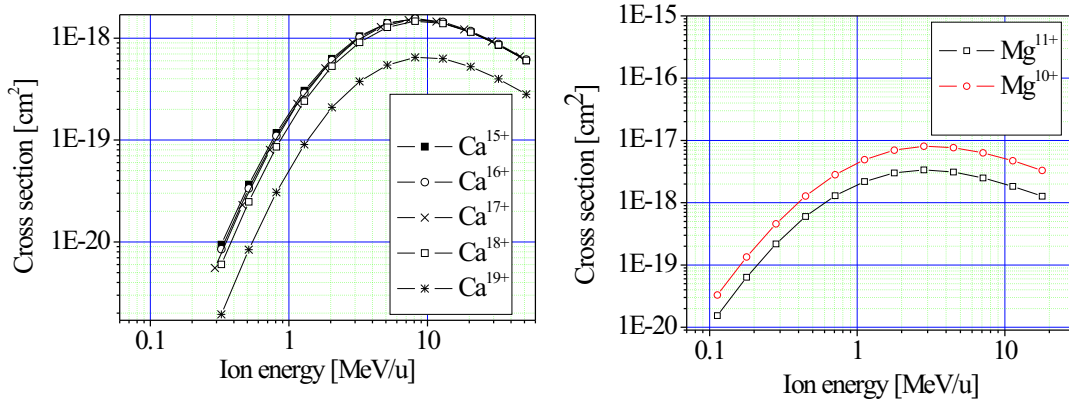


Figure 3.4: K-shell ionization cross sections of Ca^{Z+} and Mg^{Z+} ions colliding with SiO_2 molecules as function of the ion energy, calculated by the LOSS code.

3.3 Experimental scheme

The spectroscopic method discussed above was used in experiments on the penetration of $^{48}\text{Ca}^{6+}$ - $^{48}\text{Ca}^{10+}$ and $^{26}\text{Mg}^{5+}$ ion beams with initial energies of 5.9 MeV/u and 11.4 MeV/u into two different types of targets: SiO_2 aerogel and gaseous target. The principal experimental scheme is presented in figure 3.5.

The heavy ion beams were delivered to the target chamber evacuated to 10^{-6} mbar with a focusing spot of 2 mm on the target. The pulsed ion beam current was varied from 0.1 to 0.5 μA for aerogels and 0.1-0.2 μA for gaseous targets. The macro pulse duration was 2-5 ms with a frequency of 2-5 Hz. The exposure time needed to collect X-ray spectra for aerogel was 1.5-2 hours and 11-12 hours for gaseous medium.

X-ray projectile radiation has been observed with a high spatial and spectral resolution by means of a focusing crystal spectrometer and recorded using X-ray film.

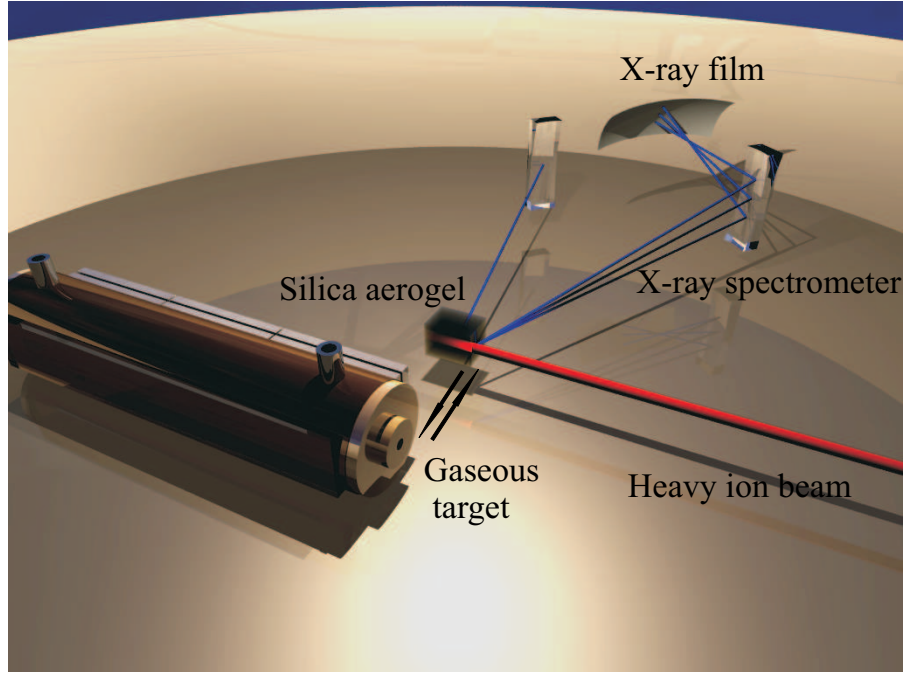


Figure 3.5: *Experimental setup for the investigation of the K-shell projectile and target radiation. Silica aerogel and gas were used as a target material. The K-shell spectra were registered using a focusing crystal spectrometer and recorded with X-ray film.*

3.4 Target material

The target material for presented experiments was chosen with the purpose to investigate two effects. One of them is the spatially resolved analysis of the ion stopping process inside solid matter. A target with the aerogel structure provides increased ion stopping range and gives the possibility to resolve the dynamics of the projectile radiation in solid structure. The second purpose was to show the influence of the target density on the charge state distribution inside matter. Argon and neon gas with a pressure of 1.75 - 1.9 bar and silica aerogels with 0.15 - 0.023 g/cm³ mean densities were used to compare the ion charge state distribution in low and high density media.

3.4.1 Silica aerogel

Spatially resolved measurements are practically impossible in solids. Because of their high density the stopping length of heavy ions with an initial energy of 5.9 MeV/u and 11.4 MeV/u calculated with the SRIM code is about of 50-100 μ m

[Rosmej et al., 2002]. In order to stretch the ion stopping path a new type of target material - silica aerogel - was used (figure 3.6).

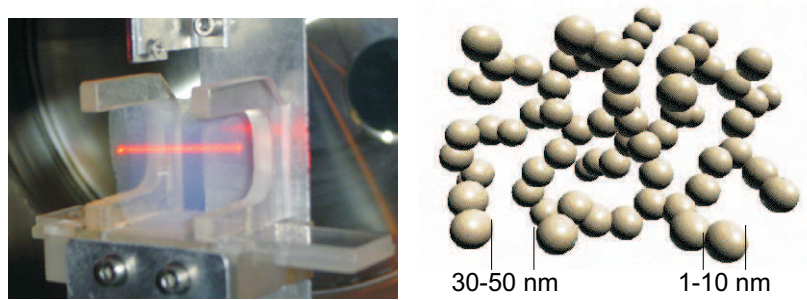


Figure 3.6: Silica aerogel: view and structure. On the left picture the piece of aerogel is fixed with the target support in the experimental chamber.

Silica aerogel is a transparent material, it looks like glass and feels like solidified smoke. The aerogel consists of bounded silicon and oxygen atoms joined into beads of 1-10 nm in diameter randomly linked together in a three-dimensional open structure with pores less than 30-50 nm between them [Borisenko and Merkuliev, 1996]. The combination of the high porosity and extremely small pores provides its extreme properties, such as high temperature stability, excellent thermal insulating properties and extremely large surface area. An important advantage of the non-organic aerogel is the high transparency for X-ray radiation in the range of the photon energy observed in the experiments. Silica aerogels with low mean densities of 0.15 - 0.023 g/cm³ transmit 30% - 95% X-ray radiation of 1.5 keV - 4 keV photon energy.

The exotic nanometer structure of the aerogel provides expanded interaction volume with small spatial gradient. It allows to stretch the ion stopping length by 10 - 100 times in comparison with solid quartz and resolve spatially the projectile radiation dynamics.

3.4.2 Gaseous target

In order to demonstrate the influence of the target density on the projectile charge state distribution inside matter, experiments with 1.75 bar argon gas and 1.9 bar neon gas were realized. The stopping process of swift heavy ions in gaseous matter was investigated in visible and X-ray ranges.

The gaseous target was designed as a massive cylindrical copper tube with the length of 210 mm and 30 mm inner diameter (figure 3.7).

A 5 μ m Havar foil separated the vacuum from the gas pressure region. The foil has density of 8.3 g/cm³. It consists of cobalt (42 %), chromium (20 %),

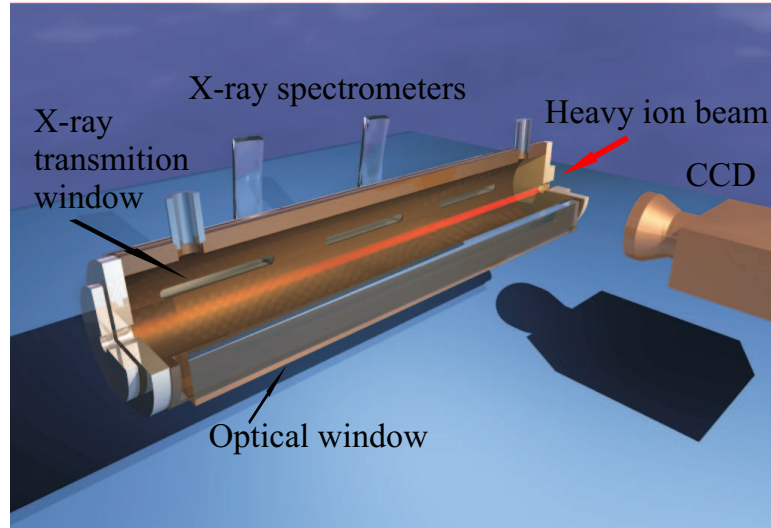


Figure 3.7: Schematic view of the gaseous target used in the experiments (in section). It is constructed as a massive cylindrical copper tube filled with Ar or Ne gas. Three windows covered with $5\ \mu\text{m}$ Havar foil along one side of the target were used to transmit X-ray radiation. The spectra were recorded with focusing crystal spectrometers. A quartz window on the opposite side served to register visible image of the ion beam-gas interaction region using CCD camera.

nickel, tungsten, molybdenum, manganese and iron. When the ion beam penetrates through this high-strength non-magnetic metal alloy, it is stripped to a higher charge state.

Three rectangular windows along one side of the target were used for X-ray diagnostics. They have a length of 40 mm and were oriented along the ion beam propagation. The distance from the entrance to the beginning of the first X-ray window was 20 mm. The windows were covered with $5\ \mu\text{m}$ Ti foils to transmit X-ray emission at 3-4 keV. A 180 mm long quartz window was placed on the opposite side of the target to recorder visible radiation from the interaction zone.

In order to refresh the gas in the target tube during long time exposition of X-ray film a special gas flow was designed (figure 3.8). The gas flow was established through income and outcome apertures for the gas in the target. Two needle valves were used to regulate the pressure of the gas in the target. The gas pressure was measured by means of a manometer placed between the entrance needle valve and the gaseous target. The gas flow system was connected to the gaseous target in the vacuum chamber using a special flange with two apertures for the entrance and exit of the gas.

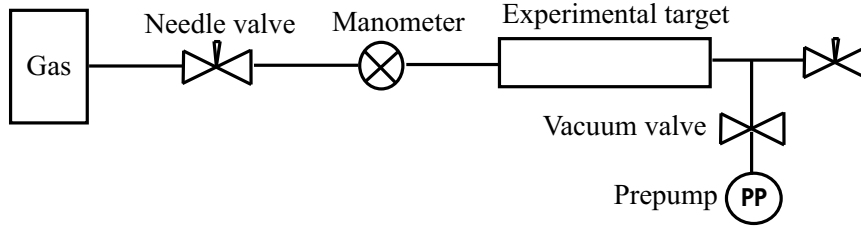


Figure 3.8: Scheme of the gas flow for experiments with the gaseous target.

3.5 Diagnostics of the projectile radiation

The study of the slowing-down process of fast heavy ions inside matter was realized by means of X-ray spectroscopy of K-shell projectile radiation. In order to resolve the projectile charge state distribution and ion velocity dynamics a sensitive X-ray spectrometer was used. A spectral resolution $\lambda/\Delta\lambda = 1000$ is necessary to distinguish the K_α -radiation caused by different ion charges. The high spectral ($\lambda/\Delta\lambda = 2000 - 5000$) and spatial (30-130 μm) resolutions were archived using two-dimensionally curved Bragg crystal and Kodak X-ray film.

3.5.1 Spectrometer design and method of the observation

X-ray spectroscopic techniques enables to measure the most important information during the stopping process: the dynamical relationship between the projectile charge state distribution and ion velocity inside matter. High spatial and spectral resolutions are required to obtain this information [Boiko et al., 1985]. Bragg diffraction crystal spectrometers provide excellent energy resolution and cover X-ray range from a few kiloelectron volts to a few thousand kiloelectron volts. If the crystal is curved, a high spatial resolution is obtained [Thoe, 1986].

Focusing Spectrometer with Spatial Resolution (FSSR) used in our experiments employs a spherically bent crystal as dispersive element (figure 3.9)[Faenov et al., 1994, Pikuz et al., 1995, Skobelev et al., 1995, Young et al., 1998].

The FSSR design combines two aspects:

1. In the plane of dispersion the crystal works on the principle of the constructive interference in reflection from the crystal lattice for a given angle and X-ray energy (figure 3.10 a). The angle reflected at particular wavelength is described by Bragg's law:

$$m\lambda = 2d_m \sin \theta, \quad (3.4)$$

where λ is the X-ray wavelength, m is the order of the reflection, d_m is the

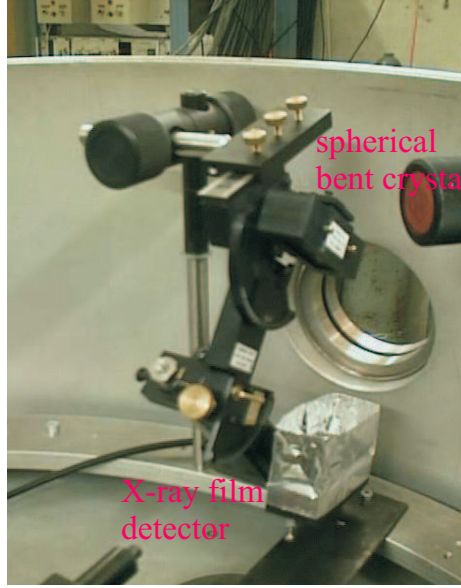


Figure 3.9: *Focusing Spectrometer with Spatial Resolution in the experimental chamber.*

crystal plane spacing for m th order of reflection and θ is the Bragg angle for the central wavelength.

2. In the sagittal plane the crystal reflects as a spherical mirror (figure 3.10 b):

$$1/a + 1/b = 2 \sin \theta / R, \quad (3.5)$$

where R is the radius of curvature of the spherical surface, a is the distance between the source and the mirror (crystal), b is the distance from the mirror to the object plane (X-ray film). In this case the plane of dispersion is defined by X-ray source, the crystal pole and the image of the source. The sagittal plane is perpendicular to the dispersion plane.

The scheme has a spatial resolution in the sagittal plane, so the length of spectral lines at the detector is a magnified length of the ion beam-target interaction zone. Linear magnification in this plane is defined by the ratio $M = b/a$.

In order to span a large energy range and receive the best possible spectral resolution the crystal and detector are located on the Rowland circle at the distance $b = R \sin \theta$ (FSSR-1D scheme). This geometry requires that the angular size of the source as viewed by the crystal is large enough to span the required Bragg angles. In such position the spectral resolution is independent on the X-ray source size. In order to obtain a focused image of the source on the detector the source is placed at the distance $a = R \sin \theta \div \cos 2\theta$ as follows from eq.(3.5). This distance corresponds to the best focusing conditions for sagittal rays on the detector and

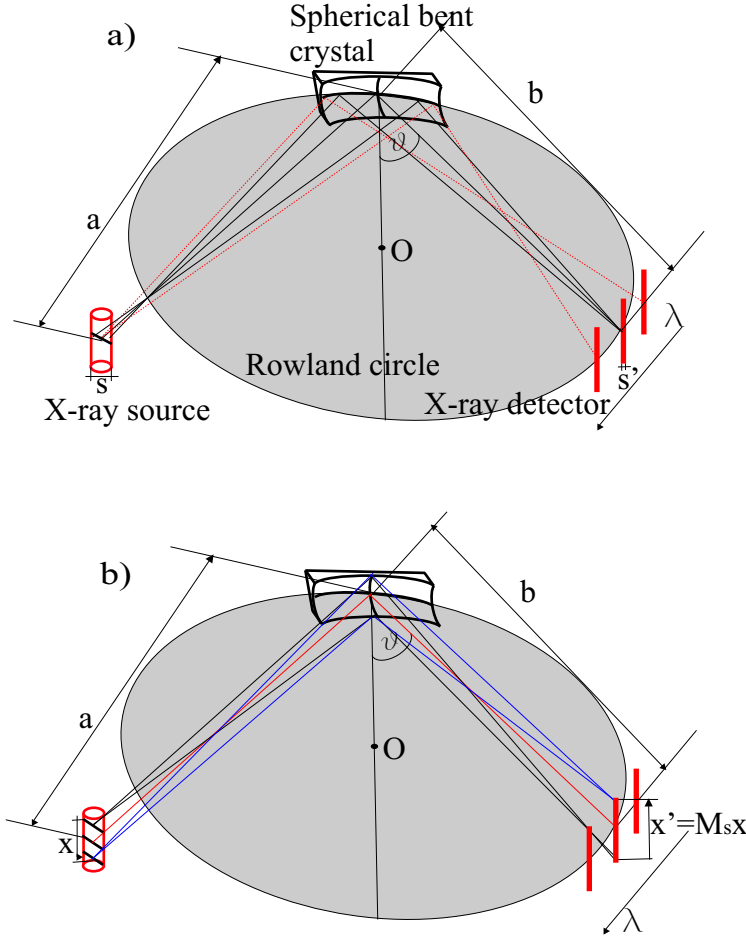


Figure 3.10: *FSSR-1D scheme: a) the formation of the image in the dispersion plane (spectral resolution); b) the formation of the image in the sagittal plane (spatial resolution).*

provides the best spatial resolution. In this case spectrally resolved images of the source with one-dimensional spatial resolution in the sagittal direction are observed. Linear magnification of the source image in sagittal direction is defined by $M_s = b/a = \cos 2\theta$. FSSR-1D allows to receive a high spatial resolution in the sagittal direction and a high spectral resolution in the dispersion plane for sources with any size. The spatial field of view for such spectrometer is very large and is only limited by detector size.

For sources that do not span large angles, the crystal is often used without satisfying the Rowland conditions (figure 3.11). By changing the distance b , i.e. mounting the detector out of the Rowland circle and putting the source at the distance $a = Rb/(2b \sin \theta - R)$ (FSSR-2D scheme) the efficiency of the setup

leads to extended spectral coverage, but the best spatial resolution is achieved as well.

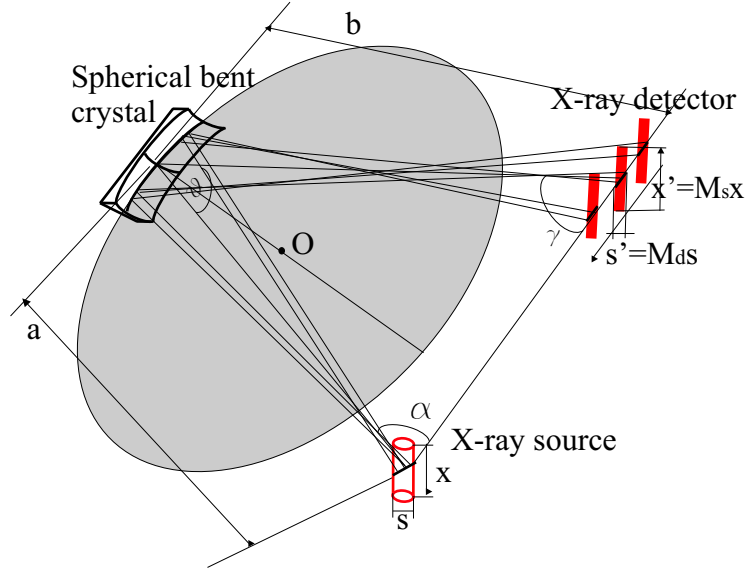


Figure 3.11: *Focusing Spectrometer with Spatial Resolution: FSSR-2D scheme.*

In the case of FSSR-2D scheme the spectral resolution depends on the size of the X-ray source, and spatial resolution exists not only in the sagittal direction, but also in the dispersion plane. In the sagittal direction the magnification is $M_s = b/a$. In the plane of dispersion the spatial resolution is not defined by focusing properties of the crystal, but the Bragg reflection. The magnification is $M_d = R[a - \cos \theta(2a \cos \theta - R)] / [(R \cos \theta - a)(2a \cos \theta - R)]$ and depends on the distance between the Rowland circle and detector. There is some relation between the spectral resolution $\lambda/\Delta\lambda$ and the size of the X-ray source in the dispersion plane:

$$\lambda/\Delta\lambda = RB(a, \theta, R)/s, \quad (3.6)$$

where

$$B(a, \theta, R) = 2 \sin \alpha \cot \theta / [(a/R - \sin \theta)(\tan \theta \tan \gamma + 1) + a/R], \quad (3.7)$$

α is the angle between the incident ray and the line connecting the source and its image on the detector, γ is the angle between the reflected ray and the same connecting line. If eq.(3.5) is fulfilled, then $\alpha + \gamma = 2\theta$. The spectral resolution for FSSR-2D scheme could reach a value of $\lambda/\Delta\lambda \sim 3000 - 10000$ even with a big (~ 3 mm) size of X-ray source.

In presented experiments two types of crystal (mica and quartz) were used. Many different varieties of mica and quartz can be found in nature. For mica crystals, it has been shown that high-order reflections can be quite pronounced [Pikuz et al., 1995]. Mica has a good reflectivity in the I-V, VII, VIII, X-XIII orders of reflection. It allows to cover a spectral range from 0.6 to 8.3 keV using the same crystal in different orders of reflection. Quartz crystal diffracts X-rays in a smaller spectral range from 1.5 to 8 keV in the I-IV orders of reflection, but has higher reflectivity in comparison with mica [Sanchez del Rio et al., 2004]. In the presented experiments mica ($2d = 19.937\text{\AA}$) and quartz ($2d = 8.492\text{\AA}$) crystals with bending radius of 150 and 100 mm were used. The size of illuminated surface was about $14 \times 45\text{ mm}^2$, which corresponds to the sagittal and dispersion plane, respectively.

X-ray film served as detector for the K-shell radiation. Quantitative measurements of X-ray spectra were determined by the number of incident photons, which activate the grains in the film emulsion, per unit square. The measured intensity is a function of the relative darkness of an image on the film, which is called optical density. The photographic density is determined by measuring the incident to transmitted light (photon counts) ratio and expressed as logarithm. Kodak Direct Exposure Film (DEF), which has a high sensitivity in the photon region of 1-10 keV, was used for the spectroscopic analysis [Henke et al., 1986]. In some last experiments the radiation was recorded by Kodak RAR 2492 film, which is sensitive in the low energy region of 0.1-3 keV [Henke et al., 1984]. The small size of the silver bromide film grain ($1.6\text{ }\mu\text{m}$ of Kodak DEF film and $1\text{ }\mu\text{m}$ of Kodak RAR film) provides a high spatial resolution. X-ray spectra were processed with 10 000 dots per inch (dpi) scanner. The film holder was protected by two layers of $1\text{ }\mu\text{m}$ polypropylene filters coated with $0.2\text{ }\mu\text{m}$ layers of aluminium on both sides. Such kind of filters transmits the soft X-ray radiation and blocks a background radiation with low photon energy.

In experiments spectrometers with film holders were mounted at different angles to the direction of the ion beam propagation.

3.5.2 Analysis of the ion velocity dynamics

The radiation of projectiles moving with velocity of 10% of the speed of light exhibits relativistic Doppler Effect. The projectile ions penetrate into the target with the maximal velocity. Then passing through the medium they lose their energy. Therefore, the line Doppler shift is decreased continuously with the ion penetration depth and, as a result, spectral lines become tilted (figure 3.12). This effect was observed for the first time and used for spatially resolved measurements of the projectile velocity along the stopping path in matter [Rosmej et al., 2003].

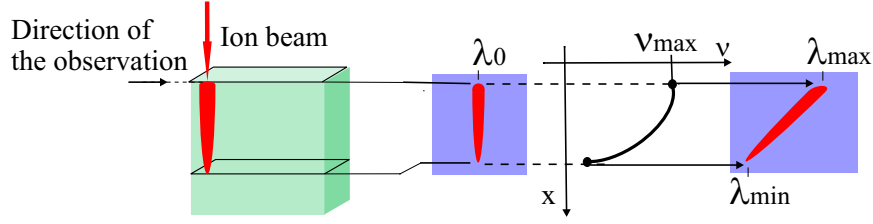


Figure 3.12: *The line Doppler shift: projectiles penetrate into the target and undergo the Doppler Effect due to the ion deceleration in matter.*

The ion projectile velocity inside the interaction volume was calculated using the following equation for the total line Doppler shift:

$$\lambda_D = \frac{\lambda_0}{\sqrt{1 - (v/c)^2}} + \frac{\lambda_0(v/c) \sin \varphi}{\sqrt{1 - (v/c)^2}}, \quad (3.8)$$

where λ_D is the measured wavelength, λ_0 is the wavelength in the rest, v is the projectile ion velocity, c is the speed of light, φ is the angle between the normal of the beam line and the direction of the observation .

Eq.(3.8) consists of the transversal and longitudinal Doppler components. The transversal value depends only on the projectile velocity. The longitudinal Doppler component depends on the projectile velocity and the angle of the observation. Figure 3.13 shows three cases of the Doppler line shift in dependence on the angle of the observation to the normal of the ion beam trajectory.

If the radiation is observed at the angle less than 90° to the ion beam propagation direction, the longitudinal Doppler component is positive. The sum of longitudinal and transversal components gives a large line shift towards the long-wavelength range, the so called red Doppler line shift.

By observation perpendicular to the ion beam there is no dependence on the angle of the observation. The transversal red Doppler shift is dominant. Therefore, spectral lines are shifted to the long-wavelength side, but by smaller value.

The last case corresponds to the blue Doppler shift. The observation of the radiation at the angle larger than 90° to the ion beam propagation direction gives negative longitudinal Doppler component. The spectral lines are shifted to the short-wavelength range.

The accuracy of the projectile velocity measurements is determined by spatial resolution.

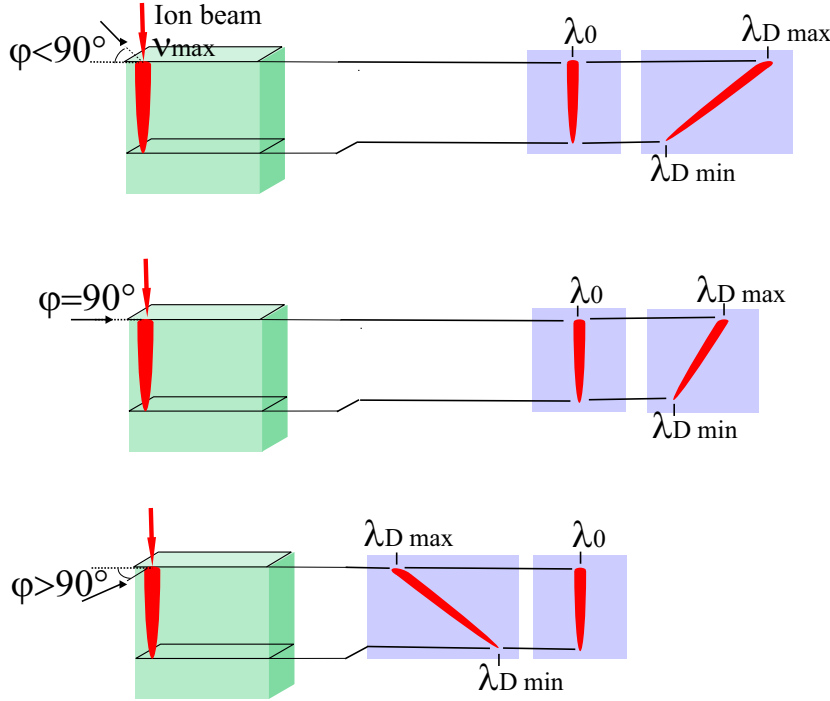


Figure 3.13: Three cases of the Doppler line shift in dependence on the observation of the radiation to the ion beam propagation direction: red Doppler shift, transversal red Doppler shift and blue Doppler shift.

3.5.3 Visible diagnostics of the gaseous target

During the interaction of fast heavy ions with matter variations of the target material parameters in the interaction region can change the energy loss significantly [Tahir et al., 2003]. In experiments on the interaction of heavy ions with gaseous target the energy deposition leads to heating of the medium and, as a result, change its density in the interaction zone.

The density of argon gas in the interaction area with 5.9 MeV/u calcium ion beam has been investigated in the presented work. The high intensity of the ion flux during the macro pulse of 5-5.5 ms led to heating of the gaseous medium in the ion beam-gas zone and varied the density along the ion beam stopping path and radius with a time. The construction of the gaseous target is described above in section 'Target material'. The pressure in the target was about 1.75 bar in order to provide a complete stopping of the ion beam. The visible image of the ion beam-gas target interaction region was registered through a 180 mm long quartz window by intensified gated CCD camera Dicam Pro. This device is a high performance intensified system with gating times down to 1.5 ns, with 12-bit dynamic range

and a high resolution sensor of 1280×1024 pixel. The camera was placed outside the vacuum chamber perpendicular to the ion beam propagation and covered the full ion stopping path.

Visible images of the ion stopping range during the macro pulse were recorded with a time resolution of $100 \mu\text{s}$. Using the dependence of the ion stopping length on the target density from the numerical SRIM code, the gas density was calculated in dependence on the measured stopping range. The simulations of the gas density in the interaction region was done with the VarJet code.

The **SRIM** code is a Monte Carlo computer program developed by J.Ziegler to calculate the stopping and range of energetic ions in solid targets [Ziegler et al., 1985]. It is based on the Bohr-Bethe-Bloch theory. The code is applicable to a wide range of incident energies from keV to several MeV and to all ion-target combinations. SRIM is available in the Internet (www.srim.org).

The **VarJet** code is a numerical simulation of the hydrodynamic response of the gas heated with the ion beam recently developed by D.Varentsov [Varentsov, 2006]. This code is able to solve 2D full time-dependent Navier-Stokes equations for multicomponent gas mixtures, including viscosity, heat conductivity and diffusion effects. The initial and boundary conditions were taken such as in the experiment whereas the beam induced heating of the gas was calculated using SRIM stopping power data and neglecting radiative energy dissipation.

Chapter 4

Experiments and data analysis

Experiments on the interaction of fast heavy ions with matter and analysis of the results are presented in this chapter. The description of the diagnostic method has been given in chapter 3 of this work. The operation of the focusing crystal spectrometer with spatial resolution to observe the K-shell spectra as well as type of targets have been also discussed in the previous chapter.

4.1 Experimental results with solid targets

In experiments on the interaction of fast heavy ions with solids the K-shell projectile and target radiation have been measured. Spatially resolved analysis of the stopping process inside solid targets has been performed using low density silica aerogels. The ion velocity dynamics inside the interaction volume was determined using the line Doppler shift of the projectile spectra.

4.1.1 Silica aerogel as a solid target

A wide variety of silica aerogels was used in order to stretch the ion stopping path in solid into the range needed to obtain a spatial resolution of the ion radiation dynamics.

The first experiments have been carried out to prove the possible influence of the porous nanostructure on the ion stopping process for given experimental conditions. The aerogel can be used as a solid if the time-of-flight of the ion inside the pore in vacuum is shorter than the time scale of the radiative and Auger processes, which lead to the collisionless relaxation of the projectile excited states.

The energy loss and the charge state distribution of 11.4 MeV/u calcium ions interacting with aluminium foils and aerogels with practically the same linear

Experiment	1.1	1.2	2.1	2.2	3.1	3.2
Target material	Al	SiO ₂ aerogel	Al	SiO ₂ aerogel	Al	SiO ₂ aerogel
Volume density, [g/cm ³]	2.7	0.023	2.7	0.048	2.7	0.019
Linear density, [mg/cm ²]	6.9	7.015	13.81	13.6	12.0	12.0
Energy loss [MeV/u]						
Measurement	1.572	1.692	3.141	3.384	2.882	3.061
SRIM data	1.558	1.77	3.283	3.635	2.812	3.16

Table 4.1: *Energy losses of 11.4 MeV/u calcium ions measured after silica aerogels and aluminium foils using the time-of-flight method.*

density were measured after the target and analyzed. The experimental scheme is presented in figure 4.1.

The energy loss measurements were performed using the time-of-flight method (TOF). The method is based on the resonant ion beam acceleration in the radiofrequency quadrupole that leads to a phase synchronization between the beam microstructure and the accelerating radiofrequency (rf) voltage structure at any point along the ion beam line. Micro sphere plate (MSP) with a rise time of 150 ps was used as a stop detector and was positioned at the end of the 473-cm-long flight path after the target. The stop detector signal and the UNILAC rf signal were recorded simultaneously by means of a two-channel digital oscilloscope. In order to initiate a time reference point for the time-of-flight measurements the phase correlation between the ion beam microstructure and rf-signal were measured without the target. Then the target was placed in the ion beam path. A phase shift of the ion beam microstructure relative to the rf-signal was observed. The time difference together with the time-of-flight distance determines the ion energy loss in the target.

The energy loss experiments have been realized for three different linear densities of presented targets and compared with values of the SRIM code. The results are summarized in table 4.1. One can see that experimental results on the calcium ion loss in Al targets are in good agreement with SRIM values. The energy loss in aluminium and aerogel targets is not the same because of not exact target linear density. The difference in Al and SiO₂ atomic structures is about 8%.

The charge state distribution of calcium ions after the penetration of aluminium foils and silica aerogels has been analyzed by means of a magnetic spectrometer. It is based on the deflection of the ion beam in a magnetic field according

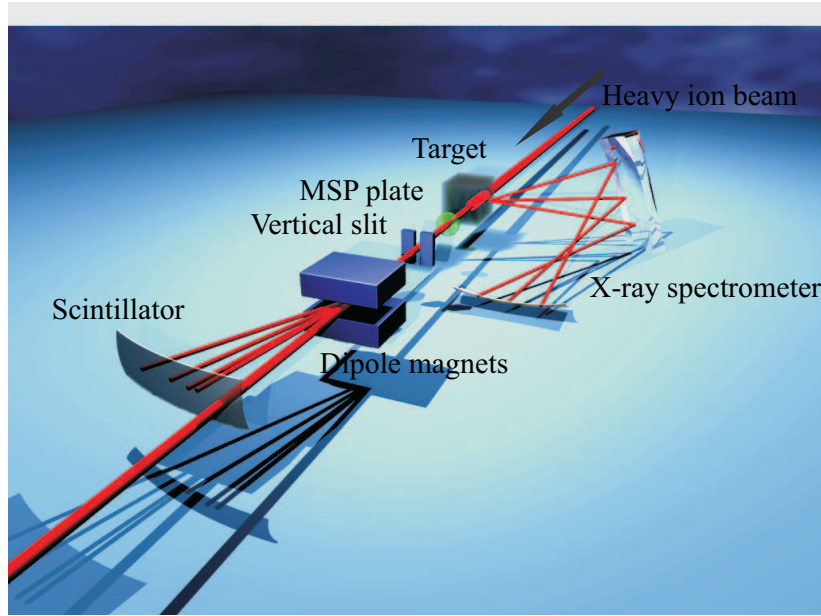


Figure 4.1: *Experimental setup for the measurements of the ion energy loss and charge state distribution of the projectile ions having left the target. The ion beam energy after the target was determined using the time-of-flight method and the ion charge state distribution was analyzed by means of a magnetic spectrometer. The method of X-ray spectroscopy to determine the projectile charge state during the ion stopping process inside the target was used at the same time.*

to their charge-to-mass ratio Q/m and energy. The ions were deviated with 1.8 T dipole magnet and detected by 1 mm plastic scintillator, viewed by a camera, which produces intensified images on the Charge Coupled Device (CCD). The background picture of the foreign lighting and CCD noise was recorded and subtracted for each image. Afterwards, the images were projected along the direction of the dispersion. Since the ion energy after the target is known from the TOF measurements, the charge state distribution of the ion can be determined.

The charge state distribution of 11.4 MeV/u calcium ions penetrating aluminium foil and silica aerogel with linear densities of 13.81 mg/cm² and 13.6 mg/cm², correspondingly, was measured (figure 4.2). The average ion charge after the aluminium target is 18.5 and after the aerogel is 18.2. A small shift along the dispersion direction is due to the difference in the final energy of ions, which was measured 8.3 MeV/u after the aluminium foil and 8.06 MeV/u after the aerogel.

The energy loss and charge state distribution investigated after the aerogel target show a good agreement with results after the aluminium foils. Therefore, the

porous silica aerogel can be used as a solid target for our experimental conditions.

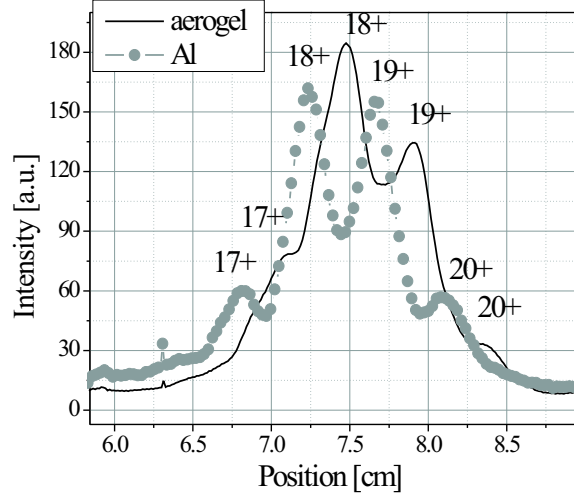


Figure 4.2: Charge state distribution of 11.4 MeV/u Ca beam after the magnetic spectrometer. The black line is the charge state distribution of ions after passing through the Al foil with a linear density of 13.81 mg/cm^2 , the line with symbols corresponds to the charge state distribution after penetration of 0.048 g/cm^3 silica aerogel with a linear density of 13.6 mg/cm^2 .

4.1.2 K-shell target radiation

The K-shell radiation of silicon target atoms was studied in experiments on the interaction of 11.4 MeV/u calcium ions with 2.23 g/cm^3 quartz and 0.04 g/cm^3 silica aerogel.

The K-shell target radiation in the photon energy range of 1.5 keV was resolved spatially by means of a focusing crystal spectrometer. Spherically bent quartz crystal with a radius of curvature of 100 mm was used as dispersive element. The spectral and spatial resolutions were $\lambda/\Delta\lambda = 3000$ and $50\text{-}70 \text{ }\mu\text{m}$, respectively. X-ray spectra were observed perpendicular to the direction of the ion beam propagation and recorded using Kodak DEF X-ray film with optical resolution of 2820 dpi.

In fast ion-atom collisions the production of a K-shell vacancy in the target atom can be accompanied by the production of one or more L- and M-shells vacancies. This process has a high probability. The K-shell X-rays from decays of

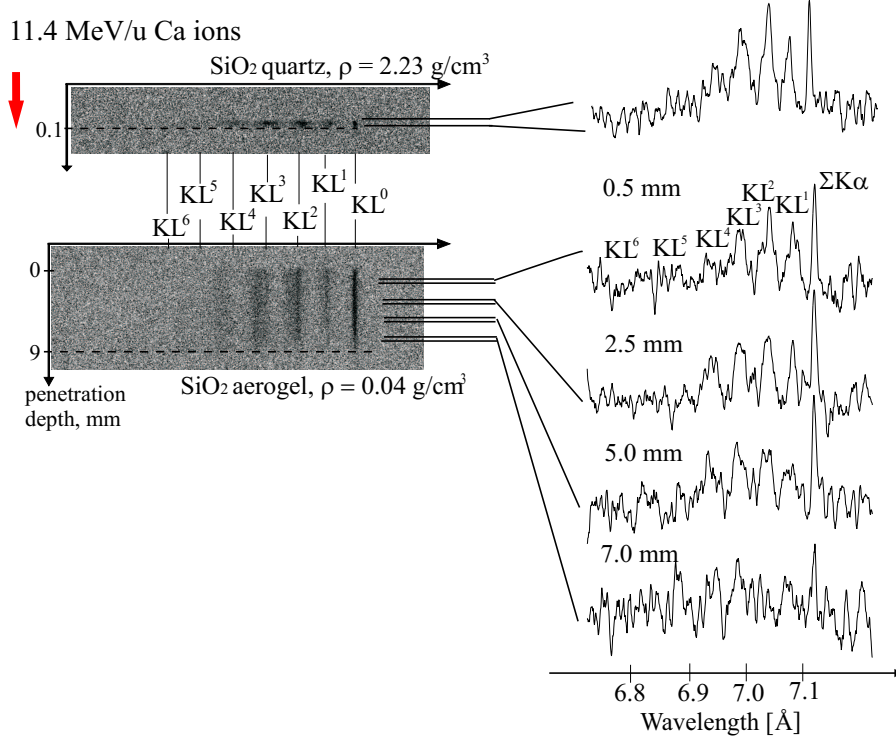


Figure 4.3: Silicon target K_α spectra produced due to irradiation of 1-mm-thick quartz plate with a density of 2.23 g/cm^3 and 25-mm-thick piece of 0.04 g/cm^3 SiO_2 aerogel by 11.4 MeV/u calcium ions. The resolved K_α satellites along the ion beam trajectory in silica aerogel are presented (densitograms).

excited states with different L-shell vacancies are shifted to higher energies than those from a K-vacancy state with a completed L shell. A spectral resolution of the detector better than $\lambda/\Delta\lambda = 1000$ is required to resolve this group of satellites.

The ion beam was fully stopped in 1-mm-thick quartz plate and 25-mm-thick piece of silica aerogel. Figure 4.3 shows Si K_α spectra of quartz and silica aerogel irradiated by calcium ion beam with the initial energy of 11.4 MeV/u. The stopping length of ions in the aerogel reached 9 mm. The corresponding length of spectral lines increased dramatically as well. In contrast to the quartz target spectrum, one can resolve the dynamics of the K_α satellite intensity distribution along the ion beam trajectory due to the change of the energy and the charge of the projectile ions.

Both target spectra show radiative transitions in Si ions having one K-shell va-

cancy and one or more L-shell vacancies. These transitions are usually designated as $K\alpha L^n$, where n is the amount of L-shell vacancies. In the Si target K-shell spectrum radiative transitions in highly ionized Si ions having up to 5 vacancies in the L shell were observed. The line KL^0 accumulates the radiative transitions in Si ions with a filled L shell and different amounts of M-shell vacancies, which are not resolved.

In the K-shell target spectrum resolved along the ion beam path the satellite intensity redistribution was observed. At the end of the ion path, intensities of satellite groups having many L-shell vacancies KL^3 and KL^4 are increasing and even KL^5 satellites appear instead of the disappearing KL^1 . This correlates to the fact that the L-shell ionization probability increases at lower ion energies.

In the presented experiment a strong dependence of the K-shell target spectra on the ion charge state and velocity has been shown. It opens perspectives to use spatially resolved target spectra to analyze the stopping process and ion track formation.

4.1.3 Velocity dynamics

In the next of the performed experiments on the interaction of 11.4 MeV/u calcium ions with 0.04 g/cm³ silica aerogel the K-shell projectile radiation has been studied (figure 4.4).

X-ray projectile spectra were registered using a focusing spectrometer with a spherically bent mica crystal, $R = 150$ mm. The spectral and spatial resolutions archived in the experiment were $\lambda/\Delta\lambda = 2000-5000$ and 30-70 μm , correspondingly. Spatially resolved spectra were observed in the direction of the ion beam propagation at 80° to the ion beam axis. The radiation was recorded using Kodak DEF X-ray film, which was scanned with optical resolution of 2820 dpi.

In the experiment the radiation of Ly_α (Ca^{19+}) and $\text{He}_{\alpha 1}$ (Ca^{18+}) corresponding to the radiative transitions in calcium electronic system with one and two bound electrons were observed. The detailed information about the ion charge state is given in the next subsection.

In contrast to the target K-shell spectra having vertical lines, projectile lines recorded with a spatial resolution are tilted due to the reduction of the line Doppler shift by the ion deceleration in the stopping medium. The ions enter into the target with a maximum velocity, which corresponds to the initial velocity of 4.77×10^9 cm/s. Therefore, the wavelength shift $\delta\lambda_D$ from the position $\lambda_0 = 3.1773 \text{ \AA}$ ($\text{He}_{\alpha 1}$) of the ion in rest due to the Doppler Effect is maximum, $\delta\lambda_D = 0.1301 \text{ \AA}$. By deeper penetration into the target, projectile ions lose their energy and the line Doppler shift is decreasing continuously.

The Doppler Effect observed on the projectile K-shell spectra was used to calculate the ion velocity dynamics inside the interaction volume. The relativistic

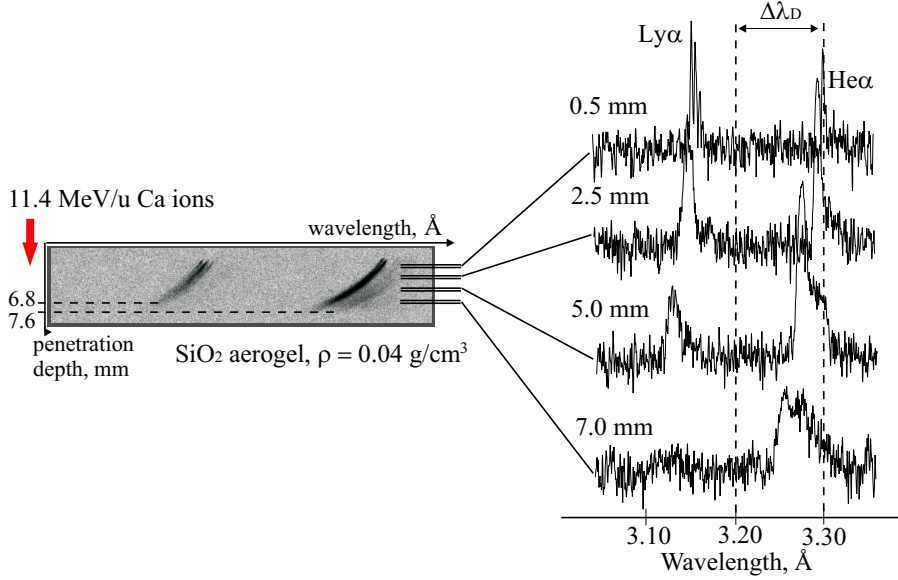


Figure 4.4: *K*-shell spectrum of 11.4 MeV/u calcium ions slowing down in 0.04 g/cm³ SiO₂ aerogel. The densitograms for different penetration depths show the reduction of the line Doppler shift.

equation for the line Doppler shift (eq. 3.8) was used to calculate the projectile velocity in dependence on the ion penetration depth in the target material. The detailed description of the equation has been given in chapter 3 of this work.

From the space-resolved analysis of the relative Doppler line shift $\Delta\lambda_D$, the experimental dependence of the calcium projectile ion velocity on the ion penetration depth in 0.04 g/cm³ silica aerogel was found (figure 4.5). The stopping length calculated with the SRIM code for 11.4 MeV/u Ca ions in 0.04 g/cm³ SiO₂ aerogel was 8.72 mm. However, the radiation of Ly $_{\alpha}$ and He $_{\alpha 1}$ has been recorded at 6.8 mm and 7.6 mm, correspondingly.

At the beginning of Ly $_{\alpha}$ and He $_{\alpha 1}$ line emission the velocity of ions corresponds to the initial 11.4 MeV/u ion beam energy. The ionization length l_{ion} of Ca⁶⁺ ions, which enter into the target, to Ca¹⁹⁺ is calculated as

$$l_{ion} = v_{ion} t_{ion} = v_{ion} \frac{1}{R_{ion}} = \frac{1}{\sigma_{ion} n_e}, \quad (4.1)$$

where v_{ion} is the ion velocity; t_{ion} is the time of the ionization process, which is inversely proportional to the rate coefficient R_{ion} ; σ_{ion} is the ionization cross section of Ca¹⁹⁺ ions colliding with SiO₂ molecules at 11.4 MeV/u (figure 3.4) and equals 6.34167×10^{-19} cm²; n_e is the target density, $n_e = 6 \times 10^{20}$ at/cm³ for

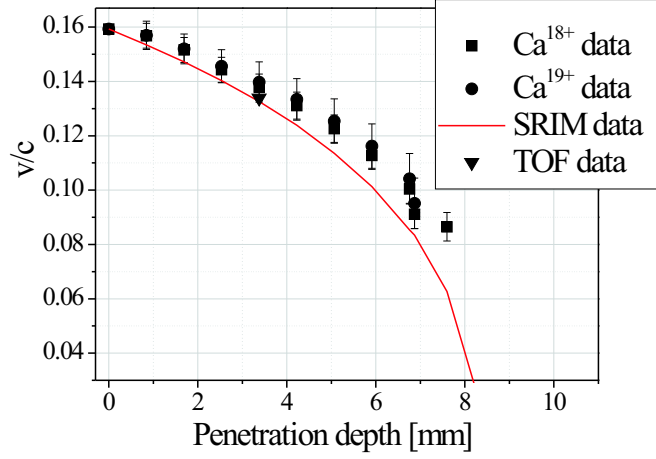


Figure 4.5: The experimental dependence of Ca ion velocity on the penetration depth in $0.04 \text{ g/cm}^3 \text{ SiO}_2$ aerogel. The velocity is normalized to the speed of light. Data measured by means of X-ray spectroscopy (squares and circles) and the time-of-flight method (triangle) are compared with SRIM calculations.

silica aerogel. The estimated ionization length was about $16 \mu\text{m}$, which is below the spatial resolution achieved in the experiment.

The calculations of the projectile velocity were performed for Ly_α (circles) and $\text{He}_{\alpha 1}$ (squares) line emission in dependence on the ion penetration depth. The accuracy of the measurements is determined by a spectral resolution. At the beginning of the ion stopping path the measurement error is about 2 % and becomes larger for smaller ion energies, i.e. for bigger energy losses. At the end of the ion stopping length the error is 14 %. The experimental data were compared to the numerical calculations using the semiempirical SRIM code (straight line) and the time-of flight measurement (triangle). The TOF measurement was performed to 11.4 MeV/u Ca ions emerged from a 3.4-mm-thick piece of 0.04 g/cm^3 silica aerogel. The measured projectile energy was 4 MeV/u and 3.5 MeV/u for Ly_α and $\text{He}_{\alpha 1}$ lines, respectively. The radiation of lines starts to disappear due to low K-shell ionization cross sections at low projectile energies (see figure 3.4).

However, it is possible to analyze the projectile energy below 3 MeV/u for projectile ions with low atomic number having low K-shell electron binding energy. In this connection the experiment on the interaction of 11.4 MeV/u magnesium ions with $0.04 \text{ g/cm}^3 \text{ SiO}_2$ aerogel was carried out. The ion beam was previously stripped in a $5 \mu\text{m}$ Al foil up to bare ions and decelerated down to 11.18

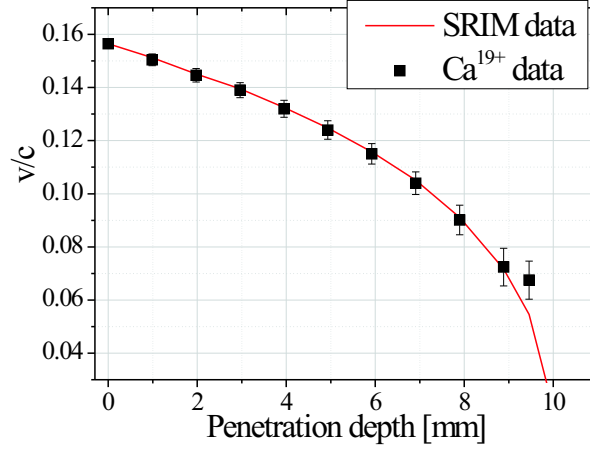


Figure 4.6: The measured dependence of 11.18 MeV/u Mg ions slowing down in 0.04 g/cm^3 SiO_2 aerogel. The measured data (squares) are compared with SRIM calculations (straight line).

MeV/u. The experimental conditions were such as in the experiment with Ca ions described above. The penetration depth of Mg ions in the aerogel calculated with the SRIM code was 10.55 mm, the measured range was 10 mm. Figure 4.6 shows the Mg ion velocity dependence on the penetration depth of Ly_α line emission (squares). The projectile energy measured at the end of the stopping path was 2.06 MeV/u. The experimental error is 2 - 11 %.

4.1.4 Projectile charge states

During the study of the charge state of projectile heavy ions interacting with low-density silica aerogels several series of experiments have been carried out. The performed experiments are summarized in table 4.2.

In the first two experiments the interaction of 5.9 MeV/u and 11.4 MeV/u Ca ions with 0.15 g/cm^3 aerogel has been studied. Using projectile ions with different initial energy, various dynamics of the stopping and radiation processes has been observed. The focusing spectrometers with a spherically bent quartz crystal of 150 mm curvature radius were placed perpendicular to the direction of the ion beam propagation. The spectral resolution achieved in experiments was $\lambda/\Delta\lambda=1000\text{-}3000$, the spatial resolution was 30-100 μm . Spatially resolved K-shell spectra of Ca projectiles in photon energy range of 3-4 keV were recorded by means of Kodak DEF X-ray film and scanned with optical resolution of 2820 dpi.

	1	2	3	4
Projectile ion	$^{48}\text{Ca}^{6+}$	$^{48}\text{Ca}^{6+}$	$^{48}\text{Ca}^{7+}$	$^{48}\text{Ca}^{10+}$
Ion energy, E [MeV/u]	5.9	11.4	11.4	11.4
Target material	SiO ₂ aerogel	SiO ₂ aerogel	SiO ₂ aerogel	SiO ₂ aerogel +5 μm Havar
Target density, ρ [g/cm ³]	0.15	0.15	0.04	0.023
Spectrometer setup				
Dispersive element	Quartz, 2d=4.9Å	Quartz, 2d=4.9Å	Mica, 2d=19.9Å	Mica, 2d=19.9Å
Radius of curvature, [mm]	150	150	150	150
Reflection order	I	I	V	V
Spectral range, [Å]	2.98- 3.27	2.98- 3.27	3.02- 3.30	3.05- 3.39
Observation angle (ion beam direction), [deg]	90	90	80	99
Detection				
X-ray film	Kodak DEF	Kodak DEF	Kodak DEF	Kodak RAR

Table 4.2: *Experiments on the interaction of calcium ions with solid targets.*

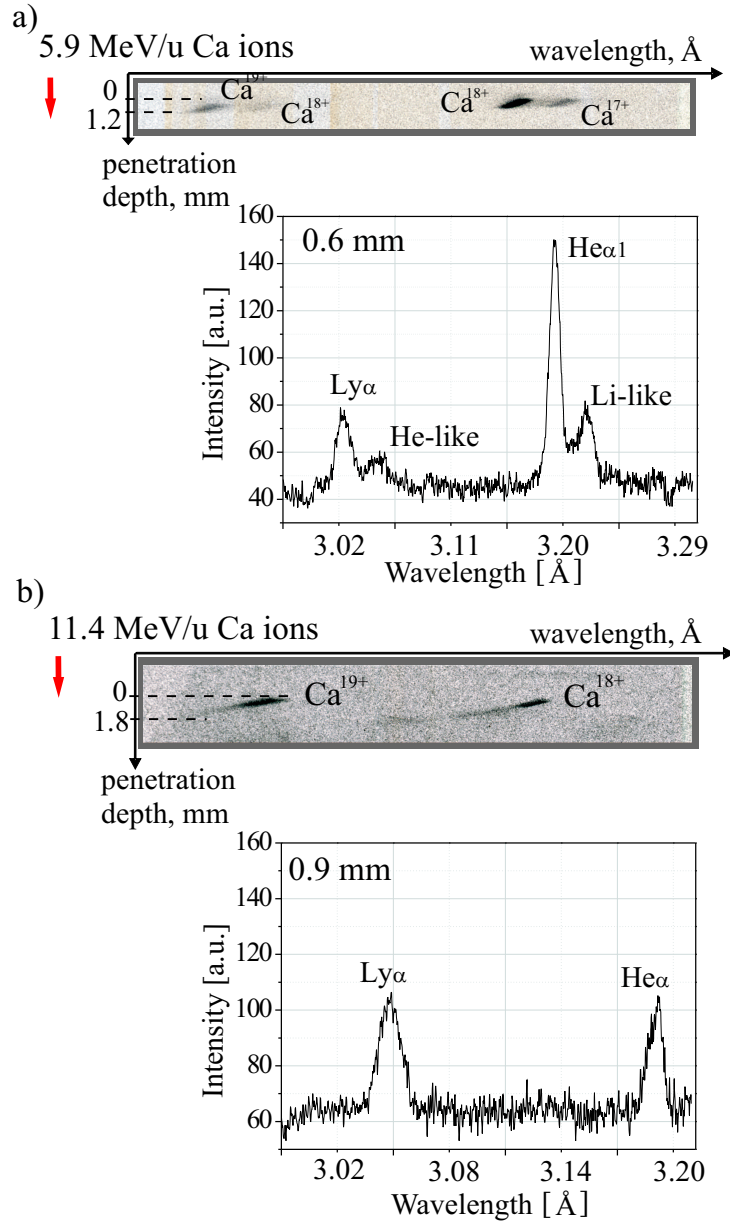


Figure 4.7: *K*-shell spectra of 5.9 MeV/u and 11.4 MeV/u Ca ions slowing down in 0.15 g/cm^3 SiO_2 aerogel. Densitograms correspond to the middle of the ion stopping path.

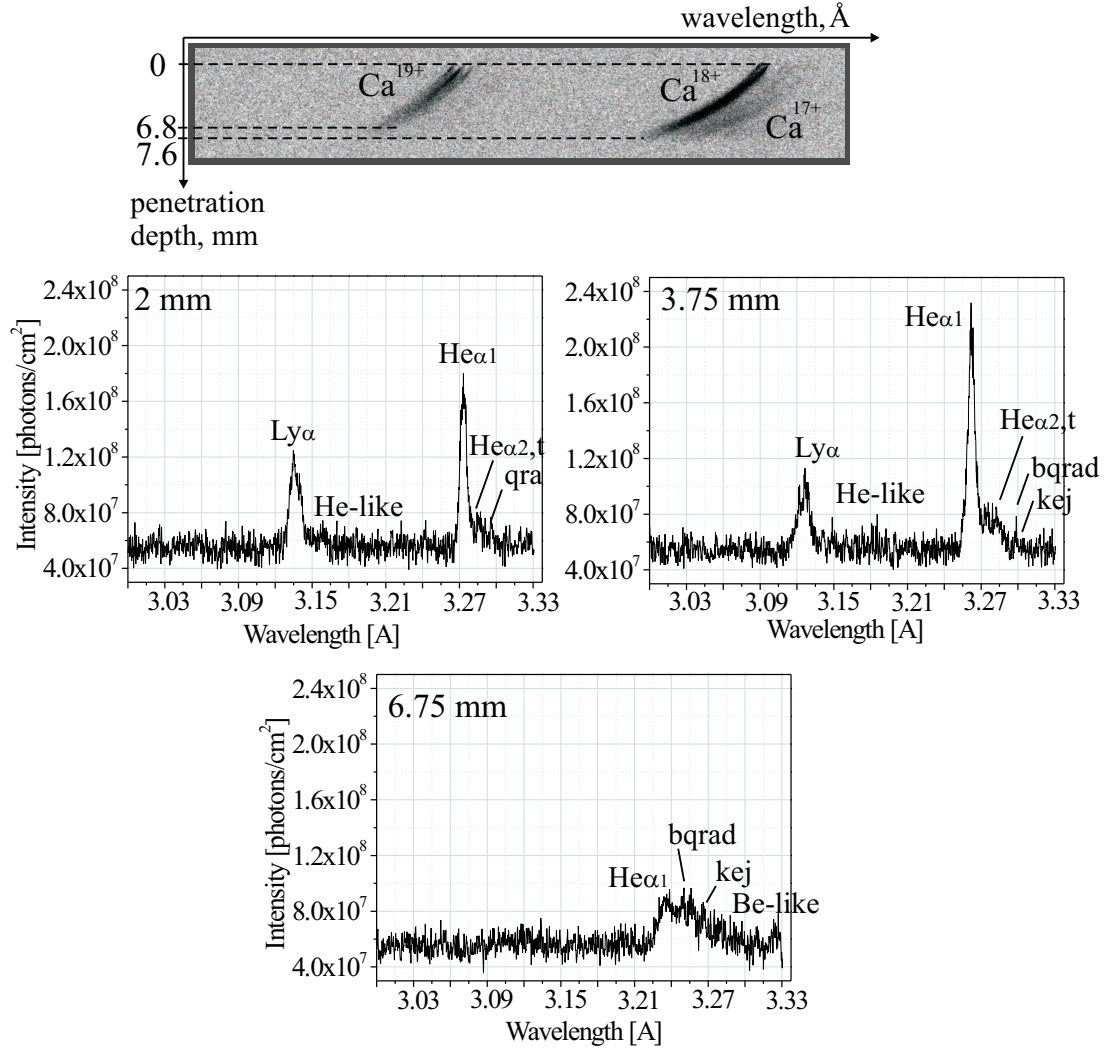


Figure 4.8: *K-shell spectra of Ca ions with the initial energy of 11.4 MeV/u slowing down in 0.04 g/cm³ SiO₂ aerogel. Densitograms demonstrate the formation of K_{α} satellites along the ion stopping path.*

In figure 4.7 the obtained spectra are presented for both cases. The radiation of 5.9 MeV/u calcium projectiles contains the transition, which corresponds Ly_{α} line $2p \ ^2P_{1/2,3/2} - 1s \ ^2S_{1/2}$ (the electronic system with one bound electron) and its satellites $2l2l - 1s2l$, the resonance $\text{He}_{\alpha 1}$ line $1s2p \ ^1P_1 - 1s^2 \ ^1S_0$ (two bound electrons) as well as the satellite group $1s2l2l' - 1s^22l$ (three bound electrons). The maximum of the line intensity is at the $\text{He}_{\alpha 1}$ in Ca^{18+} . At the ion energy of 11.4 MeV/u line intensities of highly ionized ions (Ly_{α} in Ca^{19+} and $\text{He}_{\alpha 1}$ in Ca^{18+}) are observed and Ca^{17+} ions are not presented. This demonstrates the increase of

the mean ion charge at higher projectile energy. The increase of the ion energy provides a larger stopping range for the beam inside the target. The projectile K-shell radiation was recorded at 1.2 mm and 1.8 mm along the ion stopping path for ions with an energy of 5.9 MeV/u and 11.4 MeV/u, correspondingly.

In the next experiment projectile K-shell radiation has been recorded for 11.4 MeV/u Ca ions interacting with 0.04 g/cm³ SiO₂ aerogel. X-ray spectrum was observed by means of a focusing spectrometer with a spherically bent mica crystal of R=150 mm and recorded by Kodak DEF X-ray film. The spectrometer was set in the direction of the ion beam propagation at 80° to the ion beam axis. The spectral resolution achieved in the experiment was $\lambda/\Delta\lambda=2000-5000$, the spatial resolution was 30-70 μm . X-ray film was scanned with optical resolution of 2820 dpi.

The intense long-lasting radiation of Ly $_{\alpha}$ (Ca¹⁹⁺) and He $_{\alpha 1}$ (Ca¹⁸⁺) lines has been registered of 6.8 mm and 7.6 mm, correspondingly (figure 4.8). This represents 75-87 % of the full stopping range. The formation of charge states of heavy ions was observed in dependence on the ion penetration depth in the target material. Table 4.3 shows the measured ion charge states of the presented experiment. The wavelengths of the radiative transitions of the ion in the rest are given in this table.

At the beginning of the ion stopping path (2 mm) high ion charge states (Ly $_{\alpha}$ and He $_{\alpha 1}$ lines) are the most intense and the blending of their satellites as well as the intercombination line He $_{\alpha 2}$ (forbidden transition) are not well pronounced. By penetrating into the target (3.75 mm) at lower ion energy the intensity of Ly $_{\alpha}$ is decreased. K $_{\alpha}$ -satellites are supplemented with series of new He- and Li-like satellites. Finally, close to the end of the ion penetration length (6.75 mm) the high ion charge states (Ly $_{\alpha}$ with its satellites) disappear, but the low ion charge states (Li-like satellites) become relatively intense and a group of K $_{\alpha}$ -satellites corresponding to the radiative transitions in the Be-like (four bound electrons) electronic system of calcium projectiles starts to appear. It was difficult to resolve the Be-like satellites of calcium ions because of the low intensity of the corresponding radiative transitions at the given energies. Therefore, only the envelope of the satellites group was observed and compared with theoretical data calculated by U.I.Safronova and T.G.Lisina [Safronova and Lisina, 1979].

The projectile radiation dynamics along the stopping path shows predominance of the high charge states at high ion energy and appearance of the low charge states at low ion energy. The low ion charge states appear and become relatively intense close to the end of the stopping length due to the capture process of bound target electrons by projectiles at low ion energies. The experimental error is 0.00016-0.00187 Å.

Ion charge state	$\lambda, \text{\AA}$	Transition	Line	Probability of radiative decay (s^{-1})
H-like	3.0185	$2p\ ^2P_{1/2} - 1s\ ^2S_{1/2}$	$\text{Ly}_{\alpha 2}$	1.02×10^{14}
	3.0238	$2p\ ^2P_{1/3} - 1s\ ^2S_{1/2}$	$\text{Ly}_{\alpha 1}$	1.02×10^{14}
	3.03563	$2s2p\ ^1P_1 - 1s2s\ ^1S_0$		9.87×10^{13}
	3.04534	$2p2p\ ^3P_2 - 1s2p\ ^3P_2$		1.30×10^{14}
He-like	3.1773	$1s2p\ ^1P_1 - 1s^2\ ^1S_0$	$\text{He}_{\alpha 1}$	1.68×10^{14}
	3.18993	$1s2p\ ^3P_1 - 1s^2\ ^1S_0$	$\text{He}_{\alpha 2}$	6.74×10^{13}
Li-like	3.19173	$1s2p(^1P)2s\ ^2P_{1/2} - 1s^22s\ ^2S_{1/2}$	t-satellite	3.52×10^{13}
	3.1988	$1s2p(^3P)2p\ ^2P_{3/2} - 1s^22p\ ^2P_{1/2}$	b-satellite	1.09×10^{13}
	3.20094	$1s2p(^3P)2s\ ^2P_{3/2} - 1s^22s\ ^2S_{1/2}$	q-satellite	1.60×10^{14}
	3.20277	$1s2p(^3P)2s\ ^2P_{1/2} - 1s^22s\ ^2S_{1/2}$	r-satellite	1.30×10^{14}
	3.2036	$1s2p(^3P)2p\ ^2P_{3/2} - 1s^22p\ ^2P_{3/2}$	a-satellite	2.18×10^{14}
	3.20709	$1s2p(^1D)2p\ ^2D_{3/2} - 1s^22p\ ^2P_{1/2}$	k-satellite	9.97×10^{13}
		$1s2p(^3P)2p\ ^2P_{1/2} - 1s^22p\ ^2P_{3/2}$	e-satellite	6.61×10^{13}
	3.2101	$1s2p(^1D)2p\ ^2D_{5/2} - 1s^22p\ ^2P_{3/2}$	j-satellite	8.03×10^{13}
Be-like	3.2176	$1s2s2p^2\ ^3S_1 - 1s^22s2p\ ^3P_2$		2.28×10^{13}
	3.2190	$1s2p^3\ ^1P_1 - 1s^22p^2\ ^1D_2$		1.24×10^{14}
	3.2205	$1s2s2p^2\ ^1S_0 - 1s^22s2p\ ^1P_1$		7.73×10^{13}
	3.2209	$1s2s^22p\ ^1P_1 - 1s^22s^2\ ^1S_0$		1.28×10^{13}
	3.2220	$1s2p^3\ ^3P_0 - 1s^22p^2\ ^3P_1$		7.48×10^{13}

Table 4.3: Radiative transitions of Ca ions for the experiment on the interaction of 11.4 MeV/u Ca ions with 0.04 g/cm^3 SiO_2 aerogel.

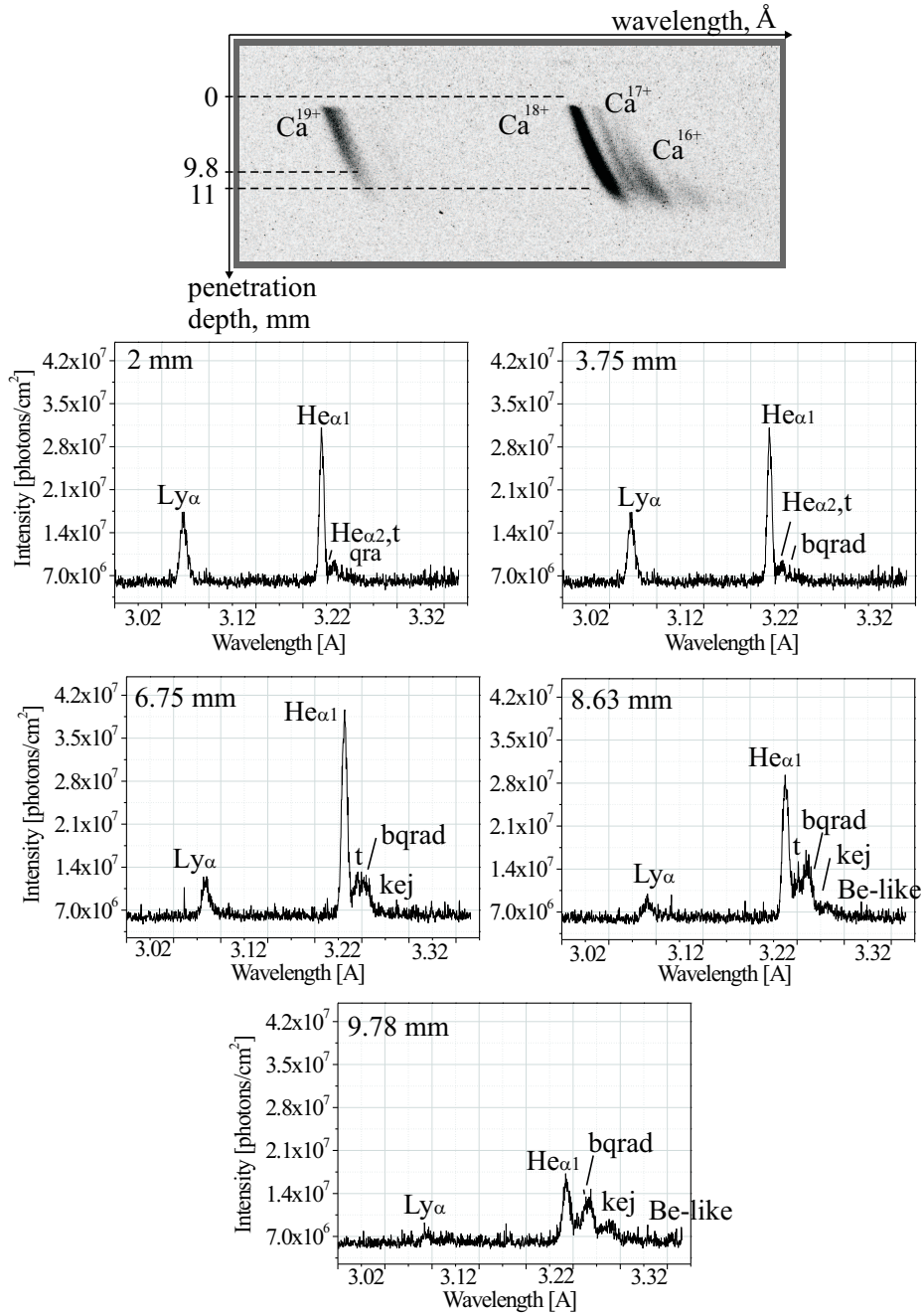


Figure 4.9: K_α spectra of 10.65 MeV/u Ca ions interacting with 0.023 g/cm³ SiO₂ aerogel. The formation of K_α satellites is shown with densitograms along the ion penetration path.

In order to observe lower ion charge states the experiment on the interaction

Ion charge state	$\lambda, \text{\AA}$	Transition	Line	Probability of radiative decay (s^{-1})
H-like	3.0185	$2p\ ^2P_{1/2} - 1s\ ^2S_{1/2}$	$\text{Ly}_{\alpha 2}$	1.02×10^{14}
	3.0238	$2p\ ^2P_{1/3} - 1s\ ^2S_{1/2}$	$\text{Ly}_{\alpha 1}$	1.02×10^{14}
He-like	3.1773	$1s2p\ ^1P_1 - 1s^2\ ^1S_0$	$\text{He}_{\alpha 1}$	1.68×10^{14}
	3.18951	$1s2p\ ^3P_1 - 1s^2\ ^1S_0$	$\text{He}_{\alpha 2}$	6.74×10^{13}
Li-like	3.19145	$1s2p(^1P)2s\ ^2P_{1/2} - 1s^22s\ ^2S_{1/2}$	t-satellite	3.52×10^{13}
	3.19924	$1s2p(^3P)2p\ ^2P_{3/2} - 1s^22p\ ^2P_{1/2}$	b-satellite	1.09×10^{13}
	3.20047	$1s2p(^3P)2s\ ^2P_{3/2} - 1s^22s\ ^2S_{1/2}$	q-satellite	1.60×10^{14}
	3.20219	$1s2p(^3P)2s\ ^2P_{1/2} - 1s^22s\ ^2S_{1/2}$	r-satellite	1.30×10^{14}
	3.20342	$1s2p(^3P)2p\ ^2P_{3/2} - 1s^22p\ ^2P_{3/2}$	a-satellite	2.18×10^{14}
	3.20737	$1s2p(^1D)2p\ ^2D_{3/2} - 1s^22p\ ^2P_{1/2}$	k-satellite	9.97×10^{13}
	3.20861	$1s2p(^3P)2p\ ^2P_{1/2} - 1s^22p\ ^2P_{3/2}$	e-satellite	6.61×10^{13}
	3.21359	$1s2p(^1D)2p\ ^2D_{5/2} - 1s^22p\ ^2P_{3/2}$	j-satellite	8.03×10^{13}
Be-like	3.2176	$1s2s2p^2\ ^3S_1 - 1s^22s2p\ ^3P_2$		2.28×10^{13}
	3.2190	$1s2p^3\ ^1P_1 - 1s^22p^2\ ^1D_2$		1.24×10^{14}
	3.2205	$1s2s2p^2\ ^1S_0 - 1s^22s2p\ ^1P_1$		7.73×10^{13}
	3.2209	$1s2s^22p\ ^1P_1 - 1s^22s^2\ ^1S_0$		1.28×10^{13}
	3.2220	$1s2p^3\ ^3P_0 - 1s^22p^2\ ^3P_1$		7.48×10^{13}
	3.2222	$1s2p^3\ ^3P_2 - 1s^22p^2\ ^3P_2$		1.46×10^{13}
	3.2238	$1s2p^3\ ^3P_1 - 1s^22p^2\ ^3P_2$		6.92×10^{13}
	3.2238	$1s2s2p^2\ ^1P_1 - 1s^22s2p\ ^1P_1$		2.32×10^{14}
	3.2243	$2p^22s(^4P)1s\ ^3P_2\ 1s^22s2p\ ^3P_1$		1.85×10^{13}

Table 4.4: Radiative transitions of Ca ions for the experiment on the interaction of 10.65 MeV/u Ca ions with 0.023 g/cm³ SiO₂ aerogel.

of 11.4 MeV/u Ca projectiles with 0.023 g/cm³ silica aerogel has been performed. In front of the aerogel a 5 μ m Havar foil was placed and decelerated the ion beam from the initial energy down to 10.65 MeV/u. The X-ray projectile radiation was observed using a focusing spectrometer with a spherically bent mica crystal installed in the direction of ion beam propagation at 99° to the ion beam axis. The spectrum was recorded with Kodak RAR X-ray film and then scanned with optical resolution of 1600 dpi.

The projectile ion characteristic spectrum was measured with a high spectral ($\lambda/\Delta\lambda = 1000 - 3000$) and spatial resolution (30-130 μ m) along the ion beam stopping path.

A 0.023 g/cm³ silica aerogel was used in order to achieve a larger stopping path and, therefore, to improve the spatial resolution of the radiation dynamics. Figure 4.9 shows the K-shell spectra of ions for different ion penetration depths of the presented experiment. In this case the observed stopping length was 9.8 mm and 11 mm for Ly $_{\alpha}$ and He $_{\alpha 1}$ lines, correspondingly.

The radiative transitions of Ca projectile ions recorded in the performed experiment are summarized in table 4.4. They are in good agreement with data of the previous experiment (0.04 g/cm³ SiO₂ aerogel). However, the Be-like satellite group is more pronounced close to the end of the stopping path.

The estimated value of an error for this experiment is 0.00024-0.00369 Å.

4.1.5 Analysis of the projectile charge state dynamics

The ion radiation dynamics along the stopping path in experiments on the interaction of calcium ions with 0.04 g/cm³ and 0.023 g/cm³ silica aerogels shows the increase of the K $_{\alpha}$ -satellite intensity corresponding to the radiation of Ca¹⁷⁺ and Ca¹⁶⁺ ions due to the capture of target bound electrons by projectile ions at lower energy.

The spectroscopic analysis of the projectile radiation was complemented by measurements of the charge state distribution of ions having left the target. Figure 4.10 shows the charge state distribution of 11.4 MeV/u Ca ions interacting with a 8.39-mm-thick piece of 0.023 g/cm³ silica aerogel with a linear density of 19 mg/cm² analyzed inside the target by the method of X-ray spectroscopy of K-shell radiation (figure 4.10a) and after the target by means of a magnetic spectrometer (figure 4.10b). The K-shell spectrum of excited states was observed with a spatial resolution by means of a focusing crystal spectrometer in the direction of the ion beam propagation at 90° to the ion beam axis. In the second case the charge of Ca ions was analyzed using a magnetic spectrometer with a magnetic field of 1.63 T for the ion beam emerging from the target. The measured ion beam energy after the target was 6.54 MeV/u.

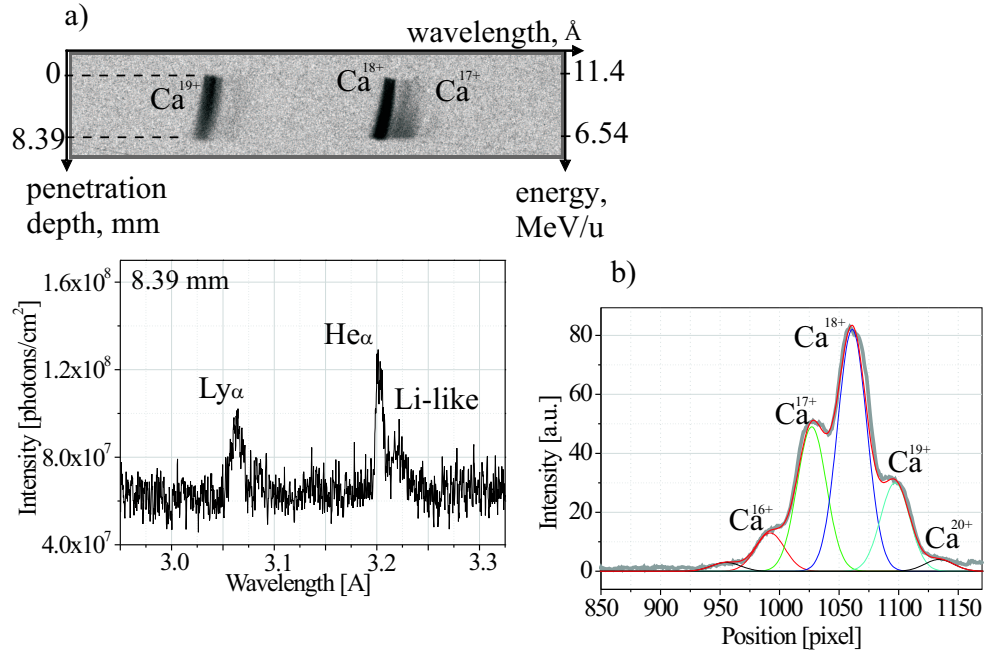


Figure 4.10: Experiments on the interaction of 11.4 MeV/u Ca ions with a 8.39-mm-thick piece of 0.023 g/cm^3 SiO_2 aerogel. a) The K_α projectile spectrum observed inside the stopping medium using the method of X-ray spectroscopy of K-shell radiation. The densitogram corresponds to the end of the penetration depth. b) The charge state distribution of Ca ions measured after the target. Data were obtained and analyzed by means of a magnetic spectrometer.

As is well known, the K_α -satellite intensity is proportional to the population of the projectile excited state $1s2pml^k$, which gives rise to these radiative transitions. For Ca^{19+} it is a $2p$ state, for Ca^{18+} a $1s2p$ (1P_1) state. The $2p$ state can be populated by three different mechanisms: due to the bound electron capture of a target electron by Ca^{20+} , due to the excitation of a projectile bound electron from the ground state in Ca^{19+} ($1s-2p$) and by ionization of a $1s$ electron from the excited state $1s2p$ of Ca^{18+} . The role of each mechanism depends on the ion energy and charge state distribution. The same is valid for the $1s2p$ state of Ca^{18+} . Therefore, there are at least three projectile charge states involved in the analysis of Ly_α (Ca^{19+}) and He_α (Ca^{18+}) radiative transitions. K_α transitions in Ca^{17+} and lower charges arise from autoionization states $1s2s^m2p^k$ ($m = 0, 1, 2$; $k = 0, 1, \dots, 6$ depending on the ion charge and the electronic configuration). These electronic states are produced due to the K-shell ionization of the projectile ground and excited states $1s2s^m2p^k$. These configurations can decay not only via radiation, but

as well due to the Auger effect. Therefore, their line intensities depend on the fluorescence factor $\Gamma_r/(\sum \Gamma_r + \Gamma_A)$, where Γ_r is the radiative decay probability, Γ_A is the Auger decay probability. According to the calculated values of fluorescence factors, the radiative transitions from excited electronic configurations with $m = 0, 1$ give the main contribution to the K-shell spectrum. Autoionization levels produced due to the K-shell ionization of the projectile ground states with $1s2s^22p^k$ ($m = 2$) have mostly low radiative transition probability.

In the case of the magnet spectroscopy the following fractions of calcium charge states after the target were measured: 2.8 % for Ca^{20+} ; 16.7 % for Ca^{19+} ; 44.7 % for Ca^{18+} ; 28 % for Ca^{17+} ; 6.7 % for Ca^{16+} ; 1.1 % for Ca^{15+} .

Certainly, the spectrum observed inside the target (excited states of projectile ions)(figure 4.10a) and after the target (ions in the ground state)(figure 4.10b) can not be compared directly. However, it is possible to reconstruct the dynamics of the projectile ions for the measurement after the target: to simulate the line intensities of projectiles before a complete relaxation takes place. In this case one can simulate what would be the population of excited levels of the ions measured after the magnet without having undergone the full relaxation process. The theoretical calculations were performed and are in good agreement with the measurement (see next chapter).

The quantitative analysis of the ion charge state distribution inside the stopping medium using K-shell satellite intensities demands detailed calculations of the projectile excited and ground state population kinetics caused by collisional and noncollisional processes. The advantage provided by this experimental method is the following: in order to calculate the rates of collisional processes, the measured dependence of the projectile velocity on the ion penetration depth can be used. It allows to reconstruct the dynamics of the projectile bound electron structure and the ion charge states along the projectile stopping path.

4.2 Experimental results with gaseous targets

During the study of the interaction of fast heavy ions with matter series of experiments with gaseous targets have been performed. 1.75 bar argon gas and 1.9 bar neon gas were used as stopping media. Ca ion beams with an initial energy of 11.4 MeV/u and 5.9 MeV/u were decelerated down to 10.65 MeV/u and 5 MeV/u, respectively, using a 5 μm Havar foil to separate the vacuum in the chamber from the gas pressure region. The K-shell projectile radiation was observed with a spatial resolution by means of a focusing crystal spectrometer. Time resolved diagnostics of gas density in the ion interaction zone was performed using the VarJet code.

4.2.1 Projectile radiation

In the following experiments on the interaction of 10.65 MeV/u and 5 MeV/u calcium ions with 1.9 bar neon gas the K-shell projectile radiation has been investigated.

The X-ray spectra were observed by means of a focusing spectrometer with a spherically bent mica crystal of $R=150$ mm. The spectrometer was installed at 90.4° to the ion beam axis in the direction of the ion beam propagation. The K-shell radiation was recorded by Kodak DEF X-ray film and scanned with optical resolution of 1600 dpi. The spectral resolution achieved in the experiment was $\lambda/\Delta\lambda=1000-3000$, the spatial resolution was up to $130\text{ }\mu\text{m}$.

The K-shell spectra of energetic ions were recorded through the first X-ray transmission window, which has a length of 40 mm and is oriented along the ion beam propagation. The distance from the Havar foil to the beginning of this window was 20 mm. Therefore, the radiation from the first 20 mm of the penetration length in the gaseous target was not observed.

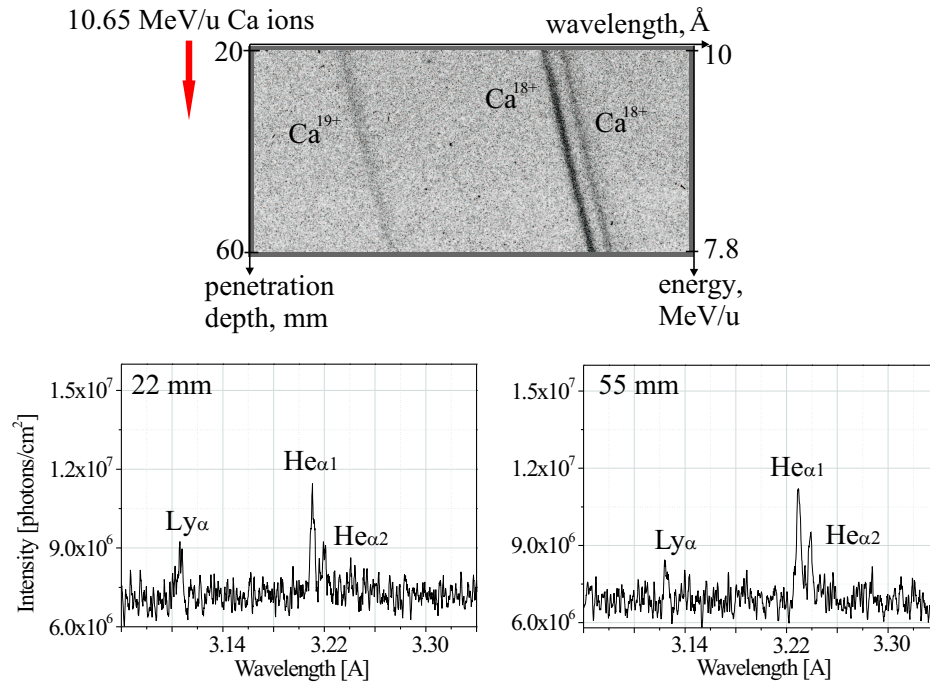


Figure 4.11: *K-shell spectra of Ca ions with the initial energy of 11.4 MeV/u interacting with 1.9 bar Ne gas. The ion beam was decelerated down to 10.65 MeV/u by a $5\text{ }\mu\text{m}$ Havar foil. The projectile radiation was recorded through the first X-ray transmission window.*

Ion charge state	$\lambda, \text{\AA}$	Transition	Line	Probability of radiative decay (s^{-1})
He-like	3.1773	$1s2p\ ^1P_1 - 1s^2\ ^1S_0$	$\text{He}_{\alpha 1}$	1.68×10^{14}
	3.18927	$1s2p\ ^3P_1 - 1s^2\ ^1S_0$	$\text{He}_{\alpha 2}$	6.74×10^{13}
Li-like	3.19266	$1s2p(^1P)2s\ ^2P_{1/2} - 1s^22s\ ^2S_{1/2}$	t-satellite	3.52×10^{13}
	3.19655	$1s2p(^3P)2p\ ^2P_{3/2} - 1s^22p\ ^2P_{1/2}$	b-satellite	1.09×10^{13}
	3.20047	$1s2p(^3P)2s\ ^2P_{3/2} - 1s^22s\ ^2S_{1/2}$	q-satellite	1.60×10^{14}
	3.20243	$1s2p(^3P)2s\ ^2P_{1/2} - 1s^22s\ ^2S_{1/2}$	r-satellite	1.30×10^{14}
Be-like	3.21484	$1s2s2p^2\ ^3S_1 - 1s^22s2p\ ^3P_1$		3.21×10^{13}
	3.21936	$1s2p^3\ ^1P_1 - 1s^22p^2\ ^1D_2$		1.24×10^{14}
	3.22213	$1s2p^3\ ^3P_0 - 1s^22p^2\ ^3P_1$		7.48×10^{13}
	3.22415	$2p^22s(^4P)1s\ ^3P_2\ 1s^22s2p\ ^3P_1$		1.85×10^{13}
	3.23873	$1s2p^3\ ^3S_1 - 1s^22p^2\ ^1D_2$		3.67×10^{12}
	3.24079	$1s2s2p^2\ ^3S_1 - 1s^22s2p\ ^1P_1$		2.07×10^{12}

Table 4.5: Radiative transitions measured in the experiment on the interaction of 5 MeV/u Ca ion beam with 1.9 bar Ne gas.

The projectile radiation of 10.65 MeV/u calcium ions interacting with the gaseous target is presented in figure 4.11.

The projectile K-shell radiation of Ca^{19+} (Ly_{α}) and Ca^{18+} ($\text{He}_{\alpha 1}$ -allowed and $\text{He}_{\alpha 2}$ -forbidden transitions) in the 10 - 7.8 MeV/u energy region was recorded. The significant change of the line intensities was not observed along the penetration depth.

Figure 4.12 shows the K_{α} spectra of 5 MeV/u Ca projectiles at energies of 4.37 - 3 MeV/u.

In the performed experiment it was possible to resolve the projectile radiation in the low energy region. The observed stopping path was 40 mm. The charge states are summarized in table 4.5.

In this case the radiation of Ca^{19+} (Ly_{α}) ions is fully absent and Ca^{18+} (resonance $\text{He}_{\alpha 1}$ and intercombination $\text{He}_{\alpha 2}$) ions start to disappear at the stopping length of 35 mm. The maximum of the spectral line intensity is shifted to the group of satellites originating from the autoionizing states of Ca^{17+} and Ca^{16+} . The group of Li-like *tbqr* satellites is intensive along the observed ion stopping length and close to the end of the path *bq* satellites starts to be well pronounced. K_{α} satellites corresponding to the radiative transitions in the Be-like electronic system of calcium ions was resolved and is in close agreement with calculations

of U.I.Safronova and T.G.Lisina [Safronova and Lisina, 1979]. It is important to note that at the end of the stopping path Ca^{16+} projectile radiation exhibits two new satellites, which were not observed in experiments with silica aerogels. As indicated above the shift to the lower charge states is due to the increase of the bound electron capture cross sections at lower projectile energy. The measurement error of the experiment is $0.00024 - 0.00285 \text{ \AA}$.

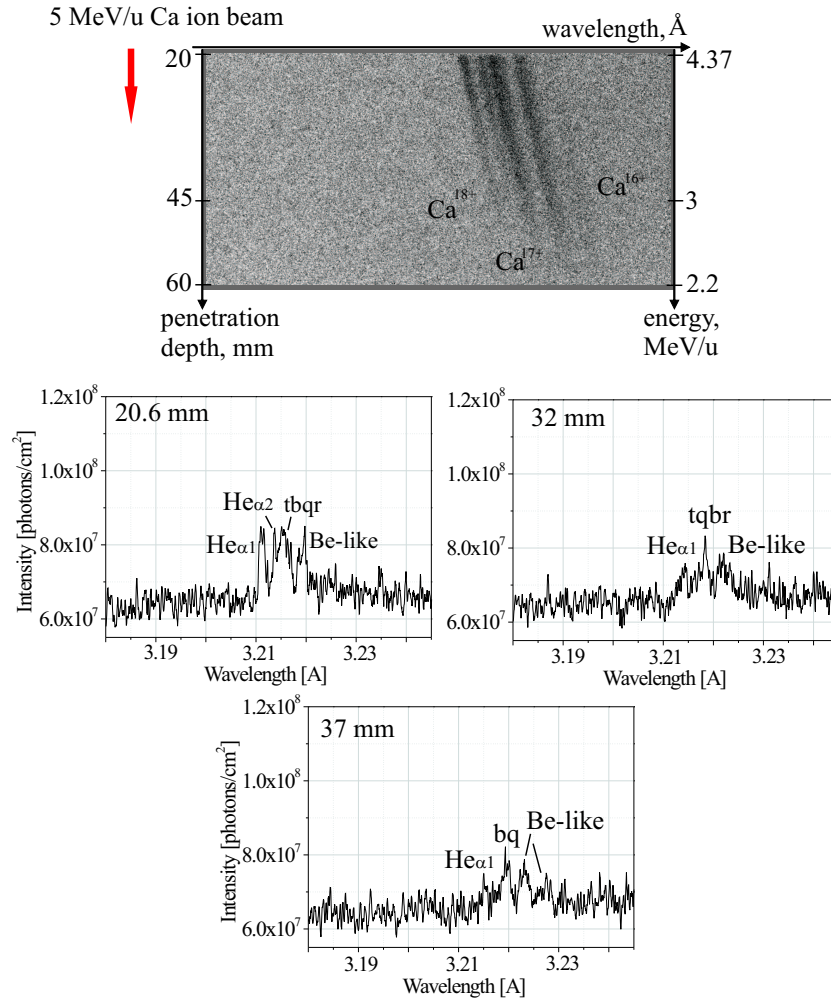


Figure 4.12: K_α spectra produced due to slowing down of Ca ions with the initial energy of 5.9 MeV/u in 1.9 bar Ne gas. The ion beam energy in gas after passing the stripping foil was 5 MeV/u. The characteristic ion radiation was collected from the first X-ray transmission window.

4.2.2 Diagnostics of the gas density

In the experiment on the interaction of 5 MeV/u Ca ions with 1.75 bar argon gas the influence of the target density on the ion stopping process has been investigated.

The energy of heavy ions and the pressure of the gas were chosen to stop the ion beam in the target completely. The 2D visible image of the ion beam-gas target interaction region was recorded through a 180 mm long quartz window using an intensified gated CCD camera (Dicam Pro). The observed image is the fluorescence emission of gas atoms induced due to collisional excitation by the ion beam and secondary electrons. The ion beam deposits its energy to excite and ionize atoms of the stopping medium. It leads to heating and expansion of the gas in the interaction region. The gas density varies along the ion beam stopping path with time and the beam radius.

In the performed experiment the lengthening of the ion beam range in argon gas during the ion macro pulse of 5 ms was observed over 65 mm. These ion beam range measurements with a time step of 100 μ s are presented in figure 4.13. The measured values are normalized to the range length during the first 100 μ s of the macro pulse duration.

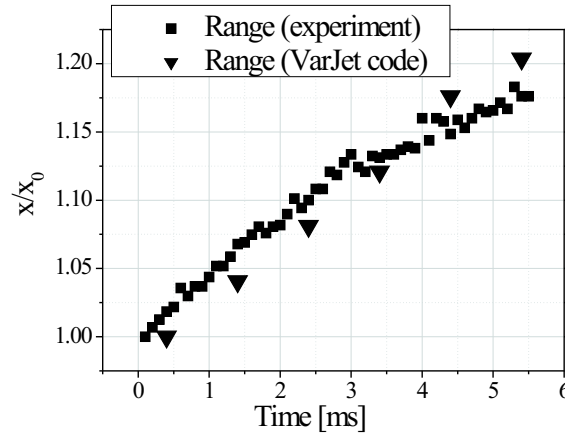


Figure 4.13: Relative range lengthening of Ca ion beam with energy of 5 MeV/u in gas during the macro pulse of 5 ms. Measured range (squares) is compared with VarJet numerical simulations (triangles).

The numerical calculations of the stopping range using the SRIM code, 49.79 mm, was not in agreement with the experimental result. In order to understand the observed range lengthening phenomena numerical simulations on hydrody-

dynamic response of the beam-heated gas have been carried out. The VarJet code has been employed in the simulations [Varentsov, 2006]. The numerical calculations are in close agreement with experimental results and shown in the same figure (figure 4.13).

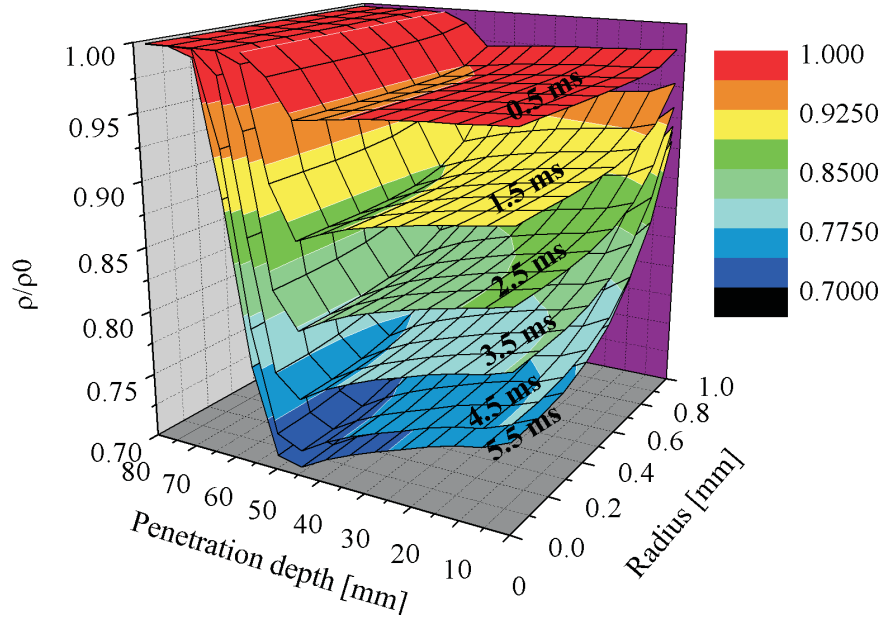


Figure 4.14: Density distribution of Ar gas in the experiment on the interaction with 5 MeV/u Ca ion beam calculated using the VarJet code. The calculations were performed during the macro pulse of 5.5 ms, along the ion beam path (X axis) and across the ion beam radius (Y axis). The density is normalized to the initial value.

In the presented simulations the following input ion beam data related to the experimental conditions were used: 5 MeV/u of calcium ions after deceleration in the Havar entrance foil, 1 mm ion beam radius, homogeneous ion distribution across radius, $8.6 \cdot 10^8$ particles in the macro pulse, 5.5 ms pulse duration. The value of deposited energy reached $2-3 \text{ J/g} \cdot \text{cm}^2$. It leads to an increase of the gas temperature in the interaction zone by $100^\circ-120^\circ$.

The calculated distribution of argon gas density along the ion beam path in the target and across the ion beam radius is plotted in figure 4.14 for different time during the macro pulse. According to simulations the target density is changing during the long pulse duration across the ion beam radius and along the ion beam trajectory. The minimum target density (about 70 % from the initial value) was reached after 5.5 ms in the region of maximum ion energy deposition.

4.3 Experimental evidence of the gas-solid effect

In the presented work a whole series of experiments on the interaction of fast heavy ions with solid and gaseous targets was carried out. These investigations provided a lot of information about the ion stopping process, projectile velocity dynamics, the charge state distribution of heavy ions in collisions with target atoms as well as atomic collisional characteristics, such as ionization and electron-capture cross sections. The charge changing processes, which play important role in the level population of ions, strongly depend on the density of the stopping medium.

The influence of the target density on the formation of charge states of heavy ions has been studied. Spatially resolved K-shell spectra of calcium ions were compared in solid and gaseous targets at the same experimental conditions (ion energy). The detailed descriptions of the experiments are presented in this chapter.

Figure 4.15 shows spectra of 11.4 MeV/u Ca ions slowed down in 0.04 g/cm³ silica aerogel and 1.9 bar neon gas and their densitograms at the energy of 9.2 MeV/u. This energy corresponds to a penetration depth of 2.5 mm in the aerogel and 35 mm in the gaseous target. In both cases the radiation of Ca¹⁹⁺ (Ly_α) and Ca¹⁸⁺ (He_{α1} and He_{α2}) is well pronounced. K_α satellites corresponding to the radiative transitions in Li-like electronic system start to appear in aerogel. The ratio of line intensities in solid and gaseous targets is

$$\frac{I_S(He_{\alpha1})}{I_S(Ly_{\alpha})} = 1.4, \quad \frac{I_G(He_{\alpha1})}{I_G(Ly_{\alpha})} = 2.2. \quad (4.2)$$

The K_α spectra were compared also at lower energy, 4.2 MeV/u, in the experiments on the interaction of 11.4 MeV/u calcium ions with 0.04 g/cm³ SiO₂ aerogel and 5.9 MeV/u Ca ions with 1.9 bar neon gas (figure 4.16). The energy of 4.2 MeV/u corresponds to the penetration depth of 6.75 mm in silica aerogel and 23 mm in the gaseous target. At this low energy the radiation of Ca¹⁹⁺ starts to disappear, Ca¹⁸⁺ is dominant and Ca¹⁷⁺ is well pronounced with a blending of Ca¹⁶⁺. In the case of the gaseous target the radiation of Ca¹⁹⁺ is completely vanished, Ca¹⁸⁺ radiative transition is still pronounced, but the spectra line intensity is shifted to Ca¹⁷⁺ and Ca¹⁶⁺. The ratio of He_{α1} and Ly_α line intensities in silica aerogel is following:

$$\frac{I_S(He_{\alpha1})}{I_S(Ly_{\alpha})} = 4.87. \quad (4.3)$$

As is well known, the intensity of spectral lines is proportional to the population of excited states [Sobelman et al., 1995]. In the experiments a difference in the population of excited states of Ca¹⁹⁺, Ca¹⁸⁺, Ca¹⁷⁺ and Ca¹⁶⁺ ions in solid and gaseous media has been observed. In solid target the higher population of

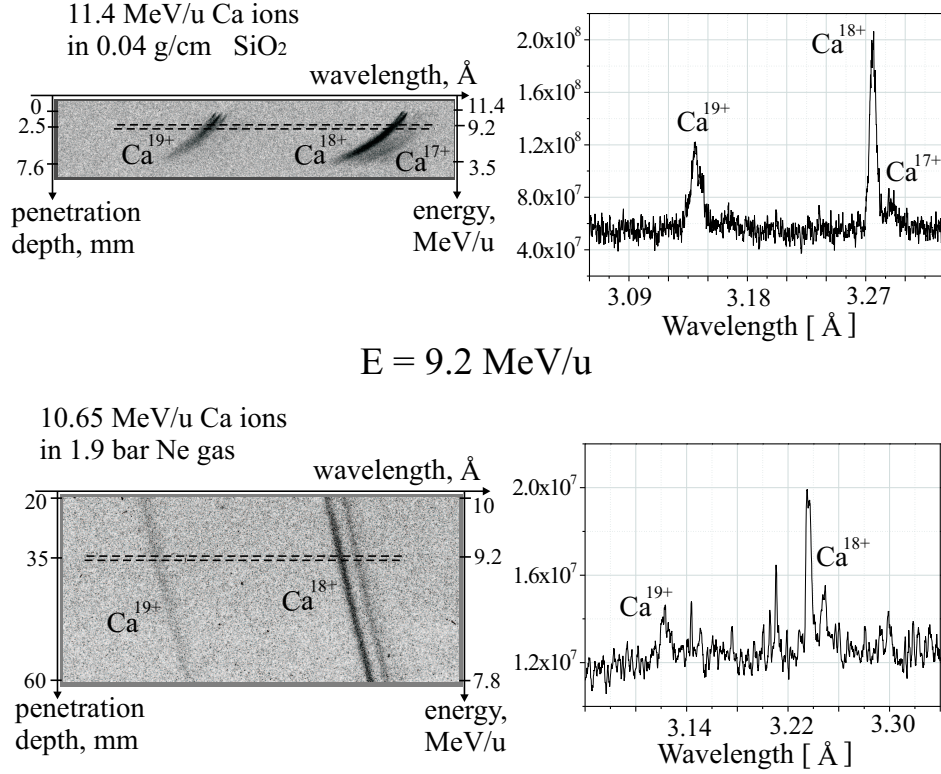


Figure 4.15: K_{α} spectra of 11.4 MeV/u Ca ions slowed down in 0.04 g/cm³ SiO₂ aerogel and 10.65 MeV/u Ca ions in 1.9 bar Ne gas. Densitograms correspond to the energy of 9.2 MeV/u (Y axis is the line intensity [photons/cm²], X axis is the wavelength [Å]).

excited states of highly charged ions is observed, but not in gaseous target. The reason of this is the influence of the target density. The rate coefficient of the collisional process is defined by the target density, $R_{coll} \sim N_T$. In solid target the increase of the population of projectile excited states leads to an increase of the effective ionization rate of the projectile ions due to collisions with target atoms. At low ion energy the mechanism of the bound electron capture to high n of the projectile ions is dominant, n is the principle quantum number. Captured electrons are immediately ionized before the radiative transition to the ion ground state can stabilized the capture process. As a result, an increase of the projectile ion charge state arises from the increase of the target density.

The physical effects observed in the experiments have been interpreted with numerical calculations of the projectile population kinetics, which are given in the next chapter.

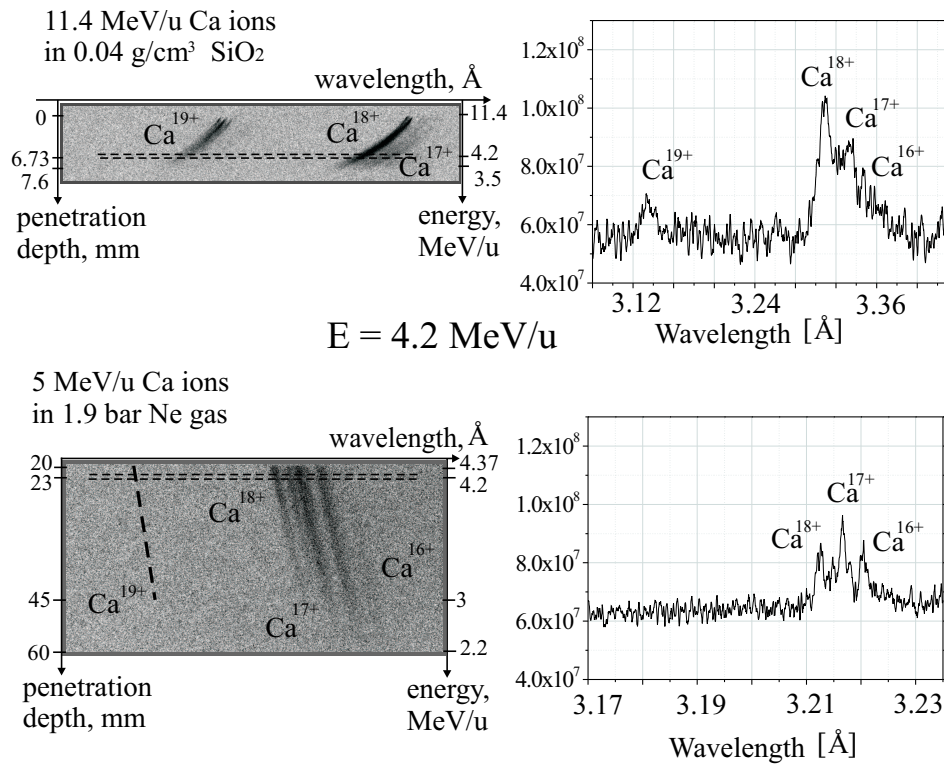


Figure 4.16: Projectile K_{α} spectra observed in the experiments on the interaction of 11.4 MeV/u calcium ions with 0.04 g/cm³ SiO₂ aerogel and 5 MeV/u Ca ions with 1.9 bar Ne gas. Densitograms correspond to the energy of 4.2 MeV/u (Y axis is the line intensity [photons/cm²], X axis is the wavelength [Å]).

Chapter 5

Numerical model of the ion population kinetics

In order to interpret the experimental results, a quantitative analysis of the ion population kinetics has been performed.

The intensity of a spectral line corresponding to the transition from the upper energy level k to the lower level i of an atom is given by [Sobelman et al., 1980]

$$I_{ki} = \hbar\omega_{ki}A_{ki}P(k) \quad [eVs^{-1}cm^{-3}], \quad (5.1)$$

where A_{ki} is the radiative probability for the transition $k \rightarrow i$, $P(k)$ is the population density of atoms excited to the level k , ω_{ki} is the frequency of the transition and \hbar is the Planck constant divided by 2π . If the populations of the atomic states are known, the intensity of the spectral lines can be predicted.

In the presented thesis populations of the ground and excited states of the projectile ions colliding with target atoms were calculated. The calculations have been performed for the case of the interaction of Ca ions with SiO₂ atoms (experimental conditions of the given work) in the context of the collisional-radiative model. The chosen model was limited to the Ca²⁰⁺, Ca¹⁹⁺, Ca¹⁸⁺, Ca¹⁷⁺, Ca¹⁶⁺ and Ca¹⁵⁺ ions. In every ion the ground and three excited states were taking into account. The numerical calculations were carried out for energy levels with the principle quantum number n without spin-orbital splitting. The scheme of the model is presented in figure 5.1.

The population and depopulation of the projectile ground and excited levels is determined by atomic elementary processes. In ion-atom interactions they are the following: projectile ionization, bound electron capture, collisional excitation and deexcitation as well as the Auger and radiative decay. The detailed description of them is presented in chapter 2. Autoionization states were not taken into considerations and, therefore, the Auger decay is neglected.

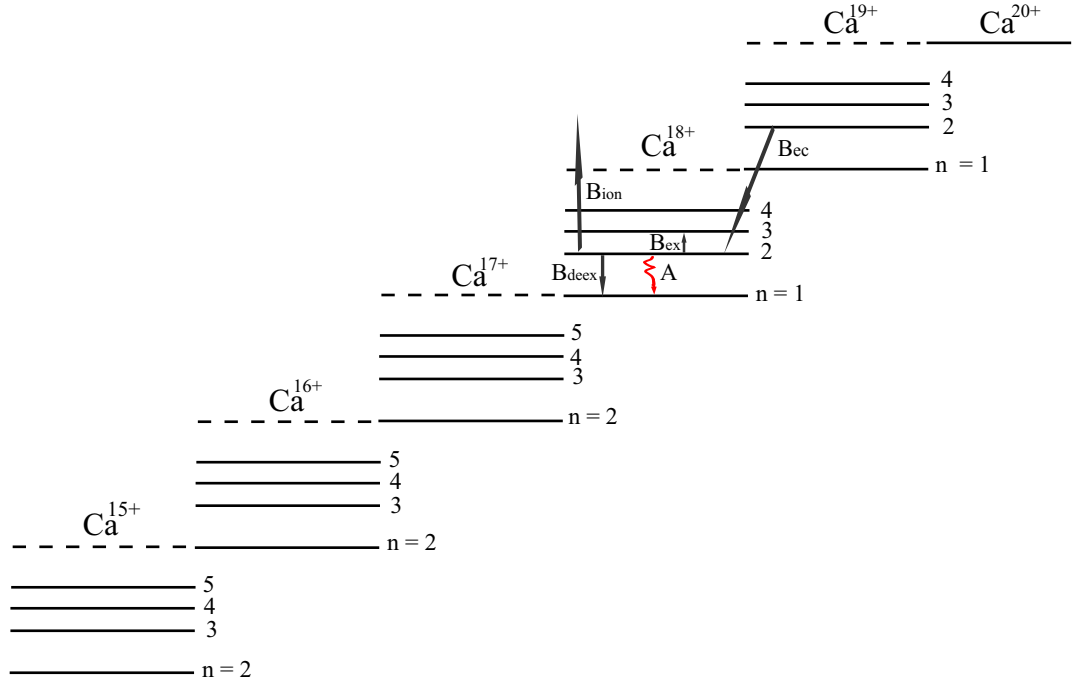


Figure 5.1: Energy level scheme of calcium ions used to calculate the population of the ground and excited states.

Numerical calculations of the projectile ionization and bound electron capture cross sections have been performed using the LOSS and CAPTURE codes, respectively. The computer code LOSS allows also estimating the excitation cross sections of the projectile. Cross sections of the deexcitation process were calculated as the inverse values of the excitation cross sections while taking into account the statistical weights of the energy levels. The radiative transition probabilities were estimated using the expression 2.27.

The population of the projectile states has been described by rate equations of the multilevel kinetics, which connect the ground and excited states of Ca^{19+} , Ca^{18+} , Ca^{17+} , Ca^{16+} , Ca^{15+} ions and bare nuclei.

The kinetic equation for the population P of the energy level k of the ion Z can be written as

$$\frac{dP_Z(k)}{dt} = \sum_{Z'} \sum_i B_{ik} P_{Z'}(i) - B_{kk} P_Z(k), \quad (5.2)$$

where B_{kk} is the sum of processes, which depopulate the energy level k ; B_{ik} is the sum of processes, which populate the level k as a result of a transition from the level i of the ion Z' , and $P_{Z'}(i)$ is the population of the level i of the ion Z' . B_{ik}

are the rate coefficients of elementary processes. For the collisional case the rate coefficient is determined by $R_{coll} = N_T v \sigma_{ion}$, for the non-collisional by radiative decay A (see chapter 2).

In equilibrium $P_Z(k)$ is defined:

$$P_Z(k) = \frac{\sum_{Z'} \sum_i B_{ik} P_{Z'}(i)}{B_{kk} P_Z(k)}. \quad (5.3)$$

In order to estimate the population of the energy levels, the system of equations in regard to $P_Z(k)$ should be resolved.

The system of equations was considered as a matrix equation

$$BP = 0. \quad (5.4)$$

B is the matrix of collisional and non-collisional rate coefficients, which connects the ground and excited states of ions and is written as

$$B = \begin{pmatrix} -b_{11} & b_{12} & \dots & b_{1m} \\ b_{21} & -b_{22} & \dots & b_{2m} \\ \dots & \dots & \dots & \dots \\ b_{m1} & b_{m2} & \dots & -b_{mm} \end{pmatrix}. \quad (5.5)$$

P is the column of populations of the presented states and equals:

$$P = \begin{pmatrix} P(1) \\ P(2) \\ \dots \\ P(m) \end{pmatrix}. \quad (5.6)$$

Since $-B_{kk} = \sum_{i \neq k} B_{ik}$ the matrix system is singular. Therefore, one of the equation was replaced by the conservation law of number particles:

$$\sum_{Z,k} P_Z(k) = 1. \quad (5.7)$$

The matrix equation was resolved by the Gauss method with serial eliminations that leads to a system with a triangular matrix. The calculations were performed using Mathematica.

The calculations of the energy level populations have been performed for three different densities: 10^{23} at/cm³ (solid quartz), 6×10^{20} at/cm³ (silica aerogel) and 10^{19} at/cm³ (gas). The results of these calculations are presented in figure 5.2.

As estimated for targets with 10^{23} at/cm³ density, nuclei and Ca¹⁹⁺ ions are dominant at high ion energy. This leads to an increase of the average charge. In the aerogel medium the increase of the population is shifted to Ca¹⁸⁺ ions and with the energy the decrease of the population of Ca¹⁷⁺ ions becomes significant.

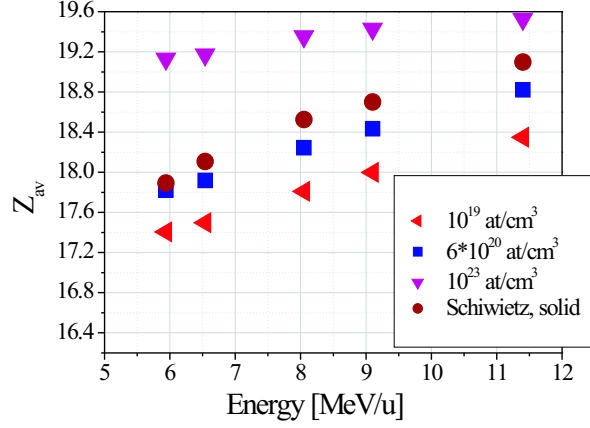


Figure 5.2: Average charge of calcium ions as function of the projectile energy calculated for solid quartz, silica aerogel and gaseous medium. It is compared with Schiwietz calculations for solid target [Schiwietz and Grande, 2001].

The population of low charged ions such as Ca^{17+} , Ca^{16+} and Ca^{15+} is dominant at the density of 10^{19} at/cm³, especially at low velocity.

The theoretical predictions were verified by comparison with the experimental results. First of all, the evidence of the gas-solid effect at high and low energy are interpreted with relation to the population density of energy levels.

The influence of the target density on the formation of ion charge states was investigated in experiments on the interaction of Ca ions with 0.04 g/cm³ SiO₂ aerogel and 1.9 bar Ne gas. The relative intensities of resonance lines of Ca^{19+} and Ca^{18+} ions (Ly_α and $\text{He}_{\alpha 1}$) were compared at the same ion energy. In calculations they were estimated as

$$I(res) = \frac{g(2p)}{g(2)} P(2) A_{2-1}. \quad (5.8)$$

$g(2p)$ is the statistical weight of the energy level from which the transition takes place, $2p^2 P_{1/2,3/2}$ for Ly_α ions and $1s2p^1 P_1$ for $\text{He}_{\alpha 1}$ ions. $g(2)$ is the statistical weight of the energy level with the principle quantum number 2 and $P(2)$ is the calculated population of this level. A_{2-1} is the radiative decay of the resonant transition. The result of the calculations as well as the average charge are presented in table 5.1 and compared with measurements. As one can see, the numerical estimations show a good agreement with the measurements. The detailed calculation of the projectile population kinetics gives the quantitative analysis of the spectral line intensity.

$I(\text{He}_{\alpha 1})/I(\text{Ly}_{\alpha})$	Experiment	Calculation	$Z_{av}(\text{calcul.})$
9 MeV/u			
gas	2.2	2.47	17.99
aerogel	1.4	1.2	18.43
4 MeV/u			
gas	-	14.6	17.14
aerogel	4.87	4.98	17.54

Table 5.1: *Relative intensities of resonance lines of Ca^{19+} and Ca^{18+} ions (Ly_{α} and $\text{He}_{\alpha 1}$) compared at high and low ion energy in gaseous and aerogel media. The average charge of Ca ions is calculated for these conditions.*

A good accuracy of the theoretical predictions was obtained for the measurement of the charge state distribution of the projectile ions having left the target by a magnetic spectrometer (see subsection 4.1.5). In the experiment on the interaction of 11.4 MeV/u calcium ions with a 8.39-mm-thick piece of 0.023 g/cm³ silica aerogel the spectroscopic analysis of the K-shell projectile radiation was complemented by measurements of the charge state distribution after the target by a magnetic spectrometer. The ion beam energy measured by the time-of-flight method was 6.54 MeV/u. The fractions of Ca charge states observed by means of the magnet spectroscopy correspond to the calculated population kinetics of excited ion states at the same energy (figure 5.3).

Certainly, the spectra observed inside the target (excited states of projectile ions)(figure 4.10a) and after the target (ions in the ground state)(figure 4.10b) can not be compared directly. However, it is possible to reconstruct the dynamics of the projectile ions for the measurement after the target: to simulate the line intensities of projectiles before a complete relaxation takes place. In this case one can simulate what would be the population of excited levels of the ions measured after the magnet without having undergone the full relaxation process. Using population mechanisms of the excited states $2p$ of Ca^{19+} , $1s2p$ (1P_1) of Ca^{18+} and $1s2l2l'$ of Ca^{17+} detailed described in the previous chapter, the relative line intensities were calculated. The results are in close agreement with measured K-shell spectrum of the experiment (table 5.2).

In conclusion of this chapter, it should be noted that the quantitative analysis of the ion charge along the stopping process in matter needs a detailed calculation of the population kinetics of the ion energy levels. Using measured dependence of the projectile velocity on the ion penetration depth for the calculation of rate coefficients of collisional processes it is possible to analyze the behaviour of the projectile bound structure along the stopping process.

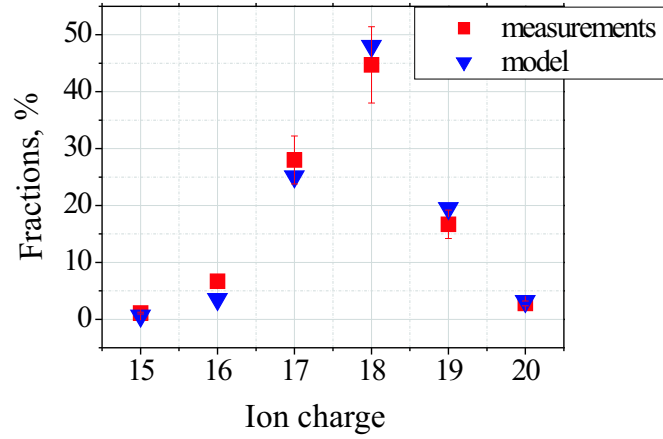


Figure 5.3: The ion charge state distribution measured by a magnet spectrometer and calculated population kinetics of the ground and excited states of projectile ions at energy of 6.54 MeV/u.

	Measurement	Calculation
$I(\text{Ly}_\alpha)/I(\text{He}_\alpha)$	0.59	0.57
$I(\text{He}_\alpha)/I(\text{Li-like})$	2.67	2.2

Table 5.2: Measured and simulated data of relative line intensities for the experiment on the interaction of 11.4 MeV/u Ca ions with a 8.39-mm-thick piece of 0.023 g/cm³ SiO₂ aerogel.

Chapter 6

Conclusions and outlook

The study of the slowing down process of fast heavy ions inside matter is presented in this thesis. The main results of the work are following:

- A novel diagnostic method, X-ray spectroscopy of K-shell projectile radiation, to measure the stopping process inside the target material has been introduced.
- For the first time, a spatially resolved analysis of the stopping process inside solids has been performed. Silica aerogels with the mean densities of 0.15 - 0.023 g/cm³ were used as a stopping medium that provided a stretching of the ion stopping length up to 2 - 11 mm. It has been shown that a porous aerogel structure has no significant influence on the ion stopping process.
- The spatially resolved K-shell projectile and target radiation has been investigated. A strong dependence of the spectra on the ion charge state and velocity has been shown. The ion charge evolution along the ion stopping path in the target material has been explained with the influence of capture and loss processes.
- The Doppler Effect was observed on the projectile K-shell spectra of magnesium and calcium ions with initial energy of 11.4 MeV/u. The line Doppler shift was used to calculate the ion velocity in relation to the penetration depth in the target material. In the case of calcium ions the velocity analysis showed a good agreement with the time-of-flight measurements.
- In order to interpret the experimental results a numerical model of the ion population kinetics has been developed. Detailed calculations provide a quantitative analysis of the ion charge evolution during the stopping process. The theoretical predictions are in good agreement with the measurements of the ion charge state distribution recorded after the target by a magnetic spectrometer.
- In the framework of this thesis, the influence of the target density on the stopping process has been studied. A quantitative analysis of the K_α spectra of fast heavy ions has been performed in solid and gaseous targets. The higher population of Ca¹⁹⁺ and Ca¹⁸⁺ excited states in solid in comparison with a gaseous medium

at the same ion energy has been shown. The experimental results are in close agreement with the numerical model.

The influence of the target density on the stopping process inside cold matter has been investigated in this thesis. However, there are still many open questions to answer whether the gas-solid effect has an influence on the ion charge state distribution and energy loss in plasma experiments. The main motivation for future plasma investigations is to minimize the gas-solid effect.

In experiments on Xe ions the energy loss and charge state distribution while passing through a solid carbon target and a laser produced plasma with a carbon foil were compared [Süss, 1999]. One has expected an increase of the ion energy loss and the ion mean charge in plasma (plasma effect) [Hoffmann et al., 1990]. However, the charge state analysis of the Xe ion beam has shown an opposite result: the Xe ion mean charge state decreased from 42 in solid down to 35 in plasma. This can be explained by the change of the target density, which can be decreased by more than three orders of magnitude. Therefore, the reduction of the ion charge in the expanded plasma in comparison to the solid foil can be observed.

The density effect can also be important for experiments with a cold gas and plasmas produced by explosive driven shock waves or in Z-pinch. An increase of the projectile ion mean charge due to the increase of the target density by 100-1000 times can be wrongly attributed to the plasma effect.

Recently, a big progress has been achieved in the field of heavy-ion interaction with matter due to new powerful experimental methods and facilities. The key instrument of the modern investigations and applications is the detailed knowledge about atomic collisions during the ion slowing down in cold matter. This study has a promising future due to challenging theoretical problems and the growing field of applications.

Bibliography

- [Ahiezer and Berestetski, 1981] A. I. Ahiezer and V. B. Berestetski (1981). *Quantum electrodynamics*. Nauka. Moscow.
- [Ahlen, 1980] S. P. Ahlen (1980). *Rev. of Mod. Phys.* **52**, 121.
- [Anthony and Lanford, 1982] J. M. Anthony and W. A. Lanford (1982). *Phys. Rev. A* **25**, 1868.
- [Baragiola et al., 1976] R. A. Baragiola, P. Ziem, and N. Stolterfoht (1976). *J. Phys. B: Atom. Molec. Phys.* **9**, L447.
- [Barkas et al., 1963] W. Barkas, J. N. Dyer, and H. H. Heckman (1963). *Phys. Rev. Lett.* **11**, 26.
- [Barkas et al., 1956] W. H. Barkas, W. Birnbaum, and F. M. Smith (1956). *Phys. Rev.* **101**, 778.
- [Bethe, 1930] H. Bethe (1930). *Ann. Physik* **5**, 325.
- [Bethe, 1932] H. Bethe (1932). *Z. Phys.* **76**, 293.
- [Betz, 1972] H. D. Betz (1972). *Rev. of Mod. Phys.* **44**, 465.
- [Betz and Grodzins, 1970] H. D. Betz and L. Grodzins (1970). *Phys. Rev. Letters* **25**, 211.
- [Betz et al., 1966] H. D. Betz, G. Hortig, E. Leischner, C. Schmelzer, B. Stadler, and J. Weihrauch (1966). *Phys. Letters* **22**, 643.
- [Bimbot et al., 1989] R. Bimbot, C. Cabot, D. Gardes, H. Gauvin, I. Orliange, L. DeReilhac, K. Subotic, and F. Hubert (1989). *Nucl. Instr. and Meth. B* **44**, 19.
- [Bloch, 1933] F. Bloch (1933). *Ann. Physik* **16**, 285.
- [Bohr, 1913] N. Bohr (1913). *Philos. Mag.* **25**, 10.

- [Bohr, 1941] N. Bohr (1941). *Phys. Rev.* **59**, 270.
- [Bohr, 1948] N. Bohr (1948). *K. Danske Vidensk. Selskab. Mat.-Fys. Medd.* **18**, 1.
- [Bohr et al., 1940] N. Bohr, J. K. Boggild, K. J. Brostrom, and T. Lauritsen (1940). *Phys. Rev.* **58**, 839.
- [Bohr and Lindhard, 1954] N. Bohr and J. Lindhard (1954). *K. Danske Vidensk. Selskab. Mat.-Fys. Medd.* **28**, 1.
- [Boiko et al., 1985] V. A. Boiko, A. V. Vinogradov, S. A. Pikuz, I. Y. Skobelev, and A. Y. Faenov (1985). **6**, 82.
- [Borisenko and Merkuliev, 1996] N. G. Borisenko and Y. A. Merkuliev (1996). Targets having microheterogeneous structure for the spherical laser compression. In: N. S. Publishers (Ed.), *Proc. of P. N. Lebedev Institute* Vol. 221. New York.
- [Brinkman and Kramers, 1930] D. R. Brinkman and H. A. Kramers (1930). *Proc. Acad. Sci. Amst.* **33**, 973.
- [Dmitriev and Nikolaev, 1964] I. S. Dmitriev and V. S. Nikolaev (1964). *Zh. Eksperim. i Teor. Fiz.* **47**, 615. [Sov. Phys. JETP, 20, 409, (1965)].
- [Eichter and Chan, 1979] J. Eichter and F. T. Chan (1979). *Phys. Rev. A* **20**, 104.
- [Eichter et al., 1981] J. Eichter, A. Tsuji, and T. Ishihara (1981). *Phys. Rev. A* **23**, 2833.
- [Faenov et al., 1994] A. Y. Faenov, S. A. Pikuz, A. I. Erko, B. A. Bryunetkin, V. M. Dyakin, G. V. Ivanenko, A. R. Mingaleev, T. A. Pikuz, V. M. Romanova, and T. A. Shelkovenko (1994). *Phys. Scr.* **50**, 333.
- [Fermi, 1939] E. Fermi (1939). *Phys. Rev.* **56**, 1242.
- [Franzke et al., 1967] B. Franzke, N. Angert, A. Möller, and C. Schmelzer (1967). *Phys. Letters* **25 A**, 769.
- [Geissel et al., 1982] H. Geissel, Y. Laichter, W. F. W. Schneider, and P. Armbruster (1982). *Nucl. Instr. and Meth.* **194**, 21.
- [Geissel et al., 2002] H. Geissel, H. Weick, C. Scheidenberger, R. Bimbot, and D. Gardes (2002). Experimental studies of heavy-ion slowing down in matter. Preprint 24 GSI Darmstadt.

- [Gryzinski, 1965a] M. Gryzinski (1965a). *Phys. Rev.* **138**, 305.
- [Gryzinski, 1965b] M. Gryzinski (1965b). *Phys. Rev.* **138**, 322.
- [Gryzinski, 1965c] M. Gryzinski (1965c). *Phys. Rev.* **138**, 336.
- [Henke et al., 1984] B. L. Henke, F. G. Fujiwara, M. A. Tester, C. H. Dittmore, and M. A. Palmer (1984). *J. Opt. Soc. Am. B* **1**, 828.
- [Henke et al., 1986] B. L. Henke, J. Y. Uejio, G. F. Stone, C. H. Dittmore, and F. G. Fujiwara (1986). *J. Opt. Soc. Am. B* **3**, 1540.
- [Hoffmann et al., 2005] D. H. H. Hoffmann, A. Blazevic, P. Ni, O. Rosmej, M. Roth, N. A. Tahir, A. Tauschwitz, S. Udrea, D. Varentsov, K. Weyrich, and Y. Maron (2005). *Laser Part. Beams* **23**, 47.
- [Hoffmann et al., 2002] D. H. H. Hoffmann, V. E. Fortov, I. V. Lomonosov, V. Mintsev, N. A. Tahir, D. Varentsov, and J. Wieser (2002). *Phys. of Plasmas* **9**, 3651.
- [Hoffmann et al., 1990] D. H. H. Hoffmann, K. Weyrich, H. Wahl, D. Gardes, R. Bimbot, and C. Fleurier (1990). *Phys. Rev. A* **42**, 2313.
- [Kaneko, 1994] T. Kaneko (1994). *Phys. Rev. A* **49**, 2681.
- [Kraft, 2000] G. Kraft (2000). *Progr. Part. Nucl. Phys.* **45**, 473. Supplement 2.
- [Labaune et al., 2000] C. Labaune, W. J. Hogan, and K. A. Tanaka (2000). Inertial Fusion Science and Applications IFSA 99. In: E. Science (Ed.), *Proc. of the Conference*. Paris.
- [Lamb, 1940] W. E. Lamb (1940). *Phys. Rev.* **58**, 696.
- [Lassen, 1951a] N. O. Lassen (1951a). *K. Danske Vidensk. Selskab. Mat.-Fys. Medd.* **26** (5).
- [Lassen, 1951b] N. O. Lassen (1951b). *K. Danske Vidensk. Selskab. Mat.-Fys. Medd.* **26** (12).
- [Lebedev and Beigman, 1998] V. S. Lebedev and I. L. Beigman (1998). *Physics of highly excited atoms*. Springer. Berlin.
- [Lindhard and Sørensen, 1996] J. Lindhard and A. H. Sørensen (1996). *Phys. Rev. A* **53**, 2443.

- [Martin and Northcliffe, 1962] F. W. Martin and L. C. Northcliffe (1962). *Phys. Rev.* **128**, 1166.
- [May, 1964] R. M. May (1964). *Phys. Rev. A* **136**, 669.
- [Maynard et al., 2001] G. Maynard, G. Zwicknagel, C. Deutsch, and K. Katsonis (2001). *Phys. Rev. A* **63**, 052903.
- [McGuire and Richard, 1973] J. H. McGuire and P. Richard (1973). *Phys. Rev. A* **8**, 1374.
- [Melchert, 1999] F. Melchert (1999). *Atomic physics with heavy ions*. Springer-Verlag Berlin.
- [Nikolaev and Dmitriev, 1968] V. S. Nikolaev and I. S. Dmitriev (1968). *Phys. Letters* **28A**, 277.
- [Nikolaev et al., 1963] V. S. Nikolaev, I. S. Dmitriev, Y. A. Teplova, and N. L. Fateeva (1963). *Izv. Acad. Nauk SSSR, Ser. Fiz.* **27**, 1078. [Bull. Acad. Sci. USSR, Phys. Ser. 27, 1049].
- [Northcliffe, 1963] L. C. Northcliffe (1963). *Ann. Rev. Nucl. Sci.* **13**, 67.
- [Northcliffe and Schilling, 1970] L. C. Northcliffe and R. F. Schilling (1970). *Nucl. Data Tabl.* **A7**, 233.
- [Oppenheimer, 1928] J. R. Oppenheimer (1928). *Phys. Rev.* **31**, 349.
- [Pierce and Blann, 1968] T. E. Pierce and M. Blann (1968). *Phys. Rev.* **173**, 390.
- [Pikuz et al., 1995] T. A. Pikuz, A. Y. Faenov, S. A. Pikuz, V. M. Romanova, and T. A. Shelkovenko (1995). *J. X-ray Sci. Technol.* **5**, 323.
- [Rosmej et al., 2003] O. N. Rosmej, S. Pikuz, J. Wieser, A. Blazevic, E. Brambrink, M. Roth, V. P. Efremov, A. Y. Faenov, T. A. Pikuz, I. Y. Skobelev, and D.H.H.Hoffmann (2003). *Rev. of Sci. Instr.* **74**, 5039.
- [Rosmej et al., 2002] O. N. Rosmej, J. Wieser, M. Geissel, F. Rosmej, A. Blazevic, J. Jacoby, E. Dewald, M. Roth, E. Brambrink, K. Weyrich, D. H. H. Hoffmann, T. A. Pikuz, A. Y. Faenov, A. I. Magunov, I. Y. Skobelev, N. G. Borisenko, V. P. Shevelko, A. A. Golubev, A. Fertman, V. Turtikov, and B. Y. Sharkov (2002). *Nucl. Instr. and Meth. in Phys. Res. A* **495**, 29.
- [Rutherford, 1911] E. Rutherford (1911). *Philos. Mag.* **21**, 669.

- [Ryding et al., 1969] G. Ryding, A. Wittkower, and P. H. Rose (1969). *Phys. Rev.* **184** (1), 93.
- [Safronova and Lisina, 1979] U. I. Safronova and T. G. Lisina (1979). *Atom. Data and Nucl. Data Tabl.* **24**, 49.
- [Sanchez del Rio et al., 2004] M. Sanchez del Rio, L. Alianeli, A. Y. Faenov, and T. Pikuz (2004). *Phys. Scr.* **69**, 297.
- [Schiwietz and Grande, 1999] G. Schiwietz and P. L. Grande (1999). *Nucl. Instr. and Meth. in Phys. Res. B* **153**, 1.
- [Schiwietz and Grande, 2001] G. Schiwietz and P. L. Grande (2001). *Nucl. Instr. and Meth. in Phys. Res. B* **175 - 177**, 125.
- [Schlachter et al., 1983] A. S. Schlachter, J. W. Stearns, W. G. Graham, K. H. Berkner, R. V. Pyle, and J. A. Tanis (1983). *Phys. Rev. A* **27**, 3372.
- [Shevelko, 1978] V. P. Shevelko (1978). *Z. Phys. A* **287**, 19.
- [Shevelko, 1980] V. P. Shevelko (1980). *J. Phys. B* **13**, L319.
- [Shevelko, 1999] V. P. Shevelko (1999). *Collisional processes with charge exchange of multielectron atoms and ions*. Habilitation P. N. Lebedev Physical Institute Moscow.
- [Shevelko, 2001] V. P. Shevelko (2001). *Tech. Phys.* **46**, 1225.
- [Shevelko et al., 2005] V. P. Shevelko, H. Tawara, O. V. Ivanov, T. Miyoshi, K. Noda, Y. Sato, A. V. Subbotin, and I. Y. Tolstikhina (2005). *J. Phys. B: At. Mol. Opt. Phys.* **38**, 2675.
- [Shevelko et al., 2001] V. P. Shevelko, I. Y. Tolstikhina, and T. Stöhlker (2001). *Nucl. Instr. and Meth. in Phys. Res. B* **184**, 295.
- [Shevelko and Vainshtein, 1993] V. P. Shevelko and L. A. Vainshtein (1993). *Atomic physics for hot plasmas*. Institute of Physics Publishing. Bristol and Philadelphia.
- [Shima et al., 1982] K. Shima, T. Ishihara, and T. Mikumo (1982). *Nucl. Instr. and Meth.* **200**, 605.
- [Sigmund, 1997] P. Sigmund (1997). *Phys. Rev. A* **56**, 3781.
- [Sigmund and Schinner, 2001] P. Sigmund and A. Schinner (2001). *Nucl. Instr. and Meth. in Phys. Res. B* **1742**, 535.

- [Skobelev et al., 1995] I. Y. Skobelev, A. Y. Faenov, B. A. Bryunetkin, V. M. Dyakin, T. A. Pikuz, S. A. Pikuz, T. A. Shelkovenko, and V. M. Romanova (1995). *JETP* **81**, 692.
- [Slater, 1960] J. C. Slater (1960). *Quantum Theory of Atomic Structure*. McGraw Hill. New York.
- [Sobelman et al., 1980] I. I. Sobelman, L. A. Vainshtein, and E. A. Yukov (1980). *Excitation of atoms and broadening of spectral lines*. Series in chemical physics. Springer. Berlin.
- [Sobelman et al., 1995] I. I. Sobelman, L. A. Vainshtein, and E. A. Yukov (1995). *Excitation of Atoms and Broadening of Spectral Lines*. Springer. Berlin. 2nd edition.
- [Spädtkke, 2003] P. Spädtkke (2003). Ion source development and operation. Scientific report GSI.
- [Süss, 1999] W. Süss (1999). *Experimentelle Bestimmung der Ladungsverteilung schwerer Ionen nach Wechselwirkung mit dichten, lasererzeugten Plasmen*. Dissertation Technischen Universität Darmstadt.
- [Tahir et al., 2003] N. A. Tahir et al. (2003). *Contributions to Plasma Physics* **43**, 373.
- [Tahir et al., 2006] N. A. Tahir, P. Spiller, S. Udrea, O. D. Cortazar, C. Deutsch, V. E. Fortov, V. Gryaznov, D. H. H. Hoffmann, I. V. Lomonosov, P. Ni, A. R. Piriz, A. Shutov, M. Temporal, and D. Varentsov (2006). *Nucl. Instr. and Meth. in Phys. Res. B* **245**, 85.
- [Thoe, 1986] R. Thoe (1986). *J. Opt. Soc. Am. A* **3**, 1407.
- [Thomson, 1906] J. Thomson (1906). *Conduction of electricity through gases*, pp. 370–382. Cambridge University Press 2nd rev. edition.
- [Vainshtein et al., 1973] L. A. Vainshtein, I. I. Sobelman, and E. A. Yukov (1973). *Excitation cross sections of atoms and ions by electrons*. Nauka. Moscow.
- [Varentsov, 2006] D. Varentsov (2006). (unpublished).
- [Young et al., 1998] B. K. Young, A. L. Osterheld, D. F. Price, R. Shepherd, R. E. Stewart, A. Y. Faenov, A. I. Magunov, T. A. Pikuz, I. Y. Skobelev, F. Flora, S. Bollanti, P. D. Lazzaro, D. Letardi, A. Grilli, L. Palladino, A. Reale, A. Scafati, and L. Reale (1998). *Rev. Sci. Instr.* **69**, 4049.

- [Ziegler et al., 1985] J. F. Ziegler, J. P. Biersack, and U. Littmark (1985). *The stopping and range of ions in solids*. Pergamon Press. New York.

Acknowledgments

I am glad to have the opportunity to express my gratitude to the people who helped and supported me during my work.

At first I would like to thank to Prof. Dr. Dr. h.c./RUS Dieter H.H. Hoffmann, who gave me the unique opportunity to make this thesis possible at GSI. I am very thankful to him for the interesting topic and his continued help during the work.

My deep gratitude I want to express to my supervisor Dr. Olga Rosmej for our fruitful work together in experiments, analysis and discussions. She guided my steps into X-ray spectroscopy and atomic physics. Without her help and advices this work could not have been done.

I am thankful to Prof. Dr. Markus Roth, who gives consent to be the co-adviser of my work. I deeply appreciate the strong support in experiments and generous discussions about my thesis Dr. Sergey Pikuz, Jr., Dr. Alexander Fertman, Dr. Vladimir Turtikov, Dr. Abel Blazevic and Dipl.-Phys. Timofey Mutin. My gratitude goes as well to Prof. Viatcheslav Shevelko for simulations, which are the significant part of my theoretical calculations, and wise advices. Also, I thank to Dr. Dmitry Varentsov for performed hydrodynamic simulations.

I address my thanks to Dipl.-Phys. Gabriel Schaumann for the great help in preparation of the experiments and my first steps in AutoCAD. I would like to express my sincere gratitude to MSc. Gonzalo Rodriguez Prieto for helpful suggestions, Heinrich Wahl for technical support and Malte Hagemann for help in Mathematica.

I wish to thank all colleagues from GSI Plasma Physics Group for the warm environment, support and friendly time together.

For corrections of this thesis I would like to acknowledge Prof. R. Bock, Prof. Th. Kuehl, Dr. O. Rosmej and Dr. A. Blazevic.

For love and understanding I thank to my best friends Oksana, Larysa, Wolfgang, Holger, Nadezda. A new definition of friendship I discovered with Gergana, Beyza, Seimon, Jonas, Ireri, Manisch, Reza, Tanja. I thank them also for the strong support in German language.

My special thanks go to my friend Udo. I am very grateful to him for his help, advices, discussions, patience and just the time together. He gave me more than a

large support in a foreign country.

Finally, I express my absolute thankfulness to my family for love and psychological support during the work as well as my whole life.

Curriculum Vitae

Name: Svitlana I. Korostiy

Birth date/place: 01.08.1980 / Gadyach (Ukraine)

Citizenship: ukrainian

Education profile:

1986-1997: Primary and secondary school in Gadyach, Ukraine.

1997-2003: Student at the Kharkiv National University, Ukraine. Specialization: Experimental nuclear physics and plasma physics.

2003: Engineer-Physicist at the Kharkiv National University. Thesis: "The study of secondary emission properties of materials for design of the secondary emission radioisotope current source".

since Apr. 2003: Ph.D. student at the Technical University, Darmstadt and Gesellschaft für Schwerionenforschung, Darmstadt, Germany.

Erklärung

Hiermit erkläre ich, dass die vorliegende Arbeit von mir selbständig und nur mit den angegebenen Hilfsmitteln angefertigt wurde, und dass bisher noch kein Promotionsversuch unternommen wurde.

Darmstadt, den 17.07.06